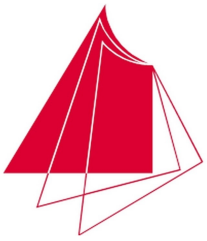

Hochschule Karlsruhe
Technik und Wirtschaft
UNIVERSITY OF APPLIED SCIENCES

Air-suspended single-mode polymer waveguides towards highly sensitive optofluidic sensors

A thesis submitted in fulfilment of the requirements for the degree of Doctor of Philosophy

Christoph Prokop
M. Eng.

College of Science, Engineering and Health
School of Engineering
RMIT University
Melbourne, Australia

Faculty of Electrical Engineering and Information Technology
Institute for Optofluidics and Nanophotonics
Karlsruhe University of Applied Sciences
Karlsruhe, Germany

November 2016

Statutory Declaration

I certify that except where due acknowledgement has been made, the work is that of the author alone; the work has not been submitted previously, in whole or in part, to qualify for any other academic award; the content of this thesis is the result of work which has been carried out since the official commencement date of the approved research program; any editorial work, paid or unpaid, carried out by a third party is acknowledged; and, ethics procedures and guidelines have been followed.

Christoph Prokop

November 2016

Acknowledgements

First and foremost, I want to thank my supervisor Christian Karnutsch for providing me the opportunity to perform this Ph.D. work at the Institute for Optofluidics and Nanophotonics (IONAS) at the Karlsruhe University of Applied Sciences. It has been an honour to be your first Ph.D. student. Getting appointed as professor and setting up an institute and perform recognized research with limited budget and only one Ph.D student has never been easy, especially with the huge amount of teaching required at a University of Applied Sciences. Your selfless and hard work enabled a lot of this at IONAS, including the acquisition of the equipment of our three labs, the numerous student projects from which I also benefited and last but not least the Ph.D. Studies Agreement between the University of Applied Sciences Karlsruhe and the RMIT University Melbourne. Thank you for all your support and guidance throughout my work at IONAS.

I also would like to express my deepest gratitude to my supervisor Arnan Mitchell from RMIT University Melbourne for providing me the opportunity to complete my thesis as an international Ph.D. student at RMIT. Thank you for your support during my Ph.D work and the enthusiasm to shape my scientific research skills not only during my stay in your group.

Among many other members of my faculty, I would like to thank Margarita Aleksandrova, Jan Wernthal, Gerd Westermann and Wolfgang Loés from the Faculty of Electrical Engineering and Information Technology for their helpful advice and support during my Ph.D. work, fabrication of mechanical parts or acquisition of equipment. Furthermore, I would like to thank Angela Brauch and Bernhard Beck from the Faculty of Mechanical Engineering and Mechatronics for the help with SEM images and the support with the clean room facility.

I also would like to thank Sandra Wolff and Bert Laegel from the Nano Structuring Center of the University in Kaiserslautern for the fabrication of E-Beam written structures and their support during the preparation of several manuscript drafts.

Many thanks go to all of the students who supported my research during my time at IONAS. I really enjoyed the companionship and solidarity we had at IONAS and especially the group activities and the after work beers.

Lastly, I would like to thank my friends outside the University and my family for supporting and encouraging me throughout my personal and professional life.

Abstract

In this thesis, a polymer lamination method is presented that enables efficient light coupling into air-suspended polymer waveguides by grating couplers which can then be exploited for research towards a large range of applications in the field of microfluidics, optics and optofluidics. This approach is especially useful for highly sensitive integrated optofluidic sensors as has been demonstrated in this work.

Due to the low refractive index contrast available between various polymer materials, the efficiency of miniaturized polymer photonic and optofluidic devices is often limited. In this work, a new lamination technique is presented that allows the bonding of unstructured and structured layers of SU-8 photoresist down to submicron thicknesses onto microchannels fabricated in KMPR photoresist using a flexible PDMS carrier stamp. This approach enables the creation of air-suspended SU-8 structures with the highest possible refractive index contrast. Such layers can be bonded down to a thickness of 0.5 μm which in principal allows guidance of light of infrared wavelengths within the single-mode regime.

In order to exploit this approach for highly sensitive optofluidic sensing applications, light needs to be coupled into such layers. In this work light coupling is achieved using air-suspended SU-8 rib waveguides and butt coupling, as well as using air-suspended SU-8 surface grating couplers. Particularly, air-suspended SU-8 grating couplers are very interesting. After numerical simulations, air-suspended SU-8 grating couplers have been fabricated based on the developed lamination method. Transmission measurements have shown that a single grating coupler exhibits approximately 8 dB coupling loss at a centre wavelength of 1557 nm indicating a coupling efficiency of about 16 %. In addition, the thermal sensitivity of the air-suspended SU-8 grating couplers has been studied by numerical simulations followed by experimental evaluation.

Even though the achieved coupling efficiencies are lower than for SOI couplers, mainly due to current fabrication limits of the master structures, the fabrication method employing widely used polymer materials has the advantage that multiple air-suspended structures can directly be created in only one simple lamination process without the need of additional etching steps.

Finally, different optofluidic sensor concepts are proposed based on the demonstrated SU-8 bonding method and the air-suspended SU-8 waveguide grating couplers. Experimental transmission measurements have shown that a first sensor concept exhibits a refractive index sensitivity of approximately 400 nm RIU^{-1} according to the wavelength shift and 17 dB RIU^{-1} due to the intensity loss which is similar to the results of the numerical simulations. In comparison to previously shown sensing applications using grating coupler structures, the analytes can directly be probed in-line due to the combination of a microfluidic channel and air-suspended grating couplers making the proposed sensor concept highly applicable for in-line polymer optofluidics and suitable for low-cost optofluidics and photonics sensor concepts.

However, in order to detect even the smallest differences in analytes, higher sensitivities would be required. Therefore, a second sensor concept aims to increase the sensitivity by introducing a long-period grating into an air-suspended SU-8 waveguide in order to enhance the light-matter interaction strength. Numerical simulations have been carried out to obtain a set of parameters for a multi-mode long-period grating sensor for TE polarized light at a resonance wavelength of 1550 nm. Transmission calculations as a function of wavelength have shown that such sensor can exhibit a very high refractive index sensitivity of about 6000 nm RIU^{-1}.

In summary, this thesis introduces a new polymer lamination method for thin, structured air-suspended SU-8 films down to sub-micron thicknesses. In fact, such films are thin enough to provide single-mode guidance of light in planar waveguides in the infrared wavelength regime. By exploiting air-suspended SU-8 grating couplers, light can be efficiently coupled into such waveguides. Different applications in the fields of microfluidics, optics and optofluidics are introduced in this thesis and it appears that the thin air-suspended SU-8 films can be robust enough even for the realisation of real world applications.

Publications

Journal publications

1. Markus Knoerzer, Christoph Prokop, Graciete M. Rodrigues Ribeiro, Horst Mayer, Jens Bruemmer, Arnan Mitchell, Dominik G. Rabus, and Christian Karnutsch. BANSAI - An optofluidic approach for biomedical analysis. *Optofluidics, Microfluidics and Nanofluidics*, 2(1):22-30, 2015. doi:10.1515/optof-2015-0003.
2. Christoph Prokop, Steffen Schoenhardt, Tanveer Mahmud, Arnan Mitchell, and Christian Karnutsch. Bonding of SU-8 films onto KMPR structures for microfluidic, air-suspended photonic and optofluidic applications. *Journal of Micromechanics and Microengineering*, 26(5):055001, 2016. doi:10.1088/0960-1317/26/5/055001.
3. Christoph Prokop, Steffen Schoenhardt, Bert Laegel, Sandra Wolff, Arnan Mitchell, and Christian Karnutsch. Air-suspended SU-8 polymer waveguide grating couplers. *IEEE Journal of Lightwave Technology*, 34(17):3966-3971, 2016. doi:10.1109/JLT.2016.2593025.
4. Christoph Prokop, Tobias Schmalz, Philipp Kleessen, Bert Laegel, Sandra Wolff, Arnan Mitchell, and Christian Karnutsch. Tunable air-suspended polymer grating couplers. *Optical Engineering*, 56(6):067112-4, 2017. doi:10.1117/1.OE.56.6.067112.
5. Christoph Prokop, Nico Irmler, Bert Laegel, Sandra Wolff, Arnan Mitchell, and Christian Karnutsch. Optofluidic refractive index sensor based on air-suspended SU-8 grating couplers. *Sensors and Actuators A: Physical*, 263:439-444, 2017. doi:10.1016/j.sna.2017.07.014.

Conference contributions

1. Christoph Prokop, Philipp Gutruf, Eike Zeller, Christian Karnutsch and Arnan Mitchell. UV-Nanoimprint Lithography in KMPR with high dimensional accuracy for optofluidic devices. Oral presentation at 2nd Conference on Optofluidics (EOSOF 2013), Munich, Germany, April 2013.
2. Christoph Prokop, Steffen Schoenhardt, Christian Karnutsch and Arnan Mitchell. Microfluidic refractive index sensor based on polymer grating couplers. Oral presentation at Laser Optics Congress for Optical Sensors and Cyber-Physical Systems 2014, Berlin, Germany, March 2014.

3. Christoph Prokop, Philipp Kleessen, Nico Irmler, Arnan Mitchell and Christian Karnutsch. Air-suspended polymer rib waveguides. Oral presentation and conference proceedings in SPIE OPTO. International Society for Optics and Photonics, San Francisco, United States of America, Proc. SPIE 9365, Integrated Optics: Devices, Materials, and Technologies XIX, February 2015. doi:10.1117/12.2079207.
4. Christian Karnutsch and Christoph Prokop. Optofluidics and Nanophotonics at IONAS - Enabling technologies for micro- and nanoplatforms for biosensors and biomedical analysis systems. Poster presentation at 16$^{\text{th}}$ German-American Frontiers of Engineering Symposium (GAFOE 2015), Potsdam, Germany, April 2015.
5. Christoph Prokop, Arnan Mitchell and Christian Karnutsch. Air-suspended polymer structures for optofluidic sensors. Poster presentation at COST MP1205 General Meeting and Conference - Integration of Optical Control and Photonics with Microfluidics, Porto, Portugal, May 2015.
6. Christoph Prokop, Nico Irmler, Bert Laegel, Sandra Wolf, Arnan Mitchell and Christian Karnutsch. Air-suspended polymer grating coupler applied as optofluidic refractive index sensor. Oral presentation at 3$^{\text{rd}}$ Conference on Optofluidics (EOSOF 2015), Munich, Germany, June 2015.
7. Christian Karnutsch, Christoph Prokop, Crispin Szydzik, Khashayar Khoshmanesh and Arnan Mitchell. Optofluidic Platforms for Miniaturized Biomedical Analysis Systems. Invited talk at Progress In Electromagnetics Research Symposium (PIERS 2015), Prague, Czech Republic, July 2015.

Scientific contributions not referred in this thesis

1. Christoph Prokop, Aliakbar Ebnali-Heidari, Majid Ebnali-Heidari and Christian Karnutsch. Label-free biosensors based on nanoinfiltrated photonic crystal slow light structures. Poster presentation at BioNanoMed 2013, Krems, Austria, March 2013.
2. Christoph Prokop, Aliakbar Ebnali-Heidari, Majid Ebnali-Heidari and Christian Karnutsch. Loss Engineering in Slow-Light Photonic Crystal Waveguides. Poster presentation at 2$^{\text{nd}}$ Conference on Optofluidics (EOSOF 2013), Munich, Germany, April 2013.

3. A. Ebnali-Heidari, C. Prokop, M. Ebnali-Heidari, and C. Karnutsch. A Proposal for Loss Engineering in Slow-Light Photonic Crystal Waveguides. *IEEE Journal of Lightwave Technology*, 33(9):1905-1912, 2015. doi:10.1109/JLT.2015.2391196.
4. Christoph Prokop, Tobias Schmalz and Christian Karnutsch. Selective infiltration and storage of picoliter volumes of liquids into sealed SU-8 microwells. *Optofluidics, Microfluidics and Nanofluidics*, 3(1):35-43, 2016. doi:10.1515/optof-2016-0005.

Other publications

1. Christoph Prokop and Christian Karnutsch. Projekt MikroBANSAI - Biomedizinisches Analysesystem mit Laserlicht. horizonte 43, ISSN: 1432-9174, p. 22-24, March 2014.
2. Christoph Prokop and Christian Karnutsch. μBANSAI: Biomedizinisches Analysesystem mit Laserlicht. Forschungsreport Elektrotechnik in Baden-Wuerttemberg (ISSN: 2199-4889), p. 55-56, November 2015.

Awards and scholarships

1. Best student poster presentation, 2$^{\text{nd}}$ Conference on Optofluidics (EOSOF 2013), Munich, Germany, April 2013
2. Doctoral Scholarship of the Heinrich-Hertz Society, Gesellschaft zur Pflege wissenschaftlicher Kontakte im Hause Heinrich Hertz e.V., Karlsruhe, Germany, October 2014
3. DAAD RISE Scholarship, February 2015
4. SPIE Optics and Photonics Education Scholarship, May 2015

Contents

List of Figures

List of Tables

1 Introduction

This Chapter introduces the broader research context and motivates the work carried out in this thesis. The key problems are identified and a thesis outline is given.

1.1 Motivation

Medical diagnostic systems are important tools in today's medicine allowing the correct diagnosis of numerous disease symptoms and hence increase the potential for a successful therapy of a patient. To increase our well-being and life span, our society has always striven to improve human health, which generates a continuous demand on improving existing sensing devices and developing new tests and diagnostic principles. Currently, most medical diagnostic tests are carried out in specialized clinical laboratories requiring bulky, sophisticated equipment and trained staff making such tests immobile, time consuming and thus expensive. In order to diagnose symptoms of a patient earlier and hence increase the potential of a successful therapy, local point-of-care measurements, for example in medical offices or ambulances, would significantly enhance the accessibility of medical diagnostic tests. However, this vision requires new sensing and detection principles to overcome the disadvantages of current diagnostic systems.

A new field of research that has attracted much interest in the last ten years is optofluidics, which integrates microfluidic and optical elements on the micrometre scale for widespread applications in fundamental sciences and engineering [1–3]. Combining microfluidics and integrated photonic circuits enables devices that can carry analytes in microchannels to be probed by the light or conversely, a photonic device can be modulated by a fluid. Since optical phenomena are often exploited for medical diagnosis, optofluidic sensor principles are very attractive as light is harmless to the analyte and does not significantly interfere with the electric and magnetic circuits of the surrounding peripheral equipment. Furthermore, optofluidic sensors offer attractive advantages such as low reagent and sample consumption, relatively easy detection of molecular interactions as well as high processing speeds and precision. With the growing trend towards mass-producible and disposable sensing devices, polymer materials have gained great interest in the last decade due to low-cost, rapid and flexible processing which basically allows single-use, disposable items.

However, in the progress of downscaling polymer integrated photonic structures and hence optofluidic devices, it is important to provide a high refractive index contrast [4, 5]. High refractive index contrasts enable strong light confinement in the waveguide of the sensor and therefore the capability of reducing device proportions. However, due to the low refractive index contrast available between various polymer materials, the efficiency of such devices is often limited.

In general, a common method for maximizing the refractive index contrast of optical devices, is to exploit air as surrounding cladding layer of the waveguide core. Mainly, air-suspended applications have been shown in high-refractive index semiconductors realized by different etching steps of sacrificial layers [6–9]. A much more useful and less elaborated process to realize air claddings in polymer materials can be derived from various methods to realize embedded microfluidic channels of the negative-tone photoresist SU-8 using an SU-8 layer to seal a structure [10–18]. However, transferring and bonding of uncross-linked SU-8 onto SU-8 microchannels has only been shown down to film thicknesses of several micrometres [19], whereas air-suspended polymer photonic devices and optofluidic applications operating in the single-mode regime of optical waveguides, would require reduced film thicknesses down to several hundreds of nanometres [20]. Realizing air-suspended SU-8 waveguide layers with such thin thicknesses by a polymer-onto-polymer lamination method is one of the challenges addressed in this work.

In order to enable optical functionality, the transferred SU-8 layers need to contain optical structures. If such thin air-suspended single-mode waveguides can be realized, the question would arise how it would be possible to couple light into the waveguides and what methods would be suitable. Due to the small cross-sections of single-mode waveguides being often in the range of several hundreds of nanometres, interfacing the waveguide layer to optical fibres is a challenging exercise. For integrated photonic devices fabricated in semiconductors, the well-known highly efficient surface grating couplers have been proposed and realized [21]. By using such grating couplers it is possible to couple light from an optical fibre into a thin single-mode waveguide layer and back into a fibre without cleaving and polishing processes.

As mentioned above, polymers do not offer large variations in their refractive indices, which makes surface grating couplers considerably difficult to implement on a polymer based platform. However, if air-suspended, structured SU-8 films can be

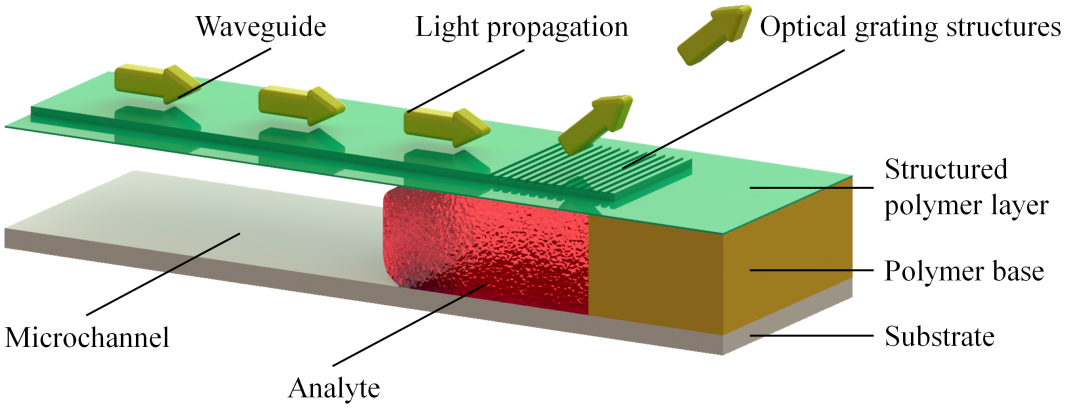

Figure 1.1: Polymer-based optofluidic sensor concept consisting of a structured polymer layer bonded onto a polymer base on top of a microchannel for maximizing the refractive index contrast. An integrated waveguide guides light towards an analyte, e.g. positioned below a sensing optical grating. The light interacts with the analyte that changes e.g. the central wavelength of the light spectrum which is then coupled out of the polymer layer by the grating for monitoring.

transferred and bonded onto SU-8 microchannels, such films would exhibit a high refractive index contrast due to the air claddings on top and at the bottom. This would potentially allow the realization of air-suspended polymer grating couplers that could provide a reasonable light coupling efficiency.

By exploiting such efficient polymer grating couplers bonded on top of a microchannel, novel polymer-based optofluidic sensor concepts and principles as shown in Fig. 1.1 could be invented and studied. This exemplary concept summarizes the challenges mentioned above. It consists of a structured polymer layer bonded onto a polymer microchannel base for maximizing the refractive index contrast between the waveguide core and the surrounding claddings. An integrated waveguide guides light towards an analyte which is e.g. positioned below a sensing optical grating. The light interacts with the analyte that changes e.g. the central wavelength of the light spectrum which is then coupled out of the polymer layer by the grating for monitoring.

In general, the detection and analysis of biochemical and biomedical species by optofluidic sensors is challenging due to short optical path-lengths that lead to weak optical absorption competing with a high background transmission, small sample volumes, and the need to analyse individual particles or molecules. Consequently, it is difficult to achieve high sensitivities and low detection limits. Hence, increasing the overlap between the optical field and the target analyte is the ulti-

mate way to improve the sensitivity of such sensors [22]. If air-suspended polymer waveguides and grating couplers can be realized, the possibility to investigate highly sensitive planar optofluidic sensors experimentally would be enabled. Such a sensor would exhibit a reduced footprint and can be exploited to probe liquid samples paving the way towards novel point-of-care optofluidic diagnostic systems.

1.2 Thesis outline

This thesis is focused on the key problems of polymer optofluidic devices identified in the introduction, namely (I) can air-suspended, high-index cladding single-mode waveguides be realised by lamination techniques; (II) can these waveguides be interfaced effectively using surface grating couplers and (III) can these grating coupler interfaced waveguides and the grating couplers themselves also be harnessed as sensing elements.

The work is divided into eight chapters that can be summarized as follows. Chapter 2 briefly reviews and describes integrated microfabrication, and especially the state-of-the art polymer processing technologies photo-, nanoimprint-, and soft lithography. Such technologies or similar alterations and modifications are mainly employed throughout this thesis. In Chapter 3 a method to bond unstructured and structured films of the epoxy-based negative photoresist SU-8 down to sub-micron thicknesses onto microchannels fabricated in the negative-tone, epoxy-based photoresist KMPR using a flexible PDMS carrier stamp is proposed and realized. By exploiting differently cast PDMS carrier stamps, flat and structured layers, approximately 0.5 μm thick, can be transferred. However, in order to exploit this approach for optical and optofluidic sensing applications, suitable methods need to be developed to use these films as waveguides and as microfluidic channels. Thus, the knowledge gained from Chapter 3 is then exploited in Chapter 4 to create air-suspended single-mode rib waveguides and butt coupling is used to demonstrate propagation of light into such thin SU-8 layers.

Chapter 5 studies the employment of air-suspended SU-8 surface grating couplers as a means to maintain the integrity of the underlying air-cavity and allow access to the optical waveguide without any further end-facet preparation. In addition to this, the behaviour of air-suspended SU-8 surface grating couplers is investigated and experimentally demonstrated in Chapter 6.

Based on the insights gained from Chapters 3-6, Chapter 7 proposes and demonstrates a selection of different highly sensitive optofluidic sensors. The first sensor concept is fully numerically simulated, experimentally realized and characterised. Two surface grating couplers are fabricated in a laminated film on top of a microfluidic channel system, where one grating coupler acts as input and the other coupler as output and sensing grating coupler for the analyte. A second more sensitive sensor concept is then proposed based on long-period gratings. Transmission calculations have shown that the sensor exhibits a very high refractive index sensitivity of 6000 nm RIU^{-1}, which would be a suitable sensitivity for novel, single-use point-of-care biomedical diagnostic systems as proposed in the motivation of this thesis. Chapter 8 presents concluding remarks and an outlook for future research.

2 Integrated microfabrication

This Chapter introduces integrated microfabrication, followed by a description of the basics of the state-of-the art polymer processing technologies. The information provided in this Chapter is a necessary basis for the following Chapters as the described polymer processing technologies or similar alterations and modifications are mainly employed throughout the thesis. Readers familiar with polymer microfabrication technologies might continue reading with Chapter 3.

2.1 Introduction

Integrated microfabrication is increasingly central to modern science and technology and can be considered as one of the key technologies of the 21st century [23, 24]. In general, microfabrication is the collection of technologies used to realise devices in the micrometer range. Especially, the invention of the transistor in 1947 sparked a revolution in microelectronics. Nowadays, transistors can be found in almost every electronic circuit with an immense degree of complexity and miniaturization. Although microfabrication has its origins in microelectronics [25] and most of the research has been focused in this field, other microfabrication disciplines have emerged rapidly. This especially includes microelectromechanical systems (MEMS) which have expanded in numerous different directions such as microsensors, microactuators, microelectronics and microstructures.

Mainly semiconductors such as silicon or gallium arsenide have been employed to create MEMS devices due to their excellent physical properties. Although silicon based microfabrication has gained tremendous interest, it is significantly limited by its material properties such as optical opacity, mechanical fragility and poor electric insulation. Over the last decade, the use of polymer materials for microfabrication became very popular as polymers offer versatile properties and mass-production capabilities and are available in numerous different types [26]. The recent developments in and by using polymers not only allow polymers to be used as a substitute for semiconductors, but also open up possibilities for new applications that could not have been realized before [26].

2.2 Polymer processing methods

In addition to the existing technologies for manufacturing of integrated microfabricated devices, the increasing interest in microstructured polymers requires equivalent fabrication technologies [27]. Numerous polymer technologies and processes for prototyping and high-throughput fabrication have been developed and established over the last decade.

The following three Subsections give a brief introduction into the standard processes for the microfabrication of polymers, namely photo-, nanoimprint-, and soft lithography, which also have been employed with minor alterations and modifications throughout this thesis. Advantages, drawbacks and limits are discussed at the end of this Chapter.

2.2.1 Photolithography

Lithography refers to the Greek words for stone *"lithos"* and to write *"gráphein"* and can be traced back to the invention in 1796 by Aloys Senefelder [28]. Nowadays, the most widely employed form of lithography is optical or photolithography. Photolithography is the dominant technology in fabrication of semiconductor devices and microelectronic systems which have high requirements on the alignment, continuity, isolation and uniformity in the final patterns [29]. In photolithography a light sensitive polymer, called photoresist, is exposed through a transparency mask containing a microstructure pattern. Afterwards, the photoresist is developed to define and form the structures on a substrate.

Fig. 2.1 shows a simplified photolithography process overview for the widely used photoresist SU-8. Initially, SU-8 is spin coated onto a silicon or glass substrate (Fig. 2.1 (a)). Afterwards, a transparency mask is employed to expose specific parts of the polymer film to ultraviolet (UV) radiation (Fig. 2.1 (b)). By using positive-tone photoresists, exposure to UV radiation changes the chemical structure of the resist and makes it soluble in developer. Thus, the exposed resist can be washed away. Negative-tone photoresists such as SU-8 behave in the opposite manner. When exposed to UV radiation, negative resists cross-link and are hence polymerized and cannot be dissolved in developer. Only the unexposed areas can be removed in developer (Fig. 2.1 (c)).

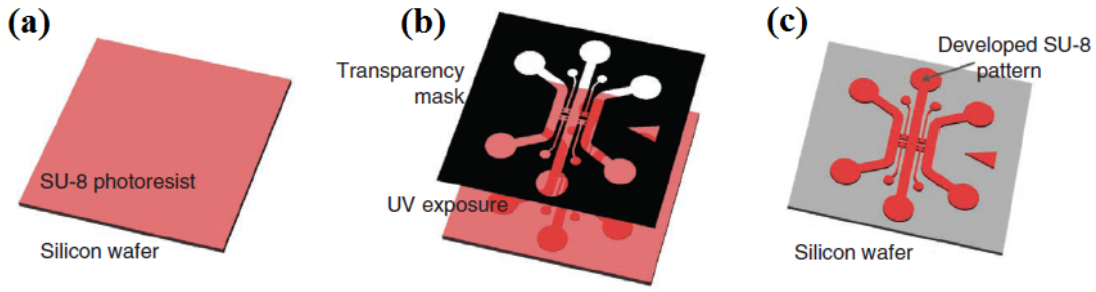

Figure 2.1: Procedure of standard photolithography. (a) Polymer photoresist spin coating and pre-baking on substrate (here: SU-8), (b) UV radiation exposure through transparency mask and (c) post-exposure bake and developing to define the structures. Reprinted by permission from Macmillan Publishers Ltd: Nature Protocols 7:1247-59, copyright 2012, Ref. [30].

2.2.2 Nanoimprint lithography

Nanoimprint lithography (NIL) is an attractive, widely researched, non-conventional lithographic method for high-throughput, high-resolution parallel patterning of polymer micro- and nanostructures [31, 32]. Unlike traditional lithography using photons or electrons to modify the chemical and physical properties of a photoresist, NIL relies on a stamp that contains a surface pattern that is replicated into a polymer material by direct mechanical deformation of the resist. This can enable resolutions beyond the limitations set by the light diffraction in the sub-10 nm range [33] and is only limited by the manufacturing abilities of the NIL stamp.

Fig. 2.2 shows a schematic of the originally proposed NIL process [33]. First a patterned stamp or mold is pressed into a layer of resist that has been spin coated onto a substrate, thereby creating a thickness contrast in the resist material. The nanostructured stamp employed in NIL can be fabricated for example by optical lithography or electron beam lithography and dry etching [34]. A thin residual layer of resist is always left underneath the stamp protrusions and can, if required, be removed by an anisotropic etching process for example reactive ion etching (RIE) or wet etching.

In general, NIL can be divided into thermal NIL (or hot embossing) and UV-NIL. In thermal NIL, a thermoplastic polymer is heated above its glass transition temperature in order to soften the material. When the polymer is soft, it behaves as a viscous liquid that can flow between the stamp protrusions when the stamp is pressed into the material. After cooling down the polymer and the mold, the

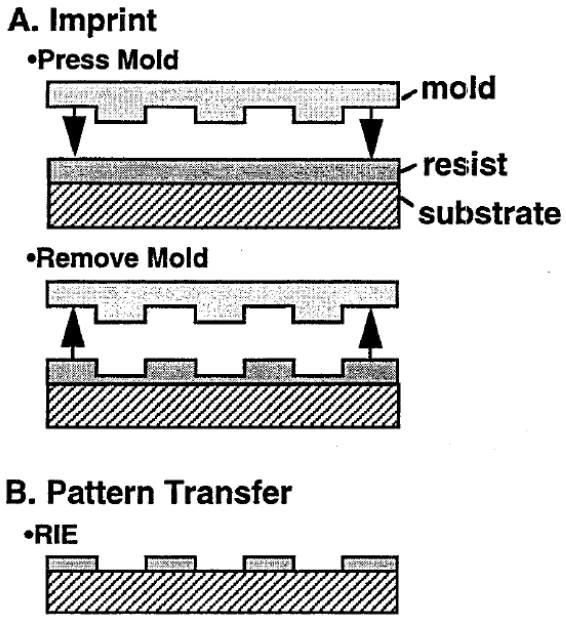

Figure 2.2: Schematic of the originally proposed nanoimprint process. (a) Imprinting a mold into a resist to create a contrast in thickness, and (b) pattern transfer using anisotropic etching, for instance reactive-ion etching (RIE), to remove residual resist in the imprinted areas. Reprinted with permission from Chou, S. Y., J. Vac. Sci. Technol., B 15:(6) 2897 (1997). Copyright 1997, American Vacuum Society, Ref [33].

structures can be demolded [35]. In UV-NIL low viscosity UV-curable resists are patterned by transparent molds and UV radiation using the same principle of pressing a mold into a resist, resist curing and separation of resist and mold. Key features and differences of UV-NIL to thermal NIL are the faster curing time at room temperature, which is important to avoid thermal expansion, the lower pressure that has to be employed for imprinting and the simplified alignment due to the transparent stamps [36]. The interested reader is referred to following publications [31, 32, 34, 36].

2.2.3 Soft lithography

Soft lithography can be viewed as a complementary extension of photolithography and is a collective name that refers to a set of techniques for microfabrication including replica molding, micro-contact printing (μCP), micro-molding in capillaries (MIMIC), micro-transfer molding (μTM), solvent-assisted micromolding (SAMIM) and near-field conformal photolithography [28, 37].

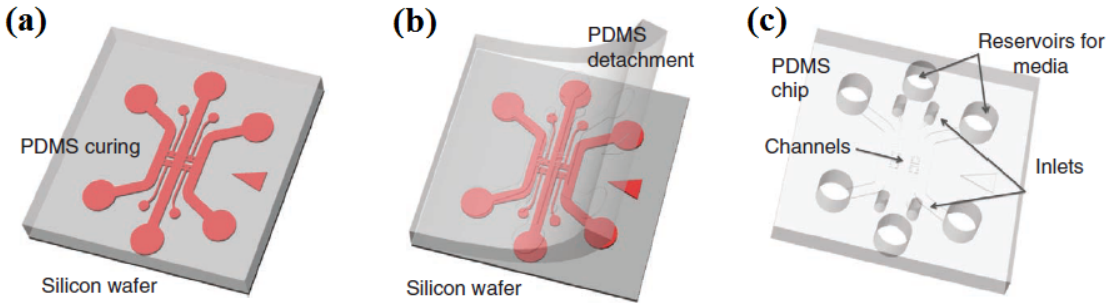

Figure 2.3: Soft lithography stamp fabrication by replica molding. (a) PDMS is mixed and poured onto an SU-8 mold and cured, (b) peeling off cured PDMS and (c) preparing the final device with access holes and inlets. Reprinted by permission from Macmillan Publishers Ltd: Nature Protocols 7:1247-59, copyright 2012, Ref. [30].

In general, soft lithography provides a convenient, effective, and low-cost method for the formation and manufacturing of micro- and nanostructures with feature sizes ranging from 30 nm to 100 μm [37]. Unlike photolithography, a wide range of elastomeric "soft" materials can be processed. Nowadays, polydimethylsiloxane (PDMS) elastomer is a widely used material in soft lithography but also polyurethanes, polyimides, and cross-linked Novolac^{TM} resin have been used [37]. PDMS has a very low glass transition temperature and is liquid at room temperature and can be readily converted into solid elastomers by cross-linking [37]. The formulation, fabrication, and applications of PDMS elastomers have been extensively studied and are well-documented in the literature [38].

Soft lithography is based on printing and molding of elastomeric stamps with the patterns of interest. The key strategy for fabricating such stamps and molds is to replicate patterned surfaces in an elastomer as shown in Fig. 2.3. Initially, for example PDMS is mixed and poured onto an SU-8 mold and cured as shown in Fig. 2.3 (a). After curing, PDMS can be peeled off (Fig. 2.3 (b)) and directly employed as shown in Fig. 2.3 (c) or further used for the soft lithography methods mentioned above. These techniques are not further explained here as the PDMS fabrication employed in this work is explained in detail in Chapter 3.
The interested reader is referred to the following publications [28, p.138 ff.], [37, 39].

2.3 Advantages, drawbacks and limits of polymers

In comparison to semiconductor materials, polymers offer several exceptional advantages. First, a large pool of different polymers with different specific properties are available at significantly lower costs [40]. Furthermore, most polymers are optically transparent to visible and UV light. Due to their small Young's modulus, polymers are soft materials allowing simple fabrication of flexible structures at low processing temperatures. The low material and fabrication costs combined with the biocompatibility [41, 42] to active molecules and living cells of most polymers, makes this material class very suitable for single-use, disposable devices such as biosensors. This allows one to eliminate the risk of sample or analyte contamination. Furthermore, polymers can offer excellent chemical stability and the surface chemistry such as the wettability can be easily modified compared to semiconductors depending on the desired application.

However, the huge diversity of different available polymers offering a broad range of chemical, mechanical, electrical and optical properties as well as the multitude of different methods to manufacture microstructures makes the selection of the optimal material a very challenging task [27]. Generally, polymers are electrical and thermal insulators and exhibit a low thermal stability. Very often the mechanical softness, the limited thermal range and the porosity of polymers are mentioned to be the main drawbacks of polymer materials. Polymers can absorb water and solvents and can swell and thus deform precise microstructures. Several polymers exhibit a poor chemical tolerance. Although the flexibility and softness of polymers have advantages, both properties are limiting polymer electronics applications and can not achieve the performance of semiconductor devices. Furthermore, the methods for fabrication on the micro-scale are not as well developed as semiconductor processes. Due to high tolerances and the low refractive index contrast available for conventional polymers, polymers are very often not very suitable for microoptical applications.

The major challenge of the microfabrication of polymer structures is the transfer from the prototypes of the academic environment to commercial products. There is an increasing gap between methods and materials between the two worlds as in academia many processes are carried out manually, whereas the technology preferred by the industry would be automated injection molding using thermoplastic materials. Transferring processes developed in academia to industry is quite chal-

lenging as the processes cannot directly be transformed into commercial devices due to the different chemistries and physical parameters involved [27].

2.4 Conclusions

This Chapter briefly reviewed techniques for polymer microfabrication. During the last decade, the use of polymer materials for fabrication of microstructures has become very popular due to moderate costs and simple processing. Especially the research areas of integrated microfluidics, photonics, and optofluidics have highly profited from new technologies such as photo-, nanoimprint-, and soft lithography. The mentioned technologies have been introduced and explained as they or similar alterations and modifications are mainly employed throughout the thesis.

3 Polymer onto polymer bonding

This Chapter motivates and proposes a method to bond unstructured and structured films of SU-8 down to sub-micron thicknesses onto microchannels fabricated in KMPR using a flexible PDMS carrier stamp. By exploiting this method and by using differently cast PDMS carrier stamps, it should be possible to combine fluid handling in microchannels and photonic structures realized in the laminated SU-8 layer. This can create new features and thus enable research towards a large range of applications in microfluidics, optics and optofluidics. The knowledge gained from the bonding of SU-8 films is the base for the subsequent Chapters of this thesis where this method is further exploited for photonic and optofluidic applications.

An introduction of the employed materials is given in the first Section, followed by the main part which is adapted from the published journal paper *"Bonding of SU-8 films onto KMPR structures for microfluidic, air-suspended photonic and optofluidic applications"* [43]. The fabrication of the different types of employed PDMS carrier stamps as well as the complete bonding process steps are presented. Important process details are discussed. Bond strength tests are carried out and a simple application of a microfluidic mixer is demonstrated.

3.1 Introduction

Bonding technologies play a major role in the fields of 3D integrated circuits, microelectromechanical systems (MEMS) and integrated microfluidics. While various bonding methods such as metal diffusion, eutectic, silicon direct or hybrid bonding are mainly used for MEMS packaging and 3D integration, adhesive and especially polymer bonding are more common in the field of integrated microfluidics [44]. Depending on the employed fabrication method of microfluidic devices, the sealing of the open structures is in most cases required in order to achieve enclosed microfluidic channels making the bonding process a critical step in the fabrication process. Besides the critical bond strength, the requirements on a bonded interface can include chemical or solvent compatibility, material compatibility or optical properties [45].

Microfluidic bonding techniques can be divided into indirect and direct methods. During direct bonding, a similar or dissimilar thermoplastic substrate such as

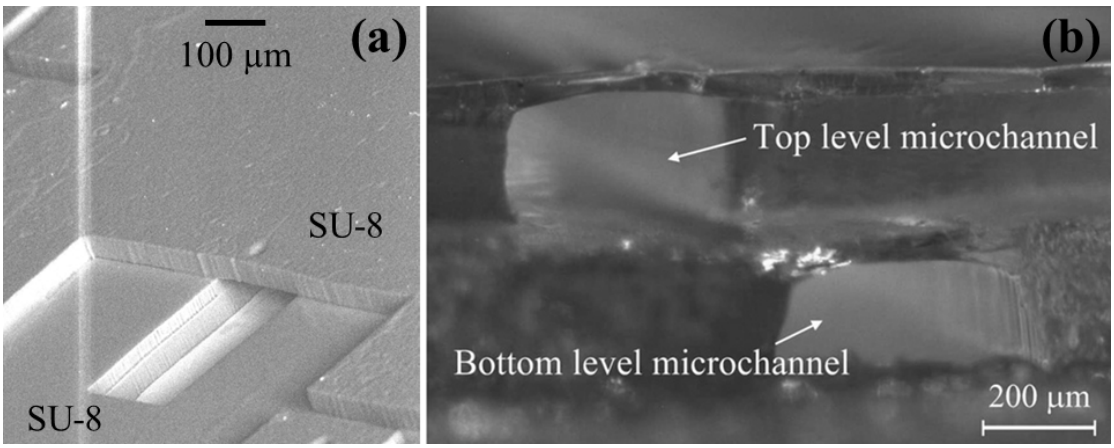

Figure 3.1: SU-8 onto SU-8 microchannel bonding using (a) a Pyrex foil [13] and (b) an acetate foil with PDMS [19]. Fig. 3.1 (a) Reprinted by permission from ©IOP Publishing: Journal of Micromechanics and Microengineering 14(7):1047-1056, copyright 2004, Ref. [13]. All rights reserved. Fig. 3.1 (b) Reprinted by permission from ©IOP Publishing: Journal of Micromechanics and Microengineering 20(3):035008 (7pp), copyright 2010, Ref. [19]. All rights reserved.

PC [46, 47], PMMA [48, 49], COC [50, 51] or polystyrene [52] is heated above its glass transition temperature (T_g) and brought into contact with the microchannel structure while applying pressure to increase the contact force between the materials. The diffusion of the polymer chains of the surfaces of the microchannels and the substrate generate strong bonds making this thermal bonding method the most commonly employed method for sealing microfluidic channels [45]. Indirect bonding techniques involve an intermediate adhesive layer including UV-curable glue, epoxy or acrylate that polymerizes and cross-links and thus cures between the microchannel structures and the sealing material [45]. Another adhesive bonding method for microfluidic devices is the lamination of both liquid and dry films of polymers. During liquid film lamination, a polymer cover is coated with an thermally activated adhesive material which is then activated at elevated temperatures (100-150 °C), allowing effective wetting of the bonding surface to encourage strong bonds [45]. Also pressure sensitive adhesive films flowing at room temperature are available for both liquid and dry film lamination. Dry film lamination is more commonly employed in microfluidics and usually exploits an uncured (uncross-linked) photoresist such as SU-8 to seal microfluidic channels. Numerous SU-8 bonding methods to seal SU-8 microfluidic channels have been reported including utilizing a commercial lamination foil [10, 53], polyethylene terephtha-

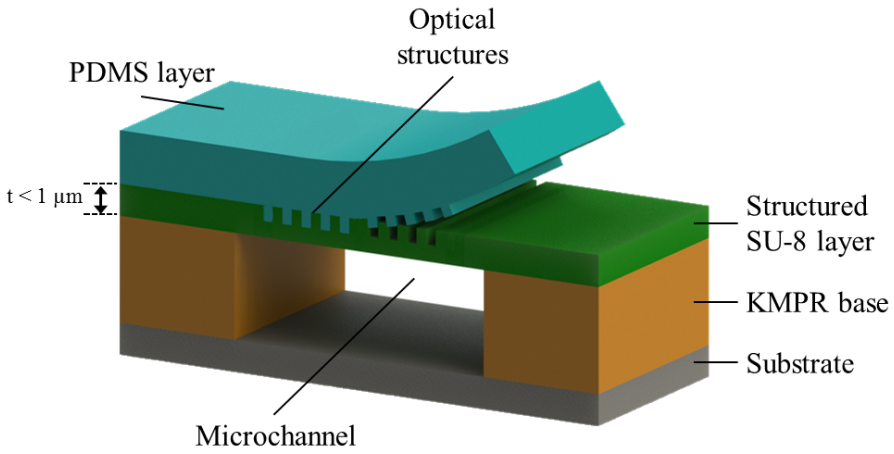

Figure 3.2: Schematic of the proposed bonding method of structured SU-8 layers onto KMPR microchannels using a PDMS layer (not to scale).

late (PET) [11, 12], Pyrex [13, 14], Kapton [15, 16], polyimide [17], Borofloat glass [53] or PDMS [18, 19, 53]. Transferring and bonding of uncross-linked SU-8 onto SU-8 microchannels has been shown [11, 17–19, 53] down to a film thickness of approximately 5 μm [19].

To exploit an SU-8 bonding method not only for microfluidics but also for optical applications and hence for optofluidics, the laminated film (I) needs to contain optical structures, (II) should provide a smooth and uniform surface and (III) most importantly, the film thickness needs to be reduced to several hundreds of nanometres according to the single-mode condition [20] as most applications require the light guided under these conditions. However, the lamination of structured SU-8 layers has not yet been reported and some of the reported methods using a foil as lamination tool exhibit rough surfaces as shown in Fig. 3.1 (a).

The most promising method to achieve smooth transferred layers is employing PDMS as interlayer between the lamination foil and the SU-8 to be transferred similar as illustrated in the schematic of the proposed bonding method in Fig. 3.2. By using such methods, film thicknesses down to approximately 5 μm have been realized (Fig. 3.1 (b)) [19]. Furthermore, the lamination of KMPR onto KMPR, a very similar photoresist to SU-8, was achieved using a conformal adsorbate film and PDMS [54]. That SU-8 and KMPR can be laminated due to their similar chemical structures has been only predicted but not experimentally realized [55]. However, such laminated films could be very interesting for optical applications, due to the lower refractive index of KMPR.

In the following a bonding method of uncross-linked SU-8 photoresist layers down to sub-micron thicknesses involving KMPR and PDMS, comparable to the illustration shown in Fig. 3.2, is reported after a brief introduction of all employed materials. After a thorough review of the literature, it would appear that this is the first experimental realization of the bonding of structured and unstructured SU-8 films below 1 μm of thickness. In contrast to the SU-8 lamination methods mentioned above, thin SU-8 films are transferred and bonded onto KMPR structures by using a flat or patterned PDMS carrier stamp.

3.2 Materials

In integrated microfabrication and rapid-prototyping towards mass-producible miniaturized devices, polymer materials became a key technology due to low-cost as well as rapid and flexible processing. As a result, most of the recent microfluidic devices have been fabricated by soft lithography particularly with the widely used elastomeric polydimethylsiloxane (PDMS) [56]. Furthermore, the negative-tone, epoxy-based photoresist SU-8 was found to be suitable [57, 58] and is nowadays of great popularity in the research community. The simple and easy processing of PDMS and SU-8 allow the fabrication of almost any desired shape and structure. SU-8, KMPR and PDMS have been chosen due to the bonding capabilities and due to the wide spread use of the materials which makes the developed bonding technique easily adaptable and compatible with other reported processing methods. In the following the employed materials are briefly introduced.

3.2.1 SU-8

SU-8 was originally developed as resin composition for electron beam lithography and has been patented in the 1980s by the IBM T. J. Watson Research Center in Yorktown Heights (US patent no. US4882245 A, 1989) [59]. SU-8 is a chemically amplified epoxy-based, highly sensitive, negative-tone photoresist which is sensitive to near UV radiation [58, 60–62], X-rays [63] and also high-energy particles (an electron beam) [64]. Uncured SU-8 consists of a multifunctional, highly branched polymeric epoxy resin dissolved in an organic solvent, along with a photoacid generator. The molecular structure contains eight benzene rings and eight epoxy groups as shown in Fig. 3.3 with a monomer molecular weight of around 7 kDa [65].

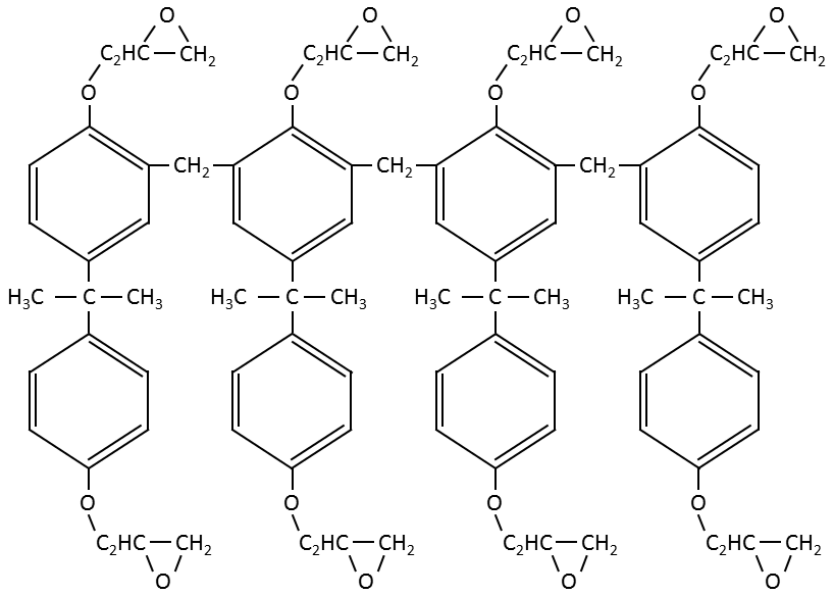

Figure 3.3: Molecular structure of the negative-tone, epoxy-based photoresist SU-8 containing eight benzene rings and eight epoxy groups.

SU-8 can be spin coated in thicknesses ranging from thin films of a few hundreds of nanometres to very thick films up to 2 mm by multilayer coatings [66]. Exposure to radiation produces a low concentration of a strong acid serving as a catalyst in the exposed regions during the cross-linking process. The polymerization of SU-8 is cationic, meaning the acid produced during the exposure does not cross-link until the post-exposure bake (PEB) [67]. Since SU-8 is a negative-tone photoresist, only the exposed parts contain the acid catalyst and thus remain after the subsequent resist development. In the exposed areas, extensive cross-linking occurs, forming a dense network that is resistant to solvents and prevents resist stripping [68]. Unexposed parts can be dissolved by a developer.

SU-8 has very good physical properties being an electrical insulator (breakdown field ≈ 108 V m^{-1}), optically transparent with a refractive index of $n_{SU\text{-}8} \approx 1.575$ at $\lambda = 1550$ nm, reasonably rigid with a Young's modulus around 3-4 GPa [69] and is not too brittle. It has good chemical resistance to most solvents and inorganic products such as acids and bases and has an excellent thermal stability making it well suited for permanent use applications. Furthermore, SU-8 and its MEMS processing methods have been proven to be biocompatible and suitable for implantable medical [70], MEMS drug delivery [41], cell cultures [71, 72], chip-based DNA [73] and biosensor devices [74, 75].

However, SU-8 suffers from three main disadvantages, namely adhesion selectivity, internal stress and its chemical resistance becomes a disadvantage making it almost impossible to strip cross-linked resist from a wafer to perform subsequent patterning. The adhesion is good on materials such as silicon or gold, but on other materials such as glass, oxides, and other metals, the adhesion is poor and SU-8 can easily de-laminate during the development process. Large amounts of stress can be introduced to the interface of a substrate and the SU-8 resist during the temperature induced cross-linking process due to a large thermal expansion coefficient mismatch. Additionally, it is difficult to remove or strip SU-8 after cross-linking.

In the 1990s, SU-8 was first employed to fabricate MEMS devices by the EPFL Institute of Microsystems and IBM in Zurich [58, 60, 61]. Since then, SU-8 finds its applications in several MEMS areas, such as high aspect ratio (100:1) features [63], microchannels [76, 77], multilayer structures [62, 78–80], integrated waveguides [81], optoelectronics [82], functional MEMS devices [62], NEMS [83], multi-layer microstructures, [80] embedded microchannels [76], microfluidics [84, 85], biological [86] and mechanical [87] sensors, or lab-on-a-chip devices [88, 89].

3.2.2 KMPR

KMPR is a chemically amplified, thick film, negative-tone, epoxy-based photoresist which has been developed by Microchem Corp. and Nippon Kayaku Co. Ltd. in 2004 [90] to resolve the stripping problem of SU-8 [91]. KMPR is processed similar to SU-8, but is easier to pattern, displays better adhesion to substrates [91–93], has an increased moisture resistance [94] and requires shorter baking conditions without the risk of cracking [95]. Unlike SU-8, KMPR can be developed in aqueous developers instead of solvent-based developers and can be easily stripped even after a hard baking process [95, 96]. Furthermore, KMPR has a lower refractive index with $n_{KMPR} \approx 1.55$ at $\lambda = 1550$ nm. Like SU-8, KMPR is also optically transparent and has high chemical, plasma and dry etch resistance [97].

KMPR has been used for several applications such as microfluidic structures [98], RIE masking layers [97, 99], electrodeposition molds [100, 101], proton beam writing [102], absorbance filters for microfluidics (when mixed with appropriate dyes) [103] and structural materials in radiation imaging detection [92]. The molecular structure of KPMR is proprietary and not published.

3.2.3 PDMS

The first silicones have been synthesized in the 1950s [104]. Nowadays, polydimethylsiloxane (PDMS), a silicone elastomer, is the most widely used silicone-based polymer for the fabrication and prototyping of MEMS and microfluidic devices [105, 106]. PDMS consists of methylated linear siloxane polymers containing repeating units of the monomer $(CH_3)_2SiO$, with trimethylsiloxy end-blocking units of $(CH_3)_3SiO$ as shown in Fig. 3.4, where n is the number of monomers repetitions.

PDMS items are mainly fabricated by soft lithography through replica molding or polymer casting as explained in Section 2.2.3. PDMS has a very low glass transition temperature and is liquid at room temperature and can be readily converted into solid elastomers by cross-linking [37]. In the fabrication process, a prepolymer mixture of PDMS and its curing agent is prepared and cast against a master mold. The prepolymer is then cured in an oven at elevated temperatures of 60-75 °C and peeled off from the master, resulting in a negative replica of the master in PDMS. Because such masters are typically rigid, the use of the flexible PDMS facilitates separation of master and replica [107]. Holes to access, for example, microfluidic reservoirs can be included into the replication process by placing posts or can be punched out of the cured PDMS device by using a manual puncher.

Due to the hydrophobic nature of cross-linked PDMS elastomer, which limits the use of PDMS in many applications, a post-fabrication treatment using plasma is very often carried out. Oxygen plasma treatment can be used for the formation of an oxidised surface layer with polar functional groups, mainly silanol groups (SiOH) [108], which changes the surface properties of PDMS from being hydrophobic to hydrophilic [109]. Such hydrophilic PDMS surfaces are very often employed to bond PDMS to glass. However, plasma treated PDMS surfaces recover within several minutes [110] and an extended plasma treatment can induce undesirable surface cracks [108].

The main characteristics of PDMS are that it is chemically inert, nontoxic, thermally stable, optical transparent, permeable to gases, simple and easy to produce and handle at lower cost than silicon [37, 106, 111]. Furthermore, PDMS is biocompatible and is indeed sometimes used as a food additive [42, 112]. A major disadvantage of PDMS is its intrinsic hydrophobicity limiting the use of PDMS for applications which require hydrophilic surfaces such as chemical synthesis, the

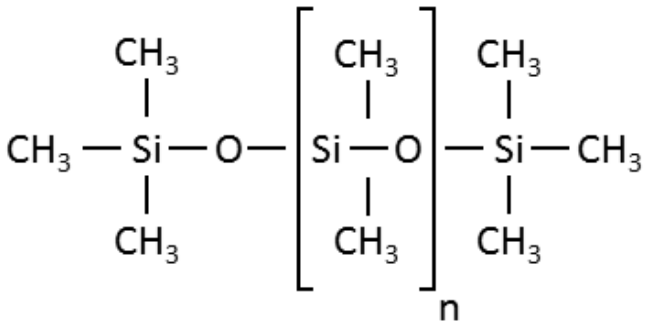

Figure 3.4: Molecular structure of polydimethylsiloxane (PDMS).

analysis of biological samples [113] or electrophoretic separation [56]. Other disadvantages are the absorption of organic solvents and small molecules, and the evaporation of water [114].

Applications of PDMS can be found in numerous research disciplines, including the wide field of microfluidics [115], MEMS [116], optical MEMS [117] and bio-MEMS [118]. Two types of PDMS are commonly used in the research community, namely RTV 615 from Bayer Silicones and Sylgard 184 from Dow Corning. The exact composition of both materials is confidential, however, RTV 615 is more robust and convenient to bond layers of PDMS, but has the reputation for being unclean. In contrast, Sylgard 184 is cleaner, but the bonding of PDMS layers is more difficult [119].

3.3 Bonding of SU-8 films onto patterned KMPR

In order to bond SU-8 films for microfluidics, optics and optofluidic applications, three objectives need to be considered: (I) it should be possible to transfer structured films which could possibly contain photonic structures, (II) the laminated films should be relatively smooth to avoid disturbing the guidance of light in the bonded SU-8 layer and (III) it should be possible to transfer film thicknesses down to several hundreds of nanometres in order to meet the single-mode condition of infrared light.

Furthermore, the lamination of SU-8 onto KMPR can possibly be interesting for optical applications due to the lower refractive index of KMPR ($n_{KMPR} \approx 1.55$) compared to SU-8 ($n_{SU\text{-}8} \approx 1.575$) at $\lambda = 1550$ nm, while maintaining many other very similar materials properties.

The developed SU-8 onto KMPR bonding method can be divided into three main steps. First, a KMPR photoresist layer can be structured as the bottom layer on a silicon or glass substrate by standard contact photolithography (Section 2.2.1). In the experiments, a KMPR film is fully processed as an open microchannel that acts as the basis for the subsequent bonding of an SU-8 layer using a PDMS carrier stamp. In contrast to other publications using a thin, unstructured PDMS layer employed on a transparent backplane of PMMA [53] or acetate [19] for bonding of SU-8 films onto SU-8 microchannels, the transfer of the SU-8 film onto the KMPR features obtained in the first step are carried out by utilizing directly a PDMS carrier stamp. The third main step is the bonding or lamination process. In order to laminate an SU-8 layer onto KMPR microchannels, SU-8 is spin coated onto the PDMS carrier stamp and is subsequently soft baked and exposed by UV radiation. This activates the SU-8, but actual cross-linking will only occur when the temperature is elevated during the post-exposure bake. The activated, but uncross-linked SU-8 layer applied on the PDMS carrier stamp is then placed on top of the KMPR microchannel structures. By applying sufficient heat and pressure, the SU-8 layer cross-links on the KMPR structures and finally the PDMS carrier stamp can be peeled off and the SU-8 film remains bonded on the KMPR. Additional standard photolithography and lamination steps can be carried out on top of the transferred layer in order to create more complex structures.

In the following Subsections the preparation of different PDMS carrier stamps and the procedure of the bonding method is explained in detail. All fabrication steps involve standard clean room equipment and processes.

3.3.1 Preparation of PDMS carrier stamp and patterned KMPR basis

Three different PDMS carrier stamp configurations have been employed in this work: (I) flat unstructured stamps; (II) structured stamps; and (III) PDMS stamps with an embedded photo mask made of PET foil. All PDMS carrier stamps are fabricated using polymer casting as explained in Section 2.2.3.

Using a PDMS carrier stamp for the transfer of an uncured SU-8 film is beneficial since PDMS does not carry any chemical groups that can react with the epoxy groups of SU-8. Even an oxygen plasma treatment of the PDMS surface does not change the nature since the silanol groups generated on the PDMS surface do not react with the epoxy groups of SU-8 [120]. In addition to this effect, the dense

network of cross-linked SU-8 helps to achieve the lamination of thin SU-8 layers.

3.3.1.1 Preparation of unstructured PDMS carrier stamps

The simplest stamp is an unstructured PDMS carrier stamp cast from a thin SU-8 layer applied on a silicon wafer to ensure good removal of PDMS as shown in Fig. 3.5 (a). Even though, in principle, it would be possible to use a blank silicon wafer as the unstructured mould, in practice an unpatterned layer of SU-8 is applied on a silicon wafer to maintain similarity with subsequent structured SU-8 moulds. Accordingly, a 500 nm thick SU-8 layer (diluted SU-8 2050, MicroChem Corp.) is spin coated on a 4 inch silicon wafer at 3000 rpm for 30 s. The sample is subsequently soft baked on a hotplate for 1 min at 95 °C, flood exposed by UV radiation with an intensity of 70 mJ cm^{-2} using a mask aligner (EVG 620, EV Group GmbH), and finally post-exposure baked on a hotplate for 1 min at 95 °C.

Having completed the unstructured SU-8 mould, the PDMS carrier stamp to be cast against this mould is prepared. A 10:1 mixture of PDMS (Sylgard 184 Silicone Elastomer Kit, Dow Corning Corp.) with its curing agent is then stirred and placed in a vacuum chamber to degas trapped air bubbles. A polymethylmethacrylate (PMMA) frame is placed onto the prepared unstructured SU-8 mold. Afterwards, PDMS is poured into the PMMA frame and is cured for 2 h at 75 °C in an oven under vacuum conditions. Casting PDMS carrier stamps individually using the help of a PMMA frame is advantageous as the side walls of a fully cross-linked and released PDMS carrier stamp appear absolutely clear. Such side walls are favourable as they provide a clear view when the PDMS carrier stamp is later brought in contact with the KMPR structures. Furthermore, clear sidewalls help to apply the required process pressure. In order to apply uniform pressure to the sample, the PDMS carrier stamp needs to be flat. Hence all edges are removed by cutting the edges at an angle of 45°. Then the PDMS carrier stamp is ready for the SU-8 onto KMPR bonding process (details in Section 3.3.2).

3.3.1.2 Preparation of structured PDMS carrier stamps

The fabrication of the second PDMS carrier stamp configuration is shown in Fig. 3.5 (b). Here, the final PDMS carrier stamp is a replication of an electron beam lithography written pattern on a silicon master.

First, an electron beam lithography pattern is formed from PMMA electron beam resist on a silicon wafer and subsequent ion beam etching (IBE). In this case, the electron beam patterning was performed by a collaborator, Bert Laegel and Sandra Wolff from the Nano Structuring Center of the University in Kaiserslautern, Germany. The silicon master is not used directly as a mould for the PDMS carrier stamp and in order to reduce wear on the master, a perfluoropolyether (PFPE, Fomblin, Solvay Solexis S.p.A.) working mould is cast firstly. To create the working mould, PFPE is mixed with the photo initiator Darucur 1173 (Bodo Moeller Chemie GmbH) with 1 % by weight and stirred and out-gassed in a vacuum chamber (desiccator) to remove trapped air bubbles. The mixture is then poured onto the silicon master which has a mono-layer of anti-sticking material on top. The anti-sticking layer (ASL) is formed by dispensing the ASL solution (confidential solution by EV Group GmbH) containing hydrofluoroether (HFE) solvent onto the silicon wafer. After a dwell time of 30 sec, the wafer is spun at 2000 rpm in a spin coater while rinsing with the HFE solvent. This procedure results in a anti-sticking mono-layer.

Since the PFPE film is very thin, it will not support its own weight once removed from the silicon master and so a glass substrate is placed on top of the PFPE and the working mould is flood exposed by UV radiation with an intensity of 850 mJ cm^{-2} to cross-link the PTFE. After separation and rinsing with isopropanol, the sample is blown dry using nitrogen.

Having prepared the PTFE working mould, the structured PDMS carrier stamp is prepared similarly to the unstructured PDMS carrier stamp (Section 3.3.1.1).

3.3.1.3 Preparation of PDMS carrier stamps with an embedded photo mask

In the third method to prepare a PDMS carrier stamp shown in Fig. 3.5 (c) where an embedded photo mask made of PET foil is implemented into the PDMS carrier stamp in order to be able to fabricate for example three-dimensional microfluidic channel networks.

First, a flat PDMS carrier stamp is fully processed as described in Section 3.3.1.1. Then a thin PDMS adhesion layer is spin coated onto the unstructured PDMS carrier stamp at 3000 rpm for 30 s. Subsequently, the PET foil is placed on top and the carrier stamp is cured for 20 min at 75 °C in an oven. To encapsulate the

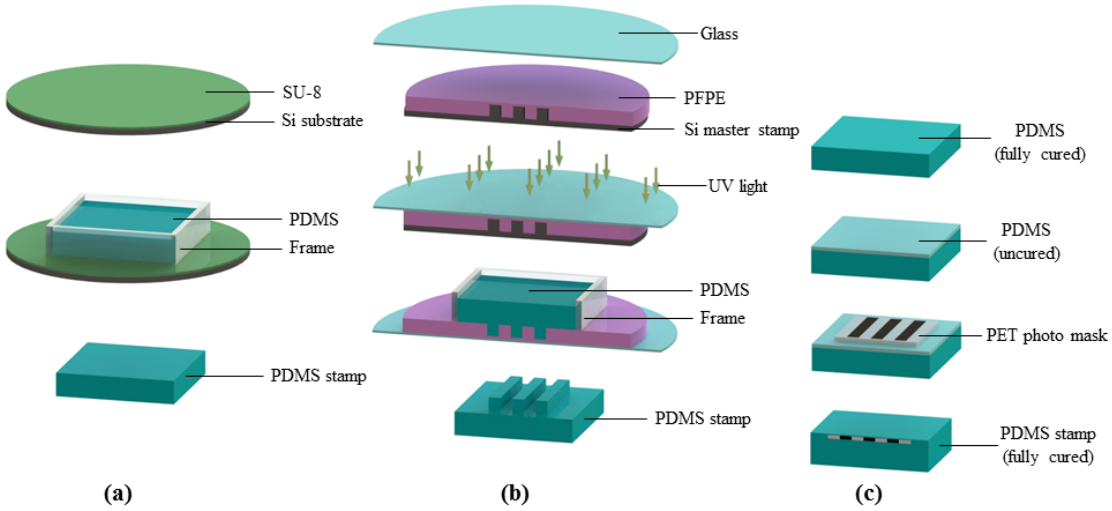

Figure 3.5: Different PDMS carrier stamp fabrication methods (not to scale): (a) standard PDMS casting of a flat carrier stamp from an SU-8 layer applied on a silicon wafer, (b) PDMS casting of structured carrier stamps from a PFPE working mould with glass backplane cast from an electron beam lithography written silicon master, and (c) PDMS carrier stamp fabrication combined with an embedded photo mask made of PET foil.

PET film with PDMS, a second PDMS layer is spin coated on top of the PET foil at 2000 rpm for 30 s and is cured for 2 h at 75 °C. Then the PDMS carrier stamp is cut to size for the bonding process.

3.3.1.4 Preparation of patterned KMPR basis

Prior to the bonding process, KMPR microchannels have been fabricated as the basis for the transfer of the SU-8 layer. First, a 25 μm thick KMPR film (KMPR 1025, MicroChem Corp.) is spin coated on a silicon wafer at 3000 rpm for 30 s. Here, the edge bead occurring at the edge of the wafer should either be removed during the spin coating process or alternatively, the photo mask used to expose the structures should cover the edge bead in order to remove it during the subsequent development process. After spin coating the KMPR film, the sample is soft baked on a hotplate ramped from 55 °C to 100 °C in steps of 5 °C with 3 min hold and cooled down to room temperature. The KMPR layer is then exposed through a photo mask containing the microchannel pattern by UV radiation with an intensity of 650 mJ cm^{-2} and is post-exposure baked for 3 min at 100 °C. The KMPR microchannels are then developed in mr-600 developer (micro resist

technology GmbH) for 2.5 min, rinsed with fresh developer and isopropanol and dry blown using nitrogen. Rinsing the sample with fresh developer is necessary to remove residual KMPR and to reduce the possibility of scumming which can be seen visually as a white film on the sample.

3.3.2 Procedure for bonding thin SU-8 layers onto patterned KMPR

Having created the PDMS carrier stamp (Section 3.3.1) and the underlying patterned KMPR structure (Section 3.3.1.4), it is now possible to describe how the PDMS carrier stamp can be used to laminate a thin film of SU-8 onto the underlying patterned KMPR structure.

The bonding procedure starts with a plasma treatment (PDC-002, Harrick Plasma Inc.) of a previously prepared PDMS carrier stamp for 3 min using ambient air in order to promote adhesion for SU-8. Subsequently, an SU-8 layer (diluted SU-8 2025, MicroChem Corp.) is spin coated onto the PDMS carrier stamp and soft baked in an oven depending on the targeted film thickness. After cooling down to room temperature, the SU-8 layer is flood exposed by UV radiation. Then the transfer and bonding of the SU-8 film is carried out as shown in Fig. 3.6.

When alignment is not required, the PDMS carrier stamp can be simply placed on top of the structured KMPR microchannels on a hotplate (Fig. 3.6 (a)). In order to align structured PDMS carrier stamps, an alignment tool has been constructed by combining a rotation stage and three translation stages (XYZ) with a microscope (LEXT OLS4000, Olympus GmbH). However, it is important that the microscope has a high-end camera system with a large contrast range to be able to image the structures in the PDMS carrier stamp when covered by the SU-8 film. Due to the small refractive index contrast between PDMS ($n = 1.399$ [121]) and SU-8 ($n = 1.575$ [122]) not every conventional microscope can be used for alignment.

After alignment, the sample is placed on a hotplate. Pressure depending on the carrier stamp geometries and feature sizes is then applied by placing steel blocks of different weights on top of the PDMS (Fig. 3.6 (b)). The weight is increased slowly on top of the PDMS carrier stamp until full contact between the KMPR microchannels and the SU-8 film can be observed.

In order to cross-link and therefore bond the uncured SU-8 layer onto KMPR, a post-exposure bake (lamination bake) is carried out by ramping the hotplate from 55 °C to 95 °C and holding the temperature until the SU-8 is fully cured. Here,

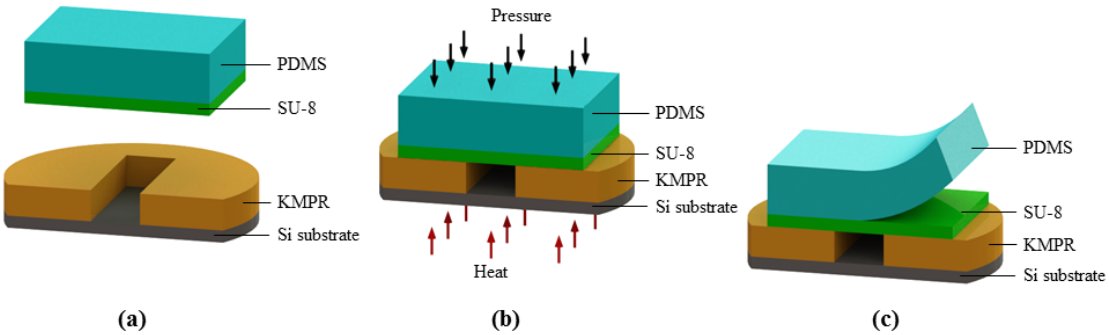

Figure 3.6: Basic principle of SU-8 lamination onto KMPR microchannel structures (cross-section, not to scale): a) deposition of SU-8 onto a PDMS carrier stamp by spin coating, and definition of KMPR microchannels by standard photolithography; b) cross-linking of SU-8 on KMPR microchannels by applying pressure and heat; c) peeling off the PDMS carrier stamp whereby the SU-8 layer remains bonded on the KMPR microchannels.

the baking time depend on the film thickness. Afterwards, the steel blocks can be removed and after cooling down the sample to room temperature, the PDMS carrier stamp can be peeled off and the cured SU-8 film remains bonded on the KMPR microchannel structures (Fig. 3.6 (c)).

The chemical process that enables the bonding of the SU-8 layer onto KMPR can be explained by the following hypothesis. For post-exposure baked SU-8 it was found that if it is not fully cured, it can still carry residual epoxy-groups that are reactive [120]. It is assumed that the same effect occurs with KMPR, processed as described in Section 3.3.1.4, as it is similar to SU-8. According to this, the KMPR microchannel structures still carry a significant amount of residual, reactive epoxy groups. Thus, during the bonding process, molecular segments of KMPR and uncured (uncross-linked) SU-8 of the layer to be laminated can diffuse into each other and cross-link.

Finally, a hard bake at 175 °C for 1 h is carried out for all samples. Optimized soft bake, exposure and lamination bake parameters in respect to the temperature and humidity conditions of the clean room facility of the Karlsruhe University of Applied Sciences (21 °C, 40 % RH) are listed in Tab. 3.1.

SU-8 film thickness	0.5 μm	2 μm	5 μm
SU-8 mixture	SU-8 2000.5	SU-8 2002	SU-8 2005
Spin speed (rpm), cycle 1	500	500	500
Acceleration (rpm/s), cycle 1	100	100	100
Time (s), cycle 1	10	10	10
Spin speed (rpm), cycle 2	3000	3000	3000
Acceleration (rpm/s), cycle 2	500	500	500
Time (s), cycle 2	30	30	30
Soft bake (min; °C)	1; 85	5; 85	10; 85
Exposure dose (mJ/cm^2)	150	160	220
PDMS carrier stamp dimensions (length×width×height mm)	∼30×30×10	∼30×30×10	∼30×30×10
Steel block weight (kg)	0.2-0.3	1.0-2.2	1.7-2.7
Lamination bake (min; °C)	4; 95	10; 95	25; 95
Hard bake (min; °C)	60; 175	60; 175	60; 175

Table 3.1: Process parameters for bonding SU-8 films onto KMPR structures.

3.3.3 Demonstration of SU-8 onto KMPR bonding

By performing the preparation of the PDMS carrier stamps and the bonding procedure as outlined in Section 3.3.1 and Section 3.3.2, respectively, SU-8 films down to 0.5 μm can be laminated onto KMPR structures.

In the following Subsections, the results of employing the three different PDMS carrier stamp configurations are described.

3.3.3.1 Bonding using unstructured PDMS carrier stamps

For the initial experiments, the flat and unstructured PDMS carrier stamps from Section 3.3.1.1 have been used to bond 0.5 μm thick SU-8 layers onto KMPR microchannel structures. After the first successful lamination tests, the maximum area that can be covered with a 0.5 μm thick SU-8 film has been evaluated.

During the temperature-assisted process, carried out as described in Section 3.3.2, the weight is increased slowly on top of the PDMS carrier stamp until full contact between the KMPR test areas and the SU-8 film can be observed as shown in Fig. 3.7 (a). Fig. 3.7 (b) shows a test sample with differently sized squares between 10 μm and 2 mm after the cross-linking of the SU-8 film.

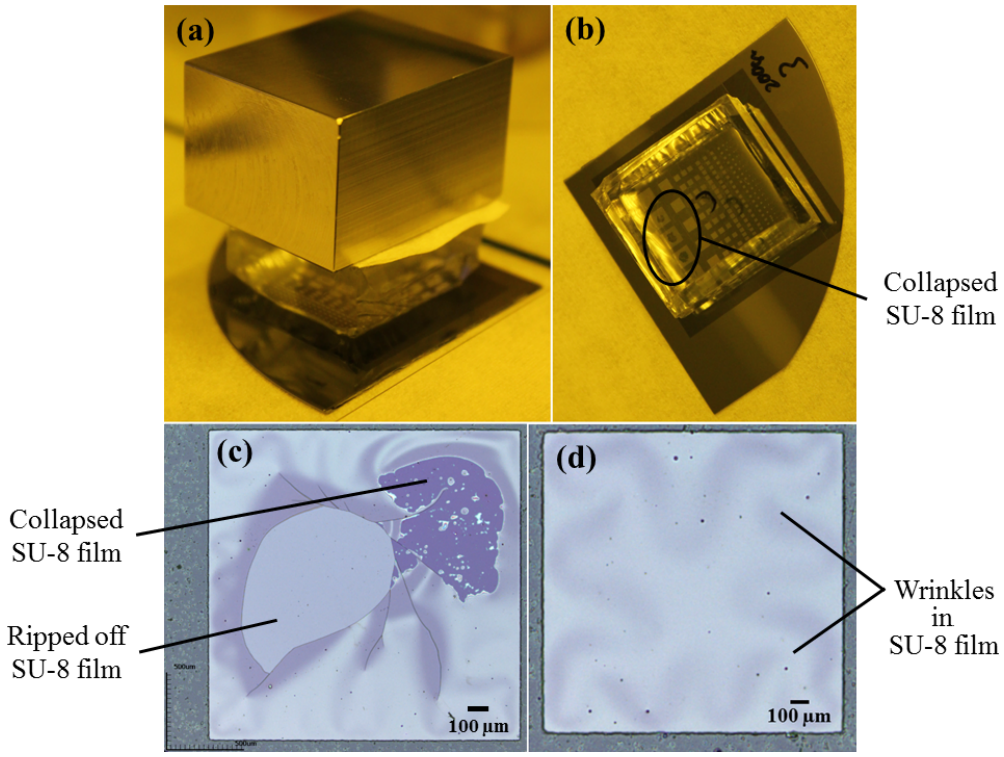

Figure 3.7: SU-8 onto KMPR structures lamination using a PDMS carrier stamp. (a) SU-8 cross-linking process at room temperature with applied weight and (b) test sample before peeling off the PDMS carrier stamp. (c) Possible fabrication errors and (d) fully covered and laminated SU-8 film on KMPR.

As can bee seen from the dark spots in the largest squares of 2 × 2 mm at the bottom left of the sample (black circle), that the PDMS carrier stamp sags into the KMPR structures due to the weight on top, which will result in a collapsed SU-8 film. However, a minimal weight is always required to ensure good contact between the SU-8 film and the KMPR structures.

Fig. 3.7 (c) summarizes errors that can occur during the bonding process. If the area to be covered is too large, the PDMS can sag into the structure, leading to a collapsed film as shown in the top right corner of the image. More likely, the SU-8 film still sticks to the PDMS carrier stamp and tears away parts or the complete SU-8 film over the KMPR structure when the PDMS carrier stamp is peeled off. This effect can be seen in the left part of Fig. 3.7 (c). Fig. 3.7 (d) shows the largest area of 1 × 1 mm that has been successfully covered with a flat, unstructured 0.5 μm thick SU-8 film during the evaluation of the maximum lamination area. However, as can be seen that the laminated layer exhibits wrinkles.

The obvious first reason for the wrinkles in the SU-8 film is the fact that air inside the covered KMPR structures is trapped and expands during the temperature-assisted cross-linking process. Thus, in the following experiments, the bonding temperature was gradually reduced while increasing the time to let the SU-8 cross-link. The best results for 0.5 μm thick SU-8 layers have been achieved by cross-linking the SU-8 at room temperature for 48 h. Such films appear to be planar all over the KMPR structures (Fig. 3.8 (a, b)).

A second hypothesis to avoid wrinkles in the SU-8 film is, to cross-link SU-8 over open KMPR structures in order to prevent the thermal expansion of trapped air. Experiments with open KMPR structures have shown that even with the temperature-assisted cross-linking process, planar laminated SU-8 films can be achieved.

In summary, the problem with wrinkles in the laminated SU-8 film can be solved by laminating onto open structures or by curing the SU-8 film at room temperature. However, this effect only occurs with thin films up to a few micrometres of thickness. Thicker films are less sensitive and do not show any wrinkles even for the temperature-assisted process over enclosed structures (Fig. 3.8 (c)).

A major problem that was accidentally found during a clean room breakdown is that the lamination of thin SU-8 films is very sensitive to elevated relative humidity (RH) values. Temperature-assisted and room temperature lamination tests have been carried out as described above in this Section. The results have shown that at humidity values higher than 55 % RH it is very likely that the 0.5 μm thick SU-8 film to be bonded onto the KMPR structures remains sticking on the PDMS stamp even after fully curing. Similar tests with thicker SU-8 films in the range between 2 μm to 5 μm have shown that such thicknesses are less sensitive to the environmental humidity and can be successfully bonded even at higher RH values. The more robust lamination of thicker SU-8 films may be attributed to their mechanical integrity or may be due to the greater concentration of active epoxy groups that exist deeper within the core of the film that have not been passivated by exposure to humidity and thus may diffuse to the interface with the KMPR to achieve cross-linking. Further investigation would be required in order to draw a conclusion as to the reason for this observation.

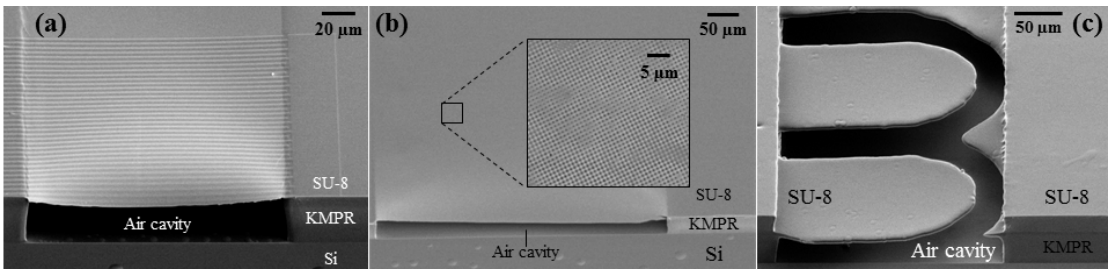

Figure 3.8: Angled scanning electron microscope (SEM) micrographs of various laminated SU-8 films after cleaving the sample containing (a) gratings, (b) nanowells and (c) free-standing structures.

In conclusion, it is highly recommended to control the clean room conditions at around 21 °C temperature and a humidity of lower than 40 % RH in order to successfully laminate SU-8 films below 1 μm of thickness.

3.3.3.2 Bonding using structured PDMS carrier stamps

After the initial experiments of bonding flat and unstructured SU-8 films, structured PDMS carrier stamps are employed to realise structured laminated SU-8 layers. By exploiting the insights gained in Section 3.3.3.1, a large variety of structured laminated SU-8 layers can be realised. Fig. 3.8 (a, b) shows angled scanning electron microscope (SEM) images of examples of laminated SU-8 layers after cleaving, approximately 0.5 μm thick, that can be achieved by using the structured PDMS carrier stamp from Section 3.3.1.2. In Fig. 3.8 (a) the microchannel is about 250 μm wide and 25 μm high. The edge of the layer appears brighter and to be bent, this is likely a result of the manual cleaving process of the sample. However, the main part of the layer appears planar all over the microchannel structure. By demonstrating the lamination of structured SU-8 films down to a thickness of 0.5 μm, air-suspended photonic applications in the infrared wavelength regime as well as optofluidic applications when the microchannel is exploited as fluidic channel can be enabled. Fig. 3.8 (b) shows an angled SEM image of the widest covered KMPR microchannel being about 500 μm wide and 25 μm high. Here, the complete laminated film is structured with nanowells with a diameter of several hundred nanometres proving that even highly structured layers with a high surface energy can be transferred.

3.3.3.3 Bonding using PDMS carrier stamps with an embedded photo mask

The results of the lamination of SU-8 layers using PDMS carrier stamps with embedded photo mask prepared as outlined in Section 3.3.1.3 are described in this paragraph. The lamination using this PDMS carrier stamp configuration is carried out in the same way than outlined in Section 3.3.2. However, after the lamination of the SU-8 layer, the unexposed parts of the laminated layer can be developed, resulting for instance in free-standing elements as shown in Fig. 3.8 (c).

If required, a second layer of photoresist such as KMPR or SU-8 can be processed on top before the development procedure. Then the unexposed parts of the laminated layer are developed together with for example a second microchannel as shown in Fig. 3.8 (c). Here, the film thickness is about 5 μm with a microchannel being about 250 μm wide and 25 μm high. The second microchannel can then be covered again with an SU-8 layer enabling three-dimensional structures such as microfluidic channel networks. More details about this lamination scheme are provided in the next Section, Section 3.4.

In summary, with the demonstrated SU-8 onto KMPR microchannel lamination method, microfluidic, optic and optofluidic applications can be enabled. While optic and optofluidic applications are further investigated in the context of this work, a simple microfluidic application in terms of a passive microfluidic mixer is demonstrated in the following Section.

3.4 Application example – microfluidic mixer

As demonstrated in Section 3.3.3, free-standing and three-dimensional polymer structures can be achieved using the SU-8 bonding method proposed in Section 3.3.2. By exploiting this fabrication process, a three-dimensional microfluidic channel network is fabricated by employing a PDMS carrier stamp with an embedded photo mask made of PET foil as described in Section 3.3.1.3. This three-dimensional microfluidic channel network can be exploited for example as a simple passive microfluidic mixer as demonstrated in the following.

3.4.1 Introduction

Mixing fluids is a fundamental procedure in numerous microfluidic applications including drug delivery, biochemistry analysis, biological processes or lab-on-a-chip platforms for complex chemical reactions [123, 124]. Furthermore, the investigation of micromixers is fundamental for understanding transport phenomena on the microscale [123]. Mixers can be integrated into a microfluidic system or work as stand-alone devices. Generally, mixers are classified into passive or active mixers. Passive mixers are the most simplest and mainly rely on molecular diffusion and chaotic advection as fluids flow laminar on the microscale [123]. Active mixing can be achieved by alternating the flow velocity [125], or by acoustic or thermal disturbance, electrokinetic instability, piezoelectric membranes or microimpellers [126].

In the following a simple passive microfluidic mixer is shown as application of the SU-8 bonding method proposed in Section 3.3.2.

3.4.2 Experimental demonstration

First, microchannels of KMPR are fabricated by photolithography using the protocol given in Section 3.3.1.4. The PDMS carrier stamp is then plasma treated and a 5 μm thick SU-8 film is subsequently spin coated on top. After the soft bake the sample is exposed through the PDMS carrier stamp by UV radiation and then aligned to the microchannels using the self-made alignment tool. Steel blocks are then applied on top of the PDMS carrier stamp until full contact between the microchannels and the SU-8 film is observed. For a 5 μm thick uncured SU-8 layer and carrier stamp dimensions of approximately 30 $\times$ 30 $\times$ 10 mm (length $\times$ width $\times$ height) used in the experiments, the required weight of steel blocks has been between 1.7-2.7 kg. This ensures good contact between the SU-8 film and the KMPR microchannels.

A post-exposure bake to cure the layer to be bonded is then carried out. The sample on the hotplate is heated up to 95 °C. At 95 °C the temperature is held for 25 min in order to cross-link and thus bond the SU-8 layer on top of the KMPR structures. After cooling down the sample to room temperature, the PDMS carrier stamp is carefully peeled off and the SU-8 layer remains bonded on the KMPR microchannels. At this stage of the fabrication process, the unexposed areas of the SU-8 film have not yet been developed. In order to achieve a three-

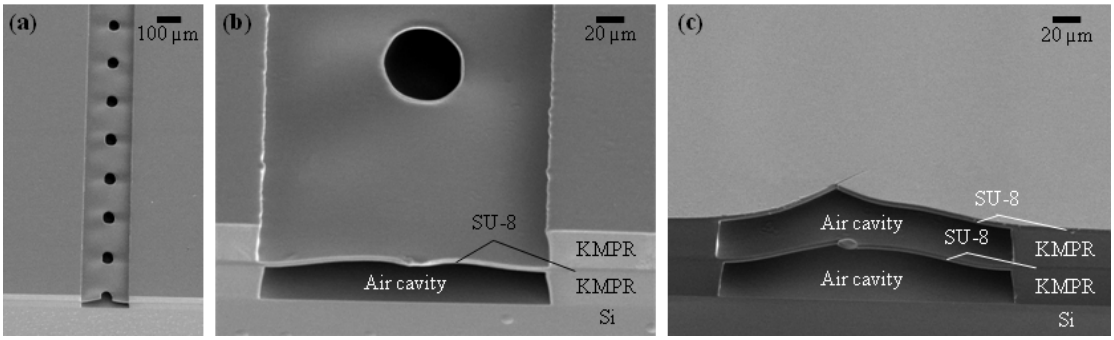

Figure 3.9: (a) Angled scanning electron microscope (SEM) micrographs of two microfluidic channels connected by openings in the laminated SU-8 layer after cleaving the sample, (b) close-up of (a), and (c) finally sealed three-dimensional microfluidic channel network fabricated by combining photolithography and lamination processes.

dimensional microfluidic mixer network a second layer of 25 μm thick KMPR 1025 is spin coated and soft baked on top of the laminated slab of SU-8 with the same parameters used for the fabrication of the microchannels. The photo mask containing the microchannel pattern is then aligned to the existing microchannels and the unexposed areas of the laminated SU-8 layer using a mask aligner, and the sample is exposed by UV radiation with an intensity of 650 mJ cm^{-2}. The subsequent post-exposure bake is extended by 1 min to 4 min in total due to the layers underneath. During the development of the second microchannel structures, the unexposed areas of the laminated SU-8 layer which have been defined by the embedded photo mask of the PDMS carrier stamp (Fig. 3.5 (c)) are also developed and result in openings (holes) to connect the two microchannels. For this reason, the sample is developed until the lower channels are filled with developer. This filling of the lower channel is observed after 4 min of developing.

Fig. 3.9 (a) and (b) show the cross-section of an angled scanning electron microscope (SEM) image of the structure after cleaving the sample. Two aligned microfluidic channels of about 250 μm width and 25 μm height and an approximately 5 μm thick SU-8 layer with openings to connect the two channels can be seen. Lastly, the structure is sealed with a 5 μm thick SU-8 layer using a flat PDMS carrier stamp. Fig. 3.9 (c) shows a SEM image of the cross-section of the final three-dimensional microfluidic mixer after cleaving the sample. Here, it is important to mention that the cracks in the transferred SU-8 films result from manual cleaving of the sample. As shown in Fig. 3.10 (a) the top and the

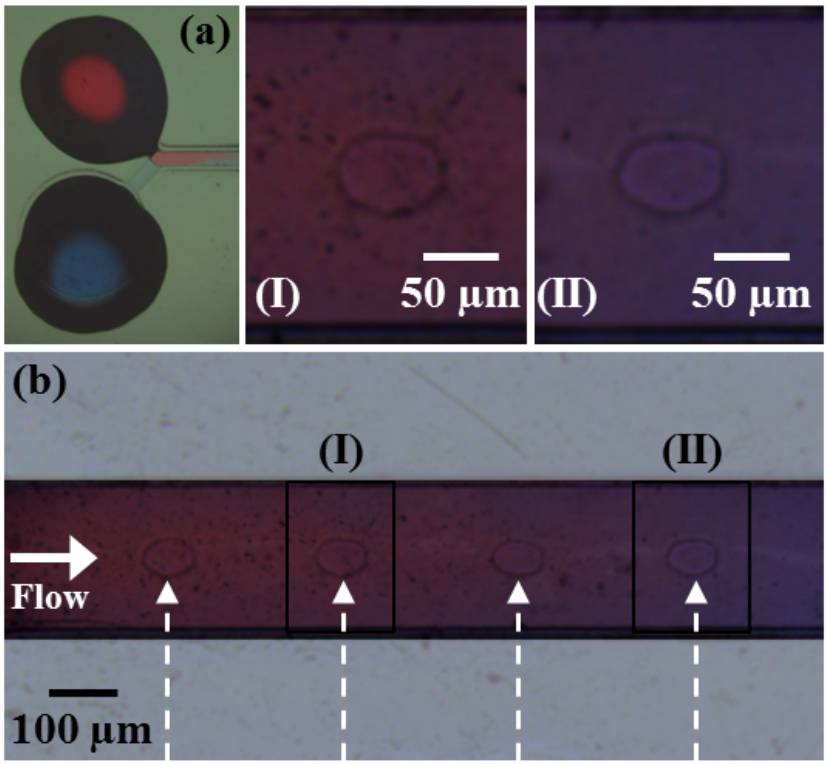

Figure 3.10: (a) Top view of the inlet reservoirs providing the coloured liquids separately for the upper and lower microchannel, and (b) demonstration of the passive microfluidic mixing. The white dashed arrows point to the positions of the opening. The black numbered rectangles (I) and (II) show magnified views along the mixing area.

bottom channels are connected to separate inlet reservoirs, which can carry the liquids towards the mixing area, where both channels are connected by the openings. Here, the structures are fabricated on a borosilicate glass substrate to obtain a fully transparent sample that be probed under an inverted optical microscope (GX51, Olympus GmbH) in transmission mode trough all layers of the sample. The fabrication process on borosilicate glass is similar to the 5 μm process given in Tab. 3.1, except that the glass substrates have been treated with a dehydration bake in a vacuum oven at 200 °C for 12 h and an additional plasma treatment for 5 min using ambient air before spin coating. In the experiments, DI water coloured with red and blue food dye is further dissolved with a tiny amount of isopropanol to ensure good flow behaviour in the microchannel structures. First, the blue liquid is applied by a pipette into the inlet reservoir of the lower channel and subsequently the red liquid into the reservoir of the upper channel. The lower

channel with the blue liquid is rapidly filled due to capillary forces. When the red liquid is applied into the upper channel and reaches the mixing area with the openings it is mixed vertically with the blue liquid of the lower channel. As shown in Fig. 3.10 (b) it takes about three to four openings to visually see a mixing effect of the two coloured liquids under the given conditions.

In summary, by employing a three-dimensional channel network as simple microfluidic mixer, it has been demonstrated in this Section that the SU-8 bonding method is suitable for microfluidic applications. The experiment has shown that this simple approach is a practical technique to realise a planar polymer-based microfluidic mixer. In future work, different mixing structures based on the SU-8 bonding method could be tested for different liquids in combination with microfluidic pumps and connectors instead of the employed capillary force mechanism.

Furthermore, for future micro- and optofluidic applications, it is important to evaluate the capacity of such structures to withstand pressure which is investigated in the following Section 3.5.

3.5 Bond strength evaluation

The bonding of three different SU-8 film thicknesses (0.5 μm, 2 μm and 5 μm) onto KMPR structures has been reported in Section 3.3.2. To evaluate whether such thin films are suited for micro- and optofluidic applications or not, the bond strength needs to be evaluated.

Tensile strength tests were carried out to compare the bond strength of the different laminated SU-8 films. Similar to a previously reported method [127], KMPR microchannels of 250 μm width and 2 cm length with a dead end connected to a reservoir as inlet were lithographically defined and sealed with different film thicknesses of 0.5, 2 and 5 μm by employing the described bonding method (Section 3.3.2). Fig. 3.11 (a) shows the initial microchannel test structure. A pressure supply (FemtoJet 4i, Eppendorf AG) was used to apply air pressure into the microchannels in order to evaluate the pressure that the laminated SU-8 films could withstand before rupturing.

After initial testing, the applied air pressure for film thicknesses of 2 μm and 5 μm was successively increased in increments of 500 hPa every 30 s. For a film thickness of 0.5 μm the increments were 100 hPa every 30 s. During the

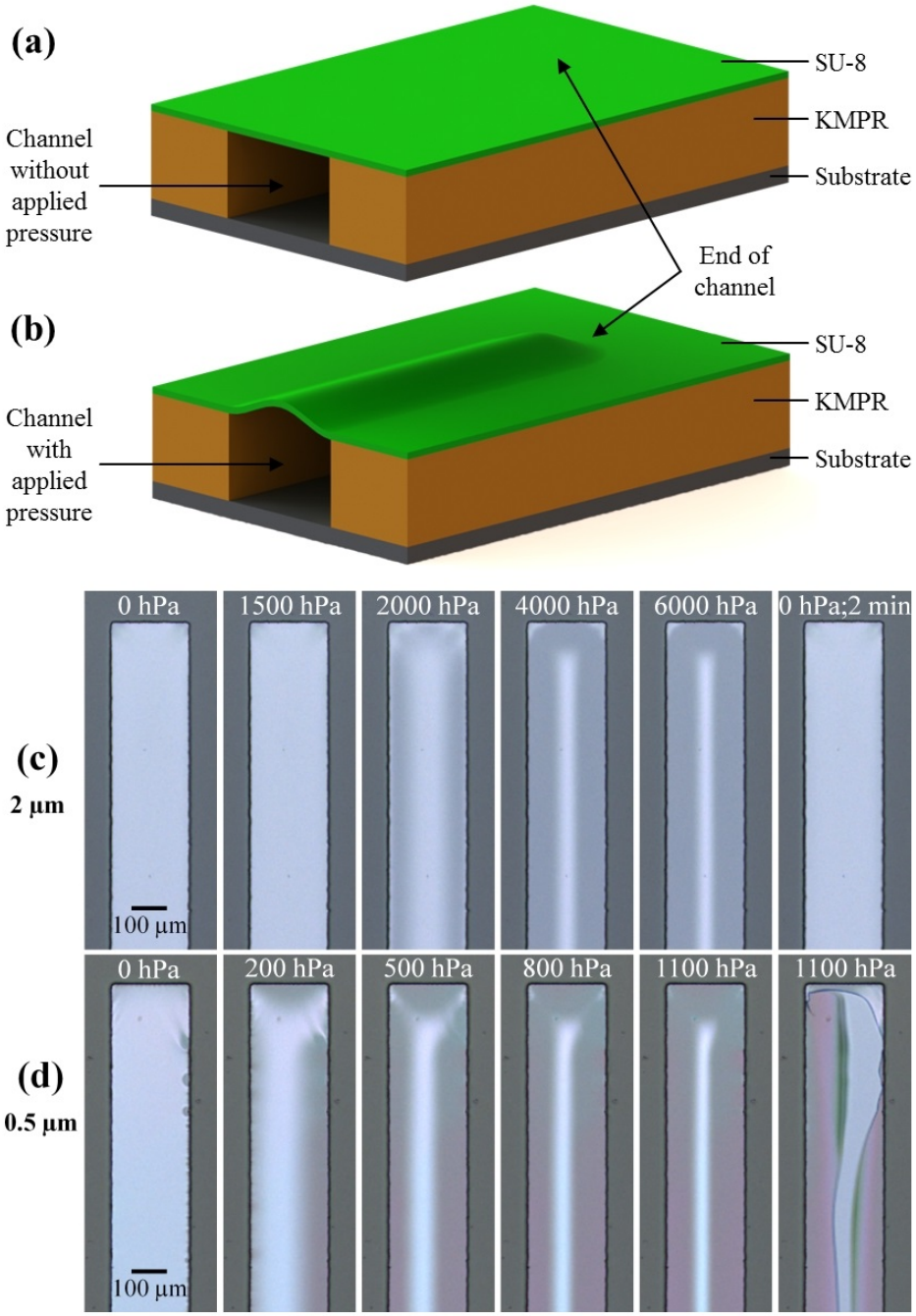

Figure 3.11: Schematic overview of the test structure (a) before and (b) during the bond strength evaluation with applied pressure (not to scale); and top views of optical microscope images of the experiment with SU-8 film thicknesses of (c) 2 μm and (d) 0.5 μm at various pressures. 2 μm thick films withstand the maximum capacity of the pressure supply of 6000 hPa and relax back into their initial state after approximately 2 min after the applied pressure is switched off, while 0.5 μm thick films burst at a pressure of around 1100 hPa.

experiments as represented in Fig. 3.11 (b), the air pressure was increased until the maximum pressure of the pump was reached or alternatively the pressure dropped rapidly due to the bursting of the SU-8 layers. For easier verification, the complete experiment was visually observed from the top using an optical microscope (LEXT OLS4000, Olympus GmbH). The experiments showed that the laminated SU-8 films with thicknesses of 5 μm and 2 μm can withstand at least 6000 hPa which is the maximum capacity of the used pressure pump. Films with thicknesses of 0.5 μm withstood pressures of 1100 hPa before the layers burst in the area of the microchannel structure. Delamination of laminated areas without the microchannels was not noticed.

From Fig. 3.11 (c) and (d) it can be seen that with increasing pressure, the SU-8 films over the channel structures get more and more bulged. The expansion of the layer at different applied pressures depends on the film thickness as the images indicate. For the 2 μm thick layer in Fig. 3.11 (c) no expansion can be seen up to a pressure of 1500 hPa. Then, with increasing pressure the film over the channel significantly expands. If the pressure is abruptly removed from the channel, the SU-8 layer relaxes back into its initial state after approximately 2 min and no visible deformation can be seen, as shown in the last image of Fig. 3.11 (c). When pressure is applied to a 0.5 μm thick film an expansion of the layer can be seen even at low pressures of around 100-200 hPa (Fig. 3.11 (d)). Similar to the 2 μm layer the expansion gets larger with increasing pressure. A few seconds after applying a pressure of 1100 hPa the SU-8 layer bursts in the area of the channel structure.

In summary, it is assumed from the experiments, that thinner SU-8 layers have a larger expansion at the same applied pressures and a lower capacity to withstand pressure compared with thicker films. After deformation, if the pressure is returned to ambient, the laminated SU-8 layers relax back into their initial state after approximately 1-6 min depending on the thickness of the layer and the applied pressure. For laminated SU-8 films below 5 μm no bond strengths had been reported in the literature, however, the value of 6000 hPa withstand pressure for 2 μm and 5 μm is in good agreement with published results ranging from 5100 hPa for 5 μm to 80 μm film thicknesses of SU-8 [19] up to 10000 hPa for 10 μm to 120 μm film thicknesses [128]. It can be concluded that the laminated SU-8 films are surprisingly robust and certainly should be suitable for most microfluidic and optofluidic applications.

3.6 Conclusions

This Chapter has introduced a method to bond unstructured and structured SU-8 films down to sub-micron thicknesses onto microchannels fabricated in KMPR using a flexible PDMS carrier stamp. By exploiting differently cast PDMS carrier stamps, flat and structured layers can be transferred over areas of up to 1×1 mm. In the experiments, the bonding of highly structured SU-8 films, approximately 0.5 μm thick, onto KMPR microchannels has been demonstrated. Despite a thorough search of the literature, it would seem that this is the first experimental realization of the bonding of structured and unstructured SU-8 films below 1 μm of thickness.

The effect enabling the lamination of such thin layers can be explained by the chemical properties of the used materials. The processed KMPR structures are not fully cured and thus can still carry residual epoxy-groups that are reactive and can diffuse into the uncross-linked epoxy-groups of the SU-8 layer to be bonded. When the SU-8 is fully cured, it forms a dense network that is from a chemical point of view unable to react or bond to PDMS as the siloxane groups of PDMS cannot react with the epoxy groups of SU-8. Consequently, the only limiting factor is the remaining adhesion between the PDMS carrier stamp and the cured SU-8 layer.

In order to successfully laminate SU-8 films below 1 μm of thickness it is highly recommended to control the clean room conditions at around 21 °C temperature and a humidity of lower than 40 % RH. Especially at higher humidities it was found that the SU-8 film to be bonded on KMPR structures very likely remains sticking on the PDMS carrier stamp even after fully curing. SU-8 films of approximately 2-5 μm and thicker are less sensitive to the environmental humidity. Furthermore, to avoid wrinkles in laminated layers below 1 μm of thickness, the bonding process should be carried out over open KMPR structures when the cross-linking of the SU-8 is temperature assisted or more preferable, cross-linking should be carried out at room temperature conditions. With increasing SU-8 thickness, the film gets less sensitive and does not show any wrinkles even for the temperature assisted process over enclosed structures.

In addition, bond strength tests have demonstrated that such thin layers can withstand pressures up to 1100 hPa and are suitable for most micro- and optofluidic applications where only a minimal pressure is required.

In contrast to the SU-8-onto-SU-8 bonding methods only employed for sealing of microchannels as described in Section 3.1, the presented SU-8-onto-KMPR bonding technique enables (I) patterned films to fabricate for example optical structures, (II) thin films down to 0.5 μm thickness, which can in principle be used to guide light in the single-mode regime for infrared light, and (III) a refractive index contrast possibly needed for optical applications by employing SU-8 and KMPR.

More complex PDMS carrier stamps and thus more complex laminated structures could be achieved by combining the different PDMS carrier stamp configurations. Furthermore, many processes can be carried out on top of the laminated layer such as photolithography, additional bonding steps, or electron beam lithography making the bonding technique a very versatile process for rapid prototyping in polymers.

Most importantly, the combination of possible fluid handling in the microchannels and photonic structures realized in the laminated SU-8 layer enables research towards a large range of applications in microfluidics, optics and optofluidics. It has been demonstrated that the SU-8 bonding method is suitable for microfluidic applications by applying a three-dimensional channel network as simple microfluidic mixer. However, in order to exploit thin, structured SU-8 films for optical and optofluidic sensing applications as it has been proposed, it is necessary to investigate whether the air-suspended SU-8 films can, in fact, guide light vertically; and whether the surface structures can be used to form waveguides guiding the light laterally.

4 Air-suspended single-mode SU-8 rib waveguides

In Chapter 3 a method has been introduced to laminate structured SU-8 films down to sub-micron thicknesses onto KMPR microchannels using a PDMS carrier stamp. However, in order to exploit this approach for optical and optofluidic sensing applications as it has been proposed, suitable methods need to be developed to use these films as waveguides and as microfluidic channels. This includes creating structures that can capture and guide light in the thin SU-8 film and also methods to launch light into it.

In this Chapter, large cross-section optical single-mode rib waveguides are designed, realised and demonstrated within laminated, air-suspended SU-8 films described in Chapter 3. Rib waveguides are the simplest air-suspended optical waveguides that can be realised.

First, the basics on optical waveguides and an overview of different integrated optics waveguide geometries are given. Then the design and simulation as well as the experimental realization and demonstration of optical waveguiding of air-suspended single-mode optical SU-8 rib waveguides are presented. In order to couple light into the waveguides, butt coupling is employed.

The main part of Chapter 4 is adapted from the published conference proceeding *"Air-suspended polymer rib waveguides"* [129].

4.1 Introduction

In the progress of downscaling integrated photonic structures and hence optofluidic devices, it is important to provide a refractive index contrast between the waveguiding core and the surrounding claddings. A high refractive index contrast forces the light to be strongly confined in the waveguide and therefore facilitates the capability of reducing device proportions [130, 131]. Strongly confined light enables robust waveguide devices with ultra-low propagation loss [132, 133] and high-density integrated optical circuits [134], and hence reduces the cost of integrated photonic circuits.

However, in contrast to semiconductors, conventional polymers including SU-8 or KMPR do not offer a large contrast in refractive index which is typically ranging from n = 1.30-1.70 [135].

Several groups have proposed methods to increase the refractive index contrast for polymer optical applications, whereas the majority employed a layer of high refractive index coating of SiN(Si_3N_4) [136, 137]. However, to fabricate such structures, PECVD (plasma-enhanced chemical vapor deposition) and selective reactive ion etching etch is required. Besides the toxic by-products and the high costs of the equipment, it has to be considered that the PECVD process has to be optimized for the employed polymer due to the high temperatures ($\approx$ 200 °C) required for the film deposition.

Another strategy, instead of adding a high-index layer, would be to introduce porosity to the underlying cladding layer which reduces the cladding index and thus increase the refractive index contrast [138–140]. By employing electrochemical etching in hydrofluoric acid of silicon wafers or oxidation, porous silicon can be fabricated with an refractive index down to $n = 1.13$. However, porous silicon is an unstable material and its properties change in storage and operation [141].

Another option for low refractive index claddings is mesostructured silica which can be obtained by acidic sol-gel block copolymer templating chemistry. Such material is mechanically and hydrothermally stable and has a refractive index down to $n = 1.15$ [139].

Similar refractive indices (n = 1.147-1.278), depending on the porosity, can be achieves by thin nanoporous dielectric films obtained by a process where an organic macromolecular (porogen) phase is selectively removed from a phase-separated organic/inorganic polymer hybrid [140].

However, the maximum refractive index contrast for photonic devices can be achieved by exploiting air ($n = 1.0$) as cladding material. This is a common method and has been demonstrated in different materials including air-bridge micro cavities in GaAs [6], 2D photonic crystals air-bridge structures in AlGaAs [7], free-standing grating couplers in GaN [8], photonic crystal slab waveguides in SOI [9], air-bridge-type waveguides in Si [142], suspended slab and photonic crystal waveguides in lithium niobate [132] or air-suspended photonic crystal slab waveguides in polymer [143].

Most of the mentioned devices have been fabricated in high refractive index silicon-on-insulator (SOI) materials using sacrificial layers including several selective etching steps. Simple coupling of light using optical fibres and waveguiding in air-suspended SU-8 polymer structures has been demonstrated by using such etching

methods [144]; however, the employed waveguides are about 3.5 mm long and 100 μm wide with a thickness between 35 μm and 50 μm which is within the multi-mode regime. For the intended polymer optofluidic sensors of this work the film thickness needs to be reduced to several hundreds of nanometres according to the single-mode condition as described in Chapter 3, Section 3.1.

Nowadays, microscale integrated applications exploiting polymer materials are extremely attractive for low-cost and mass-producible devices due to rapid and flexible processing. Unlike semiconductors, polymers allow simplified low temperature processing and can be molded into almost any conceivable shape. However, as already mentioned, conventional polymers do not offer large variations in their refractive indices when compared to semiconductors limiting the efficiency of polymer optical devices. The only way to achieve maximum refractive index contrast, not only in polymer photonic structures, is to exploit air as cladding material. A comparable fabrication method for air claddings in polymers can be derived from embedded microfluidic channels, where a polymer layer is used to seal the channel. For the widely used photoresist SU-8 numerous major methods have been reported: (I) SU-8 with filling material that can easily be dissolved [145], (II) a metal mask to protect SU-8 from a second exposure [145], (III) using an embedded mask [146], (IV) proton beam to partially expose SU-8 [147], (V) UV dosage control and anti-reflection coating on SU-8 [148], (VI) SU-8 and PEC sacrificial material [149], (VII) SU-8 exposure with two different wavelengths [150], and (VIII) different SU-8 bonding methods utilizing a commercial lamination foil [10, 53], polyethylene terephthalate (PET) [11, 12], Pyrex [13, 14], Kapton [15, 16], polyimide [17], Borofloat glass [53] or PDMS [18, 19, 53]. With the bonding method for sub-micron structured SU-8 films onto KMPR microchannels using a PDMS carrier stamp presented in Chapter 3, such air-suspended polymer optical devices become now available.

In this Chapter, air-suspended SU-8 rib waveguides in the single-mode regime are presented after a brief introduction of planar optical waveguides. In general, single-mode waveguides offer numerous advantages. Single-mode waveguides guide only one mode with one certain group velocity resulting that a pulse of light travels without delay distortion. In comparison, in multi-mode waveguides, light travels at different group velocities and therefore the different modes undergo different time delays, so that each mode of a pulse of multi-mode light is delayed by different amounts and therefore the pulse spreads in time.

Furthermore, the rate of power attenuation is lower in a single-mode waveguide, compared to a multi-mode waveguide. This, together with the smaller pulse spreading rate allows higher transfer rates in single-mode waveguides [151].

Another negative effect in multi-mode waveguides is, that the modes randomly interfere. From uncontrollable imperfections, strains, and temperature fluctuations, each mode undergoes a random phase shift resulting in a random intensity of the sum of the complex amplitudes of the modes. This randomness is a form of noise known as modal noise or speckle. In comparison, single-mode waveguides have only one path and therefore no modal noise [151].

In terms of sensors, both single- and multi-mode planar waveguide sensors have been reported. A typical advantage of single-mode waveguide sensors is the excellent sensitivity and the high spatial uniformity evanescent fields. In comparison, multi-mode waveguides exhibit a less intense evanescent field as the intensity scales with the thickness of the waveguide. On the other hand, they are easier to fabricate and hence often less expensive [152].

4.2 Planar optical waveguides

In traditional optical systems, light is transmitted in the form of beams in free space and manipulated by optical components such as mirrors, lenses, and prisms. Such components are often bulky, large and unwieldy and objects in the beam path can obstruct or scatter. Therefore, it is advantageous to guide optical beams in dielectric materials rather than in free space. The first demonstration of waveguiding was presented by Jean-Daniel Colladon in 1842 [153]. In his water jet experiment, he demonstrated that light can be guided in water that is surrounded by air due to total internal reflection.

The basic principle of optical confinement is simple. A medium with a higher refractive index than the surrounding medium acts as a trap for the light and hence the optical rays remain confined by multiple internal reflections at the boundaries. The high-index optical medium is called the "core" while the surrounding low-index media is called the "cladding".

The simplest optical waveguide is a planar slab waveguide, which consists of a three-layer structure, where the waveguide layer is sandwiched between a substrate and a cover medium as shown in Fig. 4.1 (a). If the angle of the incident light

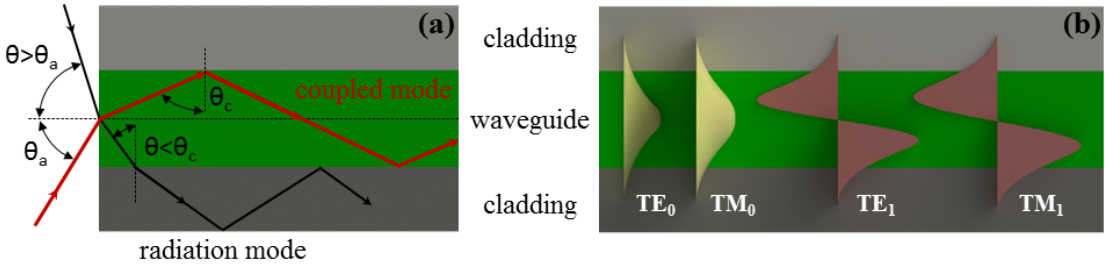

Figure 4.1: (a) Light propagation in a planar optical slab waveguide. Light can be coupled and guided when the refractive index of the core is higher than those of the surrounding cladding layers and when the angle of propagation is larger than the critical angle θ_c. Light entering the waveguide under an angle that is larger than the acceptance angle θ_a will lead to radiation modes. (b) Schematic visualization of the first four waveguide modes TE_0, TM_0, TE_1 and TM_1 of an optical waveguide. As indicated in the figure, the TM modes interrogate deeper into the surrounding cladding layers than the TE modes.

is within the acceptance angle θ_a, coupled modes can start propagating in the waveguide core. If the incident angle is larger, light cannot propagate which will result in radiation modes. Coupled modes can be guided in the waveguide core due to total internal reflection, when the refractive index of the core is higher than those of the surrounding cladding layers and when the angle of the propagating light is larger than the critical angles at the two cladding layers based on Snell's law (Eq. 4.1):

$$\theta_c = arcsin\left(\frac{n_{cladding}}{n_{core}}\right) \tag{4.1}$$

One of the most important characteristic of an optical waveguide is the attenuation or loss that can occur to the propagating light. Generally, propagation loss can be distinguished between three different mechanisms: scattering, absorption and radiation [154]. Scattering loss can be caused by imperfection in the waveguide or at the surface due to the material roughness. Absorption loss occurs when light (electromagnetic waves) is converted into some other energy form (for example heat) in the waveguide whereas radiation losses occur when the total internal reflection condition is compromised allowing light to leak out of the waveguide. Radiation loss can occur at waveguide bends or at abrupt transitions that do not meat the adiabaticity criteria.

The electric field distribution profiles of the first four possible modes of a waveguide (TE_0, TM_0, TE_1 and TM_1) are shown in Fig. 4.1 (b). When the electric field

of a mode is perpendicular to the direction of propagation in the optical waveguide, the mode is called a transverse electric (TE) mode. For the TE mode, the magnetic field can have a field component in the direction of propagation. When the magnetic field of a mode is perpendicular to the direction of propagation, the electric field can have a component along the direction of propagation and this mode is called a transverse magnetic (TM) mode. The number of guided modes of different orders depend on the thicknesses and the refractive indices of the core and the cladding materials. The number of guided modes decreases with decreasing thickness of the waveguide core or the refractive index contrast between core and cladding, or with longer wavelengths.

Several types of optical waveguides in numerous configurations in material and geometry are employed in integrated optics. In general, two types of waveguides regarding their geometrical design are classified: planar waveguides and nonplanar waveguides [155]. Planar waveguides are slab waveguides and have a planar geometry confining and guiding light in only one transverse direction as lateral modes become infinite as shown in Fig. 4.1 and Fig. 4.2 (a) [156]. In nonplanar waveguides such as channel waveguides or optical fibres, the core is surrounded by claddings in all transverse directions with a two-dimensional optical confinement. Most waveguides used in optical applications are nonplanar waveguides. The widely used channel waveguides can be further divided into ridge, rib, buried, strip-loaded and diffused waveguides. Ridge waveguides as shown in Fig. 4.2 (b) are fully free-standing high-index channel waveguides on top of a supporting low-index substrate. Rib waveguides (Fig. 4.2 (c)) are similar, but have only a partly free-standing structure on top of a slab with the same refractive index which is also part of the waveguiding core. A buried waveguide is embedded in the substrate and completely buried in a low-index surrounding material as shown in Fig. 4.2 (d). Strip-loaded waveguides (Fig. 4.2 (e)) are based on slab waveguides, but have a dielectric strip on top inducing a local effective refractive index change for the slab waveguide. Diffused waveguides (Fig. 4.2 (f)) are formed by creating a high-index region in a substrate through diffusion of dopants.

Furthermore, optical waveguides can be characterised into step-index, graded-index and photonic crystal waveguides depending on their refractive index profiles. Step-index waveguides exhibit an abrupt refractive index step at the substrate-waveguide and waveguide-cladding interface as shown in Fig. 4.2 (I). In contrast, graded-index waveguides exhibit a smooth refractive index transition between the

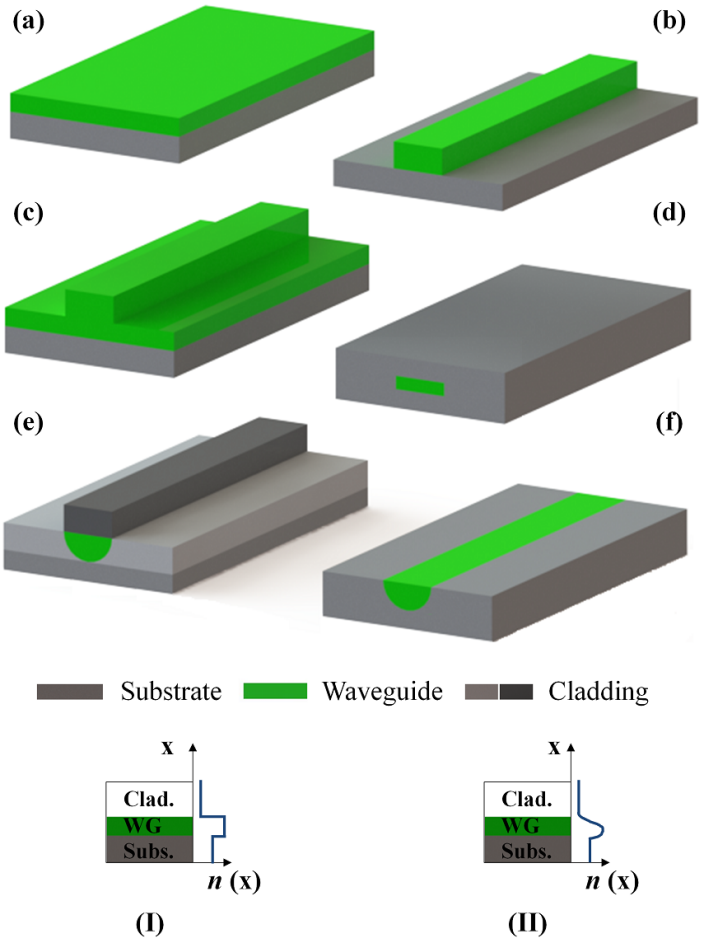

Figure 4.2: Schematic representation of different optical waveguide types. (a) slab, (b) ridge, (c) rib, (d) buried, (e) strip-loaded, and (f) diffused waveguide. Figure (I) and (II) represent step-index and graded-index waveguides. Step-index waveguides exhibit an abrupt refractive index step at the substrate-waveguide and waveguide-cladding interface while graded-index waveguides exhibit a smooth refractive index transition.

two interfaces (Fig. 4.2 (II)). Photonic crystal waveguides are composed of repetitive regions of low and high dielectric constants that affect the propagation of the electromagnetic waves by diffraction and interference effects [157].

In the following, air-suspended single-mode SU-8 rib waveguides are presented exploiting the SU-8 bonding method shown in Chapter 3. However, single-mode slab waveguides in SU-8 would be available by using this method, coupling of light into such a thin layer would be a very challenging task. In order to facilitate the light coupling process and the guiding characteristics, large cross-section rib waveguides are employed instead.

4.3 Air-suspended SU-8 rib waveguide design and simulation

Rib waveguides are the simplest air-suspended optical waveguides that can be realised and typically consist of a slab waveguide with a raised rib with identical refractive index on top. The rib is surrounded by low-index cladding material and acts as waveguide core providing strong optical confinement. Fig. 4.3 shows a cross-section of the rib waveguide studied in this Section. The rib width is W, the inner rib height is H and the slab height is h, where r is the fractional height of the slab compared to the inner rib, $r = h/H$. The wavelength of light used in the simulations is $\lambda = 1550$ nm with material refractive indices of $n_0 = 1.0$ (air), $n_1 = 1.575$ (SU-8) and $n_2 = 1.55$ (KMPR). The rib waveguide is a free standing structure on top of an air cavity with air as upper and lower cladding. The distance between the rib structure and the edge of the KMPR air cavity as well as the height of the KMPR layer are chosen in a way that the functionality of the rib waveguide is not affected.

In order to evaluate the characteristics of the light modes of an air-suspended polymer rib waveguide simulations are carried out. The objective of the simulations is to obtain a set of parameters for single-mode behaviour for TE modes that allow the fabrication of rib waveguide structures using standard clean room processes. Therefore, a large cross-section is preferable. For large cross-section single mode rib waveguides made of semiconductor materials, two simulation approaches have been used in the literature: the effective index method (EIM) according to Pogossian et al. [158] and the beam propagation method (BPM) according to Soref et al. [159].

In general, for rib waveguides with large cross-section the following condition has to be fulfilled:

$$H_{min} > \frac{\lambda}{\sqrt{n_1^2 - n_0^2}} \tag{4.2}$$

For an air-suspended rib waveguide with SU-8 as core material, the minimum height H_{min} at $\lambda = 1550$ nm has to be 1.27 μm. In addition to this, the dimensions of the rib waveguide have to fulfil the following condition to ensure single-mode conditions:

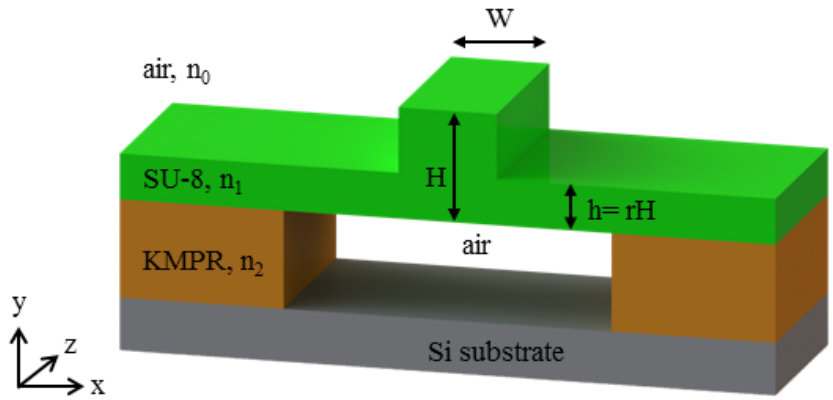

Figure 4.3: Schematic of the air-suspended polymer rib waveguide configuration.

$$\frac{W}{H} \leq C + \frac{r}{\sqrt{1-r^2}} \tag{4.3}$$

where W is the rib width, H the inner rib height, C a numerical correction factor and r the fractional height of the slab compared to the inner rib with $r \geq 0.5$. This condition is based on results from mode matching techniques by Petermann [160] and was derived by Soref et al. [159].

By using equation 4.2 and 4.3 and the correction factor of Soref et al. ($C = 0.3$) [159] and Pogossian et al. ($C = -0.05$) [158], respectively, plots of the theoretical curves of the single-mode limit can be obtained for the proposed air-suspended SU-8 rib waveguides as shown in Fig. 4.4. The areas on the right hand side of the plots correspond to single-mode waveguides while the left hand side correspond to multi-mode waveguides. By employing equation 4.2 and 4.3 as well as Fig. 4.4, a selection of dimensional parameters can be made in order to obtain an air-suspended rib waveguide with single-mode guidance of light.

In the following, the single-mode behaviour for air-suspended rib waveguides in SU-8 polymer is investigated by the EIM and afterwards by the BPM approach.

4.3.1 Effective index method (EIM)

The effective index method (EIM) is widely used and a simple technique to analyze and provide good predictions for the propagation characteristics of waveguides. The basic idea of the EIM is to approximate a waveguide by a one-dimensional one with an effective-index profile derivable from the geometry and the refractive-

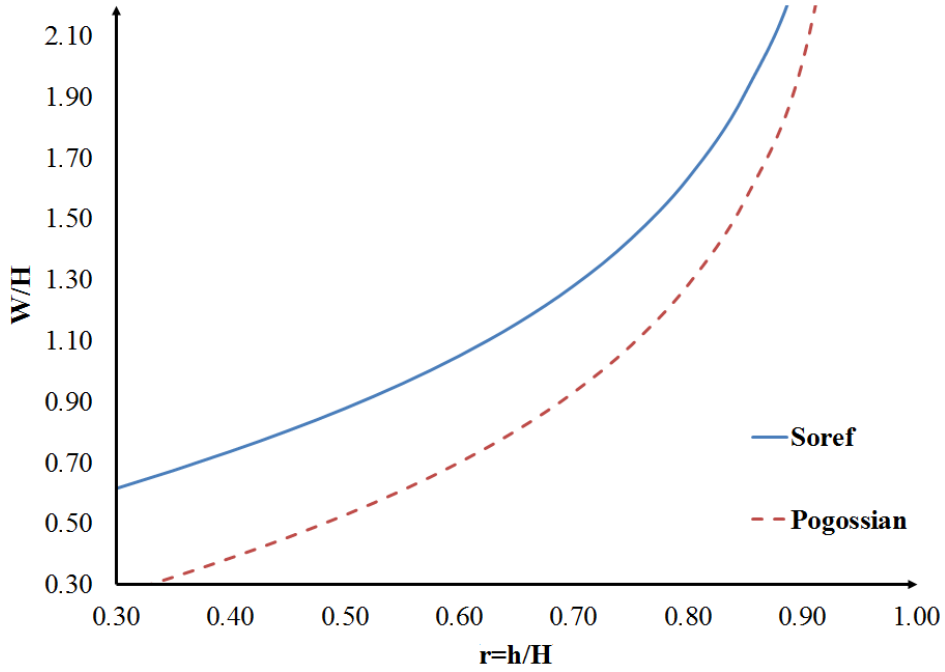

Figure 4.4: Plots of the theoretical single-mode limit by Soref et al. [159] and Pogossian et al. [158] for the proposed air-suspended SU-8 rib waveguides. The areas on the right hand side of the plots correspond to single-mode waveguides while the left hand side correspond to multi-mode waveguides.

index profile of the original structure [161–163]. The main feature and advantage of this method is the ability to convert a two-dimensional problem into a one-dimensional one [162]. By employing the obtained effective 2D planar waveguides of the EIM method, further design and simulations can be carried out, for example using the beam propagation method (BPM). This can save significant computation time [164].

When using the EIM method, the proposed rib waveguide is segmented into a slab and a rib region in the first case as shown in Fig. 4.5 (a) [165]. Then the effective refractive indices of the slab region (I) and the rib region (II) can be calculated using a mode solver for the vertical case (a). In the second case, the effective refractive index of the slab region (I) of the first case is used to calculated the effective refractive index of region (II) of the horizontal case (b).

By employing the EIM method, in order to have single-mode guiding laterally, the higher order modes vertically of the core must have propagation constants lower than the fundamental mode vertically in the cladding region [158]. If this condition is met, then all higher order modes are unbound in the rib region and

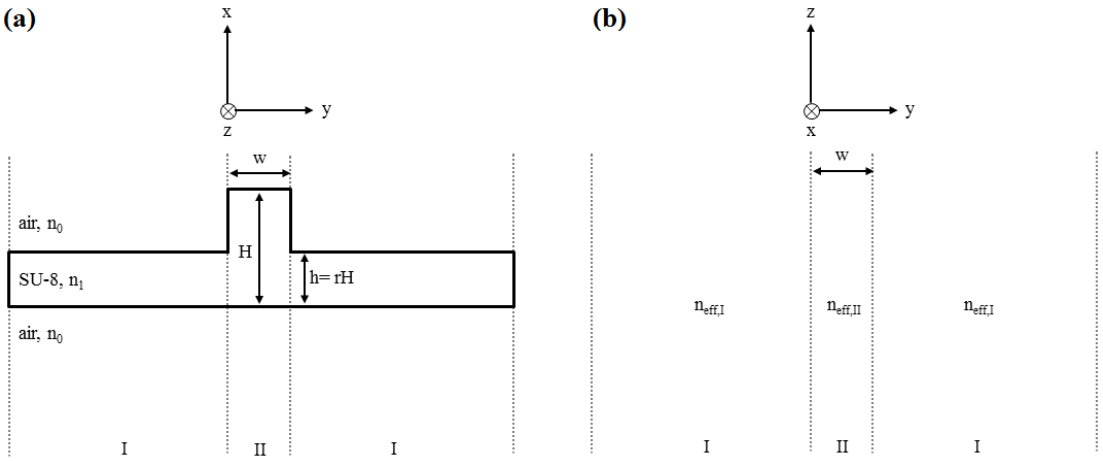

Figure 4.5: Schematic of the proposed rib waveguide resulting from the effective refractive index method. Vertical case (a) and horizontal case (b).

will couple into the slab region during propagation, where only the fundamental mode of the rib waveguide remains. When the rib waveguide is modelled correctly, only the TE_0 mode will be guided in the region of the rib. All higher order modes will be leaking into the slab regions of the rib waveguide and will therefore not propagate. This is known as quasi-single-mode behaviour.

Based on the theory of Section 4.3 on the single-mode condition of large cross-section semiconductor rib waveguides [159], a first assumption of the parameters of air-suspended polymer rib waveguide have been made by EIM calculations using CAMFR[1] (CAvity Modelling FRamework) [166].

By using the EIM method, the proposed rib waveguide is first segmented into a slab and a rib region and the effective refractive indices of the fundamental mode of the slab region (I) and the first higher order mode of the rib region (II) are calculated. In order to achieve a large cross-section rib waveguide, the height of the slab h is fixed in the simulations to 7 μm. Then the height H of the rib is swept and the corresponding effective refractive indices are calculated and plotted.

Fig. 4.6 shows the EIM result for the vertical case of the air-suspended rib waveguide. The black solid line represents the effective refractive index n_{eff} of the TE_0 mode of the slab region and the blue solid line the n_{eff} of the TE_1 mode of the rib region as a function of $r = h/H$ for a wavelength of $\lambda = 1550$ nm. It can be seen from the graph that at an h/H ratio of approximately 0.5, the rib waveguide

[1] CAMFR (CAvity Modelling FRamework) is a fast, flexible, friendly full-vectorial Maxwell solver. Its main focus is on applications in the field of nanophotonics [166].

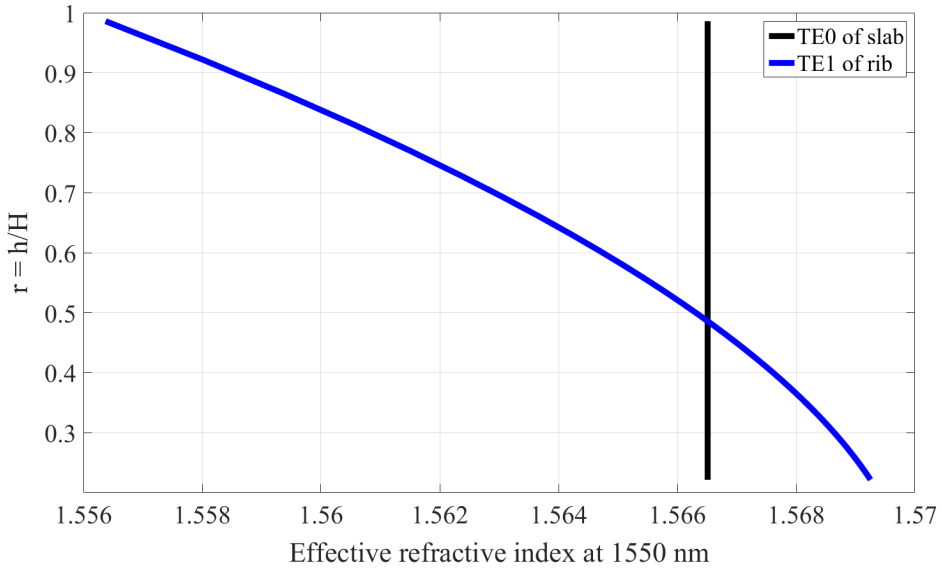

Figure 4.6: Effective index method results for the vertical case of a rib waveguide. It can be seen that at an h/H ratio of approximately 0.5, the rib waveguide configuration should only allow single-mode guidance as the n_{eff} of the TE_1 mode of the rib region is smaller as the TE_0 mode of the slab region.

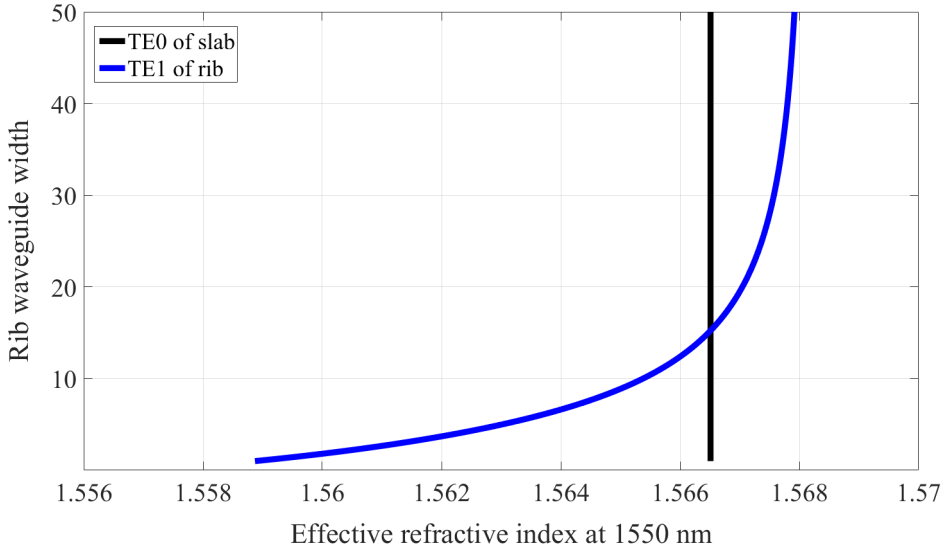

Figure 4.7: Effective index method results for the horizontal case of a rib waveguide. It can be seen that at a rib width larger than approximately 15 μm, the rib waveguide configuration is no longer in the single-mode regime as the n_{eff} of the TE_1 mode of the rib region is larger than the TE_0 mode of the slab region.

configuration should only allow single-mode guidance as the n_{eff} of the TE_1 mode of the rib region is smaller than the n_{eff} of the TE_0 mode of the slab region. This means that with the assumed slab height h of 7 μm, the height of the rib H has to be at least 14 μm or larger for single-mode guidance.

Fig. 4.7 shows the EIM result for the horizontal case of the air-suspended rib waveguide. The black solid line represents again the effective refractive index n_{eff} of the TE_0 mode of the slab region and the blue solid line the n_{eff} of the TE_1 mode of the rib region as a function of the width W of the rib waveguide for a wavelength of $\lambda = 1550$ nm. It can be seen from the graph that at a rib width larger than approximately 15 μm, the rib waveguide configuration is no longer in the single-mode regime as the n_{eff} of the TE_1 mode of the rib region is larger than the n_{eff} of the TE_0 mode of the slab region.

In summary, from the two cases of the EIM, an approximation of the propagation behaviour of waveguides can be made allowing the definition of a set of dimensional parameters that only allow quasi-single-mode guidance in the rib region.

However, in order to validate the expected single-mode behaviour and make an assumption of the modes of the proposed air-suspended SU-8 rib waveguide, a study of the light propagation in the rib waveguide needs to be carried out by using the beam propagation method.

4.3.2 Beam propagation method (BPM)

The beam propagation method (BPM) is one of the most commonly used numerical methods for the analysis and simulation of guided-wave propagation in inhomogeneous media. The basic idea of BPM is to represent the electromagnetic field by a superposition of plane waves propagating in homogeneous media [167]. Advantages of this method are that it is the most powerful technique to study the propagation of light in integrated optics and it is conceptually straightforward and allows rapid implementation of the photonic structure to be studied.

In the previous Subsection 4.3.1, an approximation of the propagation behaviour of the proposed air-suspended single-mode rib waveguide has been made by the effective refractive index profile using the EIM. In order to validate the expected single-mode behaviour, a study of the light propagation in the rib waveguide using the BPM is carried out by employing the BPM simulation software *RSoft* (Synopsys, Inc.).

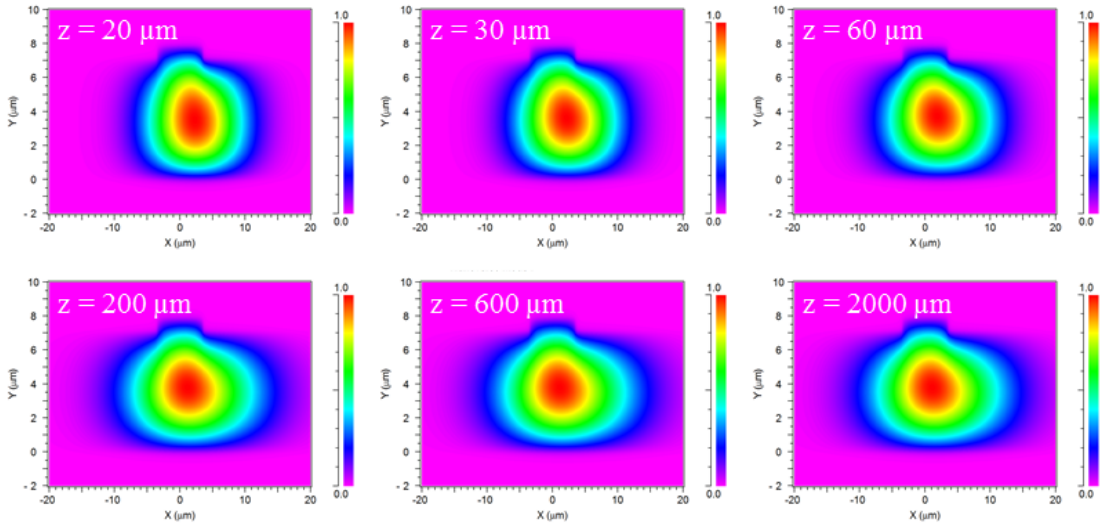

Figure 4.8: Propagation of the TE_0 mode of the rib waveguide with propagation distances (a) z = 20 μm, (b) z = 30 μm, (c) z = 60 μm, (d) z = 200 μm, (e) z = 600 μm and (f) z = 2000 μm, when a Gaussian field is launched off-axis into the rib. It can be seen that the mode profile becomes more symmetric the longer the light propagates and stays within the rib region.

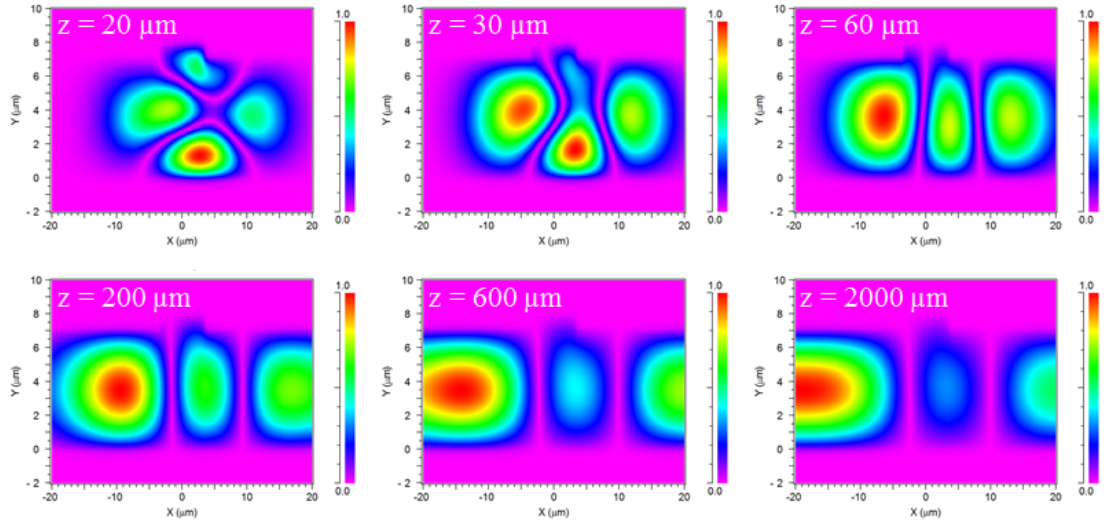

Figure 4.9: Propagation of the TE_1 mode of the rib waveguide with propagation distances (a) z = 20 μm, (b) z = 30 μm, (c) z = 60 μm, (d) z = 200 μm, (e) z = 600 μm and (f) z = 2000 μm, when a Gaussian field is launched off-axis into the rib. It can be seen that with increasing propagation length the higher order mode is radiated into the slab region and is no longer guided in the rib region.

According to the EIM results, higher order modes should not propagate in the slab region of an air-suspended rib waveguide with for example $W = 7$ μm and $r = 0.9$. Fig. 4.8 shows the evolution of a TE_0 mode for different z-values when a Gaussian field is launched off-axis into the rib for a waveguide with $W = 7$ μm and $r = 0.9$. These values have been chosen in order to have a large overlap with the fibre mode field (core diameter of 8.5 μm) in the experimental setup. It is evident from Fig. 4.8 that the mode profile becomes more symmetric the longer the light propagates and stays within the rib region, which was also experimentally shown in [159].

Fig. 4.9 shows the evolution of the TE_1 mode for different z-values when a Gaussian field is launched off-axis into the rib for a waveguide with the same dimensions as used to calculate Fig. 4.8. Here, with increasing propagation length the higher order mode is radiated into the slab region and is no longer guided in the rib region. From Fig. 4.8 and 4.9 it can be seen that for the given dimensions the rib waveguide only guides the TE_0 mode after a certain propagation distance, which is known as quasi-single-mode behaviour.

4.4 Waveguide realisation

The fabrication of the air-suspended polymer rib waveguides is carried out by transferring and bonding an SU-8 film onto a KMPR microchannel with a flat unstructured PDMS carrier stamp. First, a flat PDMS carrier stamp and the KMPR microchannels are fabricated as explained in Section 3.3.1. A 2 μm thick SU-8 layer is then spin coated onto the plasma treated PDMS carrier stamp. The sample is flood exposed by UV radiation and transferred onto the KMPR microchannels with the parameters listed in Tab. 3.1. After the uncured SU-8 layer is fully cross-linked and transferred onto the KMPR, the PDMS carrier stamp is carefully peeled off. In the next step, standard photolithography is employed to define the rib structure of the waveguide. A second 2 μm thick SU-8 layer is spin coated on top (Fig. 4.10 (a)) using the same parameters as given in Tab. 3.1. Subsequently, a soft bake of 1.5 min at 95 °C is carried out. The microchannels of the sample are then aligned to a photo mask containing the rib waveguide pattern using a mask aligner. After the exposure with UV radiation intensity of 100 mJ cm^{-2} as shown in Fig. 4.10 (b), the sample is post-exposure baked on a hotplate for 3 min at 95 °C, and developed for 2 min. Following this, the final

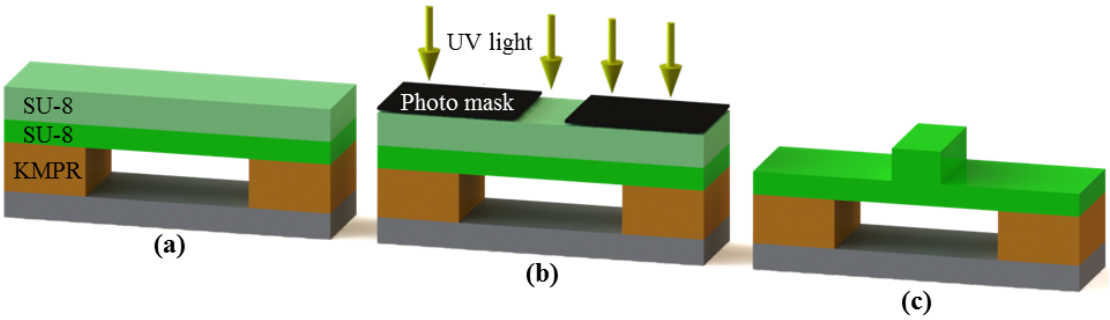

Figure 4.10: Fabrication process of air-suspended SU-8 rib-waveguides. (a) After bonding a flat SU-8 layer onto a KMPR microchannel, as described in Chapter 3, Section 3.3.2, a second SU-8 layer is spin coated on top. (b) Subsequently, a photo mask is aligned and the uncured SU-8 layer is exposed by UV radiation. (c) After developing the exposed SU-8 layer, the final rib waveguide structure is obtained.

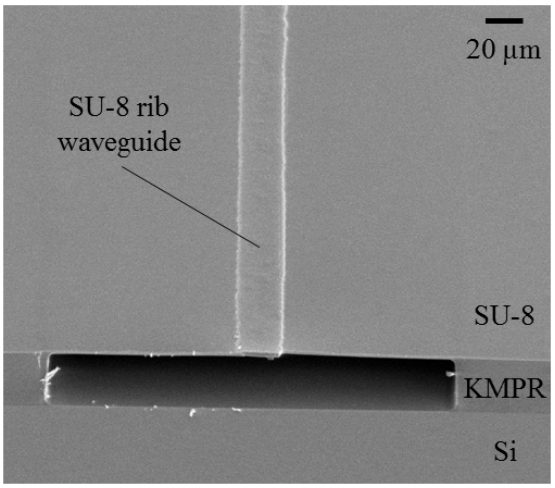

Figure 4.11: Angled scanning electron microscope (SEM) micrograph of an air-suspended rib waveguide structure after cleaving the sample. The SU-8 slab and rib are both approximately 2 μm thick with a 20 μm wide rib, while the KMPR microchannel is 25 μm high and about 250 μm wide.

structure is rinsed with isopropanol and dry blown using nitrogen (Fig. 4.10 (c)). Fig. 4.11 (a) shows an angled SEM image of the resulting exemplary air-suspended rib waveguide structure after cleaving with an active waveguide area of approximately 80 μm^2. The dimensions of the channel are about 250 μm width and 25 μm height. An approximately 2 μm thick laminated planar SU-8 layer with an accurately aligned air-suspended rib waveguide structure on top, approximately 2 μm thick and 20 μm wide, can be seen. The rib waveguide has the same thickness than the laminated layer underneath.

4.5 Waveguide characterisation

Characterisation of the fabricated air-suspended SU-8 rib waveguides has been carried out employing a butt coupling setup to couple light into the waveguide as shown in Fig. 4.12. The samples were cleaved into approximately 10 mm long pieces and were placed on a translation stage. To couple light into the waveguide a standard optical single-mode fibre with stripped cladding was mounted on a second translation stage using a fibre chuck. A camera system was employed to support the alignment of the fibre.

First the input fibre was aligned by the help of the camera and a visible laser (λ = 655 nm, 1 mW output power, Fibercheck, Laser Components GmbH). Fig. 4.13 (a) shows a photograph of the experimental demonstration of an air-suspended SU-8 rib waveguide excited from the left hand side with the visible laser source. Red light that is guided through the waveguide can be observed by the bright end facet of the waveguide on the right hand side of the sample. Afterwards a tunable laser (TUNICS T100S-HP, Yenista Optics S.A) was used to launch TE-polarized light (λ = 1550 nm) into the previously aligned waveguide. A beam profiler (BP209-IR, Thorlabs GmbH) was placed at the output facet of the waveguide. An intensity distribution of the waveguide was thus obtained (Fig. 4.13 (b)) with a resolution setting of the beam profiler of 1.2 μm. The experimental result underpins the simulation result indicating that the waveguide is single-mode.

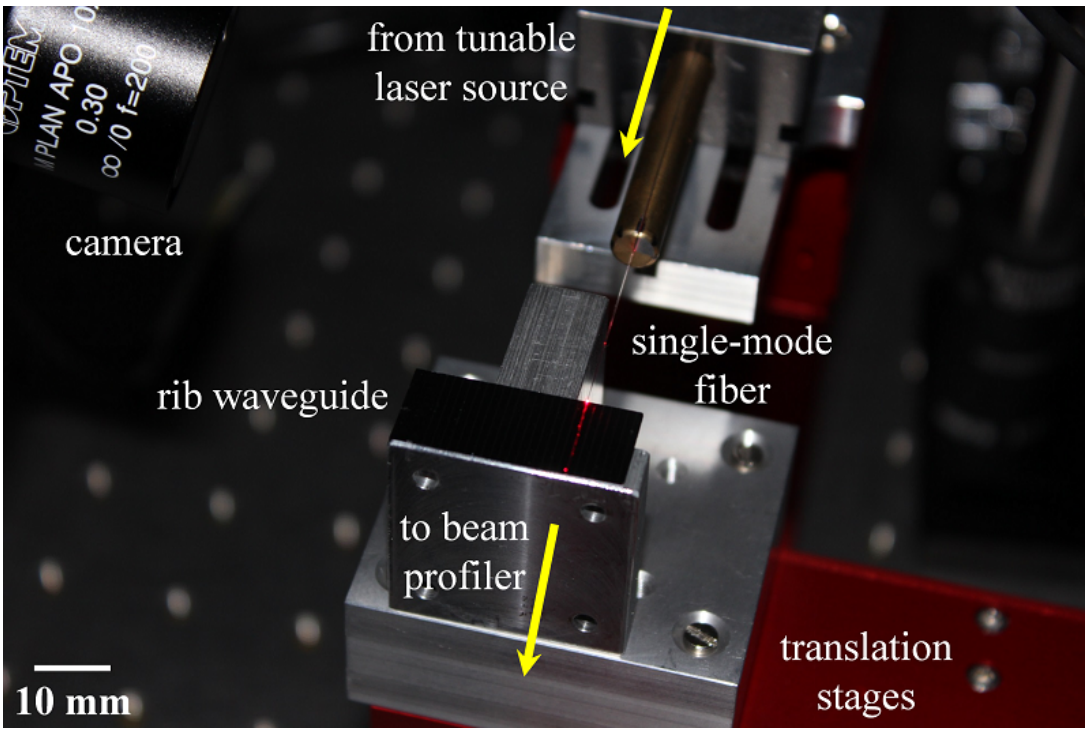

Figure 4.12: Butt coupling setup for the optical inspection of air-suspended polymer rib waveguides.

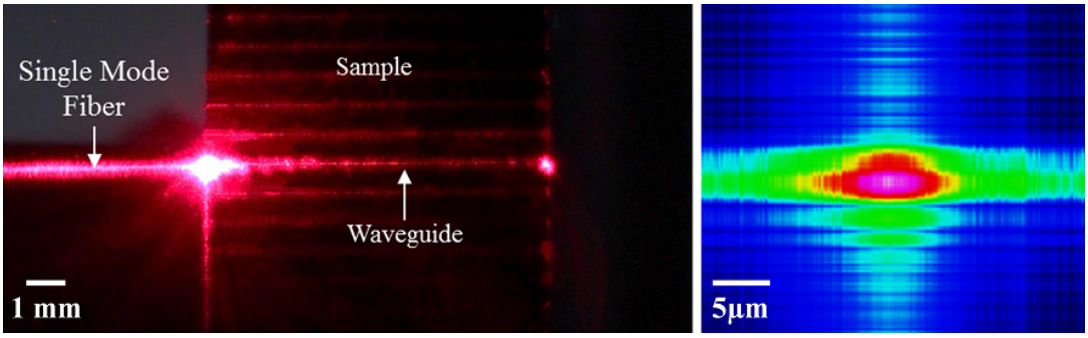

Figure 4.13: Results of the optical inspection. (a) Photograph of an air-suspended rib waveguide, approximately 4 μm thick and 20 μm wide, when visible light at $\lambda = 655$ nm is coupled into it, (b) intensity profile at the end facet of the rib waveguide obtained by a beam profiler with 1.2 μm resolution at $\lambda = 1550$ nm.

4.6 Conclusions

In this Chapter, single-mode large cross-section optical rib waveguides with an active waveguide area of approximately 80 μm^2 have been designed, realised and demonstrated. Initially, optical modelling was performed using first the effective index (EIM) to approximate the single-mode guidance of light followed by a validation using the beam propagation method (BPM). The simulation results indicated that large cross-section air-suspended rib waveguides in SU-8 can exhibit quasi-single-mode guidance for TE polarization. By exploiting the bonding method to seal air cavities of KMPR with a thin SU-8 film by using a flexible PDMS carrier stamp, combined with a subsequent photolithography step to define a rib structure, air-suspended rib waveguides have been successfully fabricated. In order to couple light into the waveguides, butt coupling was employed. Experiments have been carried out and waveguiding was demonstrated at visible and infrared wavelengths. A beam profile for $\lambda = 1550$ nm was obtained indicating single-mode behaviour of the rib waveguide.

Although single-mode guidance of light in an air-suspended SU-8 waveguide was demonstrated in the experiment, the employed butt coupling method for such thin waveguides with approximately 4 μm thickness is demanding and very time consuming. Furthermore, defining the optical structure by photolithography adds an extra step to the process. To obtain waveguides with good optical properties, for example low losses, a high-resolution photo mask would be required which is the reason why no further testing of the rib waveguides has been carried out.

As butt coupling is demanding and very time consuming, more advanced concepts and methods to couple light into the laminated SU-8 layers need to be investigated.

5 Grating coupler interface for air-suspended SU-8 waveguides

In Chapter 4 air-suspended single-mode rib waveguides have been proposed and demonstrated using the SU-8 onto KMPR lamination techniques of Chapter 3. Although the employed fabrication and light coupling method is very straightforward, it damages the fluidic channel underneath, limiting the usefulness for optofluidic devices. Thus, it would be beneficial if a more appropriate approach could be found that would maintain the integrity of the underlying air-cavity and allow access to the optical waveguide without any further end-facet preparation.

In this Chapter, light coupling into bonded SU-8 waveguides is studied employing air-suspended SU-8 surface grating couplers. Such structures can be created by patterned PDMS carrier stamps that already contain the optical structures.

Initially, an overview of concepts to couple light in and out of optical waveguides is presented. Then air-suspended SU-8 surface grating couplers are designed, numerically simulated, fabricated and characterised.

The main part of Chapter 5 is adapted from the published journal paper *"Air-suspended SU-8 polymer waveguide grating couplers"* [168]. This Chapter provides the necessary background knowledge for the following Chapter 6 and 7.

5.1 Introduction

Microscale integrated photonic circuits exploiting polymer materials are extremely attractive for low-cost and mass-producible applications, especially for sensing devices in the fields of biomedicine, healthcare, food safety or drug screening. In order to fabricate such small footprint photonic sensors, planar and monolithic fabrication methods including photolithography, hot embossing, and nanoimprint lithography have been found suitable [169–171]. However, interfacing the waveguide layer of these sensors to optical fibres is a challenging exercise due to the small waveguide cross-sections being often in the range of several hundreds of nanometres.

For integrated photonic devices fabricated in silicon-on-insulator (SOI), the well-known highly efficient surface grating couplers have been proposed and realized [21]. By using such grating couplers it is possible to couple light from an

optical fibre vertically into a thin single-mode waveguide layer and back into a fibre without cleaving and polishing processes. However, in contrast to semiconductors, conventional polymers do not offer large contrast in refractive index between the core and cladding (typically in the range of n = 1.30-1.70 [135]) making surface grating couplers considerably difficult to implement on a polymer based platform.

One strategy to overcome this issue is to increase the refractive index contrast by depositing a layer of high refractive index coating of SiN(Si_3N_4) on top of the grating coupler structures as described in Chapter 4, Section 4.1 [136, 137]. Another strategy, instead of adding a high-index layer, would be to introduce a porous layer below the grating couplers which reduces the cladding index and thus increase the refractive index contrast [138–140].

By exploiting the proposed fabrication method of bonding sub-micron SU-8 films onto KMPR microchannels of Chapter 3, air-suspended photonic devices with a maximum of refractive index contrast can be realized. This method allows the parallel production of photonic structures made entirely from polymers with air as lower and upper cladding layer.

In this Chapter, air-suspended polymer waveguide grating couplers exhibiting a high refractive index contrast by exploiting air claddings on top and at the bottom of the structures are presented. Numerical simulations are carried out in order to determine the maximum theoretical efficiency and to obtain a set of parameters that allow the fabrication using the proposed fabrication method for air-suspended photonic structures. Waveguides designed for TE polarized light with a wavelength of λ = 1550 nm connected with an input and an output grating coupler are fabricated and characterised.

5.2 Light coupling into photonic devices

In order to guide light in integrated optical waveguides, light from an external source needs to be coupled into and subsequently out of the waveguide for detection. In general, five coupling methods can be classified: butt, end-fire, prism, grating, and directional coupling. Each of these techniques is described in the following.

One of the simplest methods to couple light into an optical waveguide is butt coupling, as employed in Chapter 4, where an optical fibre is brought close or in direct contact (often via immersion oil) with the polished or cleaved input facet of the waveguide, as shown in Fig. 5.1 (a). The optical fibre and the waveguide can be aligned using a microscope or fibre alignment grooves. However, to achieve efficient coupling, the alignment as well as the mode match between fibre and waveguide are crucial [172]. Furthermore, with decreasing waveguide cross-sections, alignment is more difficult, especially for single-mode waveguides with dimensions of a few hundreds of nanometres.

In the case of end-fire coupling, the light is directly focused onto the polished or cleaved input facet of the waveguide by using a lens, as shown in Fig. 5.1 (b). In order to achieve efficient coupling, the end facets of the waveguides need to be extremely smooth and the numerical aperture of the focusing lens has to fit to the propagations constant of the mode exited in the waveguide core [172]. As described for butt coupling, a precise alignment with high mechanical stability is required for thin single-mode waveguides.

Another method to couple light into an optical waveguide is via prism coupling. By employing this method, a high-index prism is brought in contact with the waveguide, as shown in Fig. 5.1 (c), either directly or by using an immersion oil. When the waveguide is illuminated through the prism at an angle that matches the propagation constant of a guided mode of the waveguide, light is refracted and hence can be coupled into and also extracted from the waveguide [172].

In the case of waveguide grating coupling (Fig. 5.1 (d)), a periodic structure with an alternating refractive index is employed to couple light into and out of a waveguide. Incident light is diffracted into several higher diffraction orders by the grating. When a wave vector of the diffracted light matches a supported mode of the waveguide, coupling occurs while the higher order diffraction has to fulfil the conditions of total internal reflection. The principle is reversible and allows light to be diffracted out of the bound mode of a waveguide and into free space.

An optical directional coupler (Fig. 5.1 (e)) consist of parallel channel optical waveguides, that are in close proximity so that energy can be transferred from one to another. The light must propagate with the same phase velocity in each channel over a substantial length to couple. The amount of power coupled is determined by the overlap of the modes in the separate channels, the length of interaction

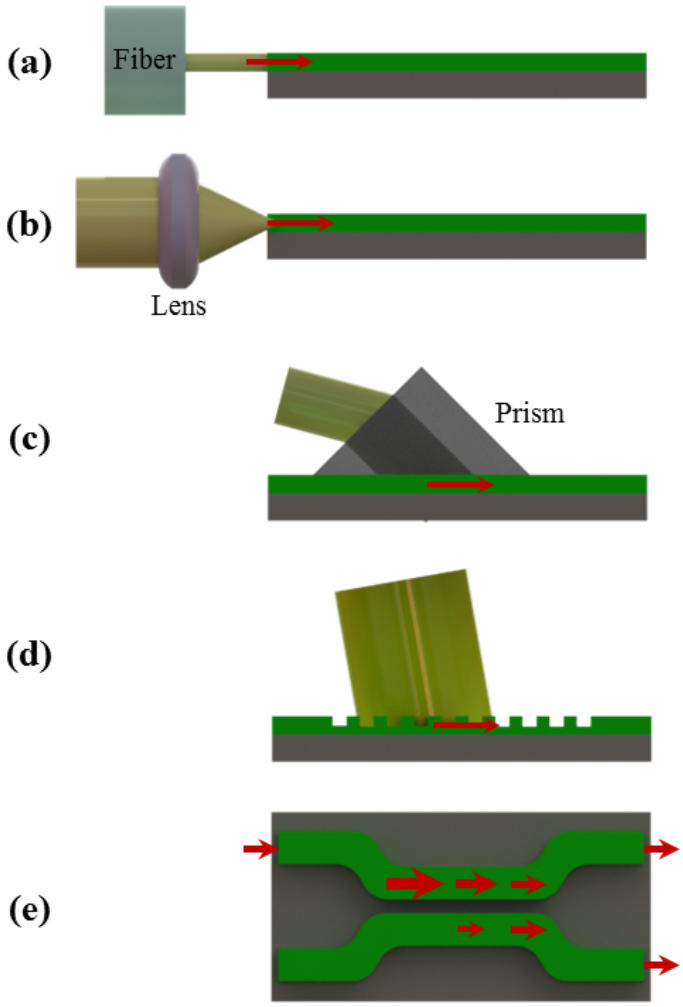

Figure 5.1: Light coupling methods for optical waveguides: (a) butt, (b) end-fire, (c) prism, (d) grating, and (e) directional coupling.

and the degree to which the two channels are phase matched [173]. Directional coupling can be effective; however, the light already needs to be coupled into one of the waveguides beforehand. One popular technique involves tapering an optical waveguide to the point where the light is evanescent around the fibre and then using this as one of the waveguides of a directional coupler.

5.3 Grating coupler design and simulation

Grating couplers are optical elements with an alternating refractive index, producing a phase match between particular waveguide modes and an unguided optical beam which is incident at an oblique angle to the surface of the waveguide [154].

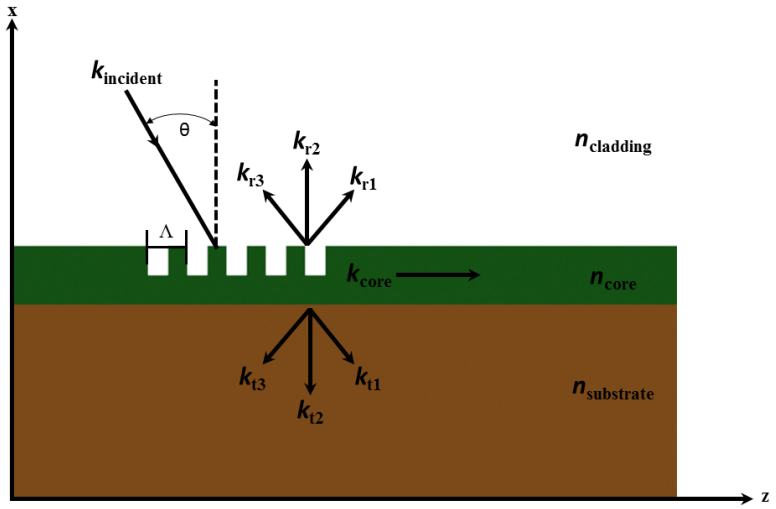

Figure 5.2: General grating coupler configuration with simplified representation of the beam diffraction on the surface of a grating coupler.

As shown in Fig. 5.2, incident light is partially reflected ($k_{r1}..k_{rn}$) and transmitted ($k_{t1}..k_{tn}$) into several diffraction orders at the surface of the grating. When a wave vector of the diffracted light matches a supported mode of the waveguide, coupling occurs while the higher order diffraction has to fulfil the conditions of total internal reflection. This effect can be described by the grating equation, which represents the relation between the wave vectors of the incident and diffracted waves. For grating couplers, the grating equation can be written as Eq. 5.1 [174]:

$$k_{incident}\ sin\theta + v\frac{2\pi}{\Lambda} = k_{core} \tag{5.1}$$

$$\text{with } k_{incident} = \frac{2\pi}{\lambda_0}\ n_{cladding} \tag{5.2}$$

$$\text{and } k_{core} = \frac{2\pi}{\lambda_0}\ n_{eff} \tag{5.3}$$

and with $k_{incident}$ the incident wave vector, λ_0 the wavelength, θ the incident angle, v the diffraction order, Λ the grating period, k_{core} the real part of the propagation constant and n_{eff} the effective refractive index of the guided mode.

The grating equation is only exact for structures with an infinite sequence of grating periods while in a finite structure not exactly one, but a range of k-vectors occur around the one predicted by the grating equation. It is referred to the Ph.D.

thesis of Dirk Taillaert [175] for a deeper understanding of the grating coupler theory.

When the incident beam is coupled in vertically from the top ($\theta = 0°$) half of the power will couple to the horizontal left and right hand side due to the symmetry of the grating. In order to achieve higher coupling efficiencies, slightly asymmetric gratings (typically θ = 5-10°) are employed. Furthermore, if the grating depth is much smaller than the waveguide thickness, approximately vertical symmetry can be assumed. The symmetry can be broken by using different materials as substrate or top cladding, or by adding a high-index reflective substrate below the waveguide [175].

In this Chapter, the proposed structure consists of an air-suspended straight polymer waveguide with a grating coupler element at each end for in and out coupling of light. The grating and the waveguide structures are both realized in SU-8 above a previously defined KMPR microchannel. Fig. 5.3 shows a schematic of the structure studied in this work. Silicon wafers are used as substrates. On top of the substrate, an air-cavity providing the air cladding is defined in a KMPR layer that acts as the base for the free-standing SU-8 waveguide and grating coupler elements. By employing such a structure with air as upper and lower cladding layer a large refractive index contrast for the proposed polymer grating couplers is achieved.

The main design parameters are the height of the waveguide t, the groove depth of the grating e and the period Λ. The centre wavelength of light used in the simulation is λ = 1550 nm with material refractive indices of n_t = 1.0 (air), n_g = 1.575 (SU-8) and n_s =1.55 (KMPR). The refractive index of the fibre core was set to 1.44 (silica). The numerical simulations are carried out using the eigenmode expansion tool CAMFR (CAvity Modelling FRamework) [166]. First, the single-mode condition for TE modes (cut-off thickness $d(TE)$) of the SU-8 waveguide can be calculated according to Eq. 5.4 [20],

$$d(TE) = \frac{m\pi + arctan\left(\frac{n_s^2 - n_t^2}{n_g^2 - n_s^2}\right)^{1/2}}{k(n_g^2 - n_s^2)^{1/2}} \tag{5.4}$$

with the order of the guided mode m, wave vector k and refractive indices for the top layer n_t, the substrate layer n_s and waveguide layer n_g. For TM polarized light the cut-off thickness $d(TM)$ can be calculated according to Eq. 5.5.

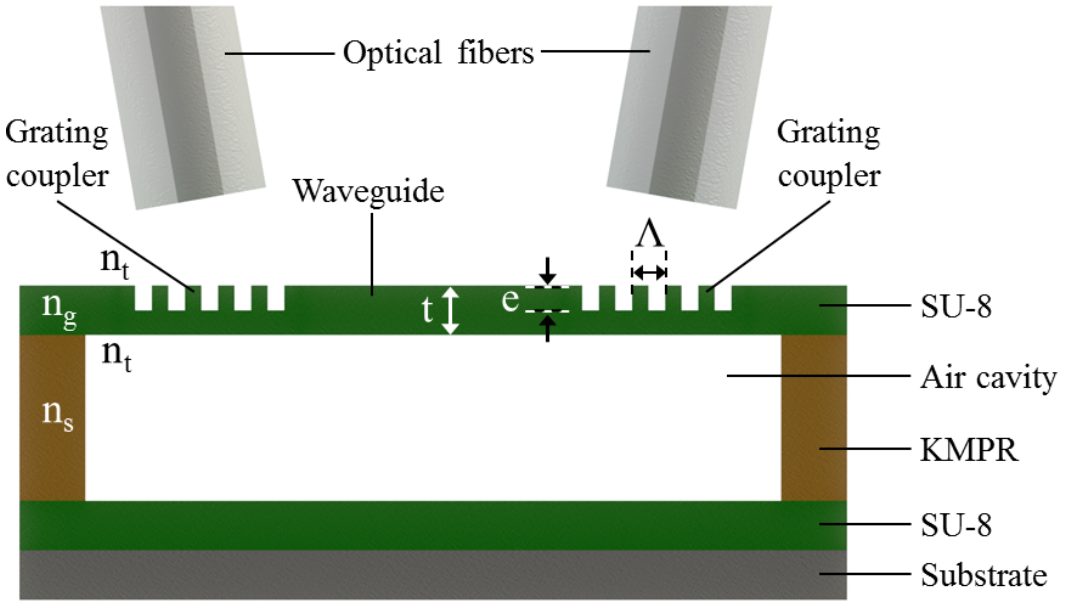

Figure 5.3: Schematic of the proposed air-suspended SU-8 polymer waveguide grating couplers (cross-section, not to scale).

$$d(TM) = \frac{m\pi + arctan\left[\left(\frac{n_g}{n_t}\right)^2 \left(\frac{n_s^2 - n_t^2}{n_g^2 - n_s^2}\right]\right)^{1/2}}{k(n_g^2 - n_s^2)^{1/2}} \tag{5.5}$$

After choosing an appropriate period and number of periods, the grating coupler is optimized to a maximum spectral response at a wavelength of $\lambda = 1550$ nm through the use of the well-known grating equation (Eq. 5.6),

$$n_{eff} = n_t sin(\theta) + m\frac{\lambda}{\Lambda} \tag{5.6}$$

with the effective refractive index of the grating region n_{eff}, the refractive index of the top cladding n_{t}, the coupling angle θ, the order of the mode m, the period of the grating Λ and the wavelength of light λ.

Fig. 5.4 illustrates the electric field distribution of an optimized grating coupler over an air-cavity with the following parameters at a coupling angle of $\theta = 10°$: thickness of the waveguide core $t = 0.6$ μm, groove depth of the grating $e = 0.3$ μm and grating period $\Lambda = 1.397$ μm. The width of the simulation window was 18.5 μm in order to meet the experimental setup which employs single-mode fibres with a core diameter of 10.5 μm and a slightly larger grating coupler area. The

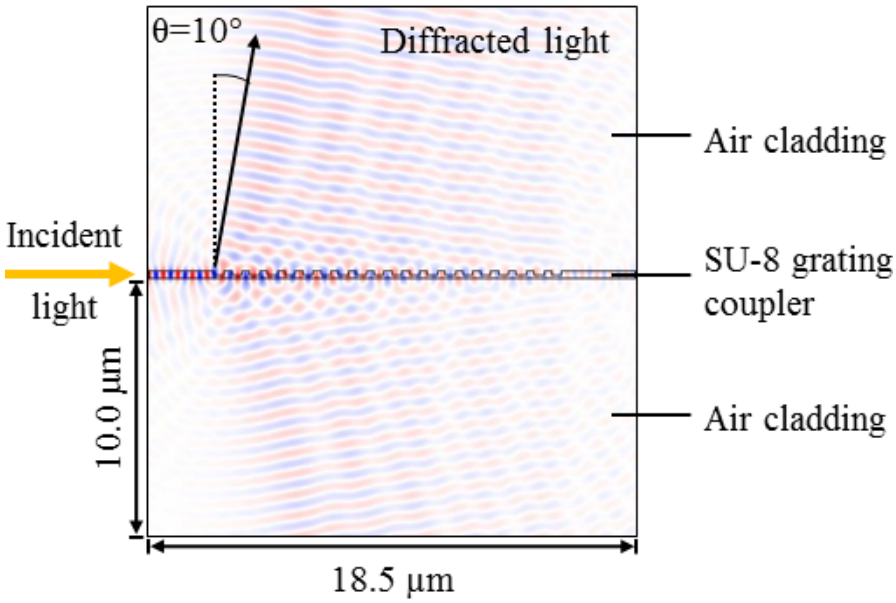

Figure 5.4: Electric field distribution with an air cladding on top and on the bottom of the grating coupler structure.

silicon substrate is not included in the simulation as the height of the air-cavity ensures that the evanescent tail of light extending from the polymer layer into the air decays rapidly due to the high refractive index contrast and thus is negligible by the time it reaches the silicon. The distance above and below the grating coupler structure is chosen to be 10 μm which is in the range of the distances between the sample and the input and output fibres that emit and collect the light in the experiment.

Fig. 5.4 shows that light that is emitted into the waveguide from the left hand side is diffracted by the periodic refractive index modulation of grating coupler into the free space at an angle of $\theta = 10°$. It can be seen that a significant amount of light also radiates downwards. Light that could be reflected back from the substrate might influence and disturb the coupling performance of the grating and has to be considered and possibly investigated during the experiments. On the other hand, in order to make use of such light, bottom reflectors could be employed [176, 177].

Fig. 5.5 shows the theoretical spectral response of an optimized air-suspended grating coupler for TE polarized light (blue solid line). If an air-cavity cladding and thus a large refractive index contrast of 1.575:1.0 ($\Delta_{RI} = 0.575$) is present as shown in Fig. 5.3, it can be seen that a single grating coupler exhibits approx-

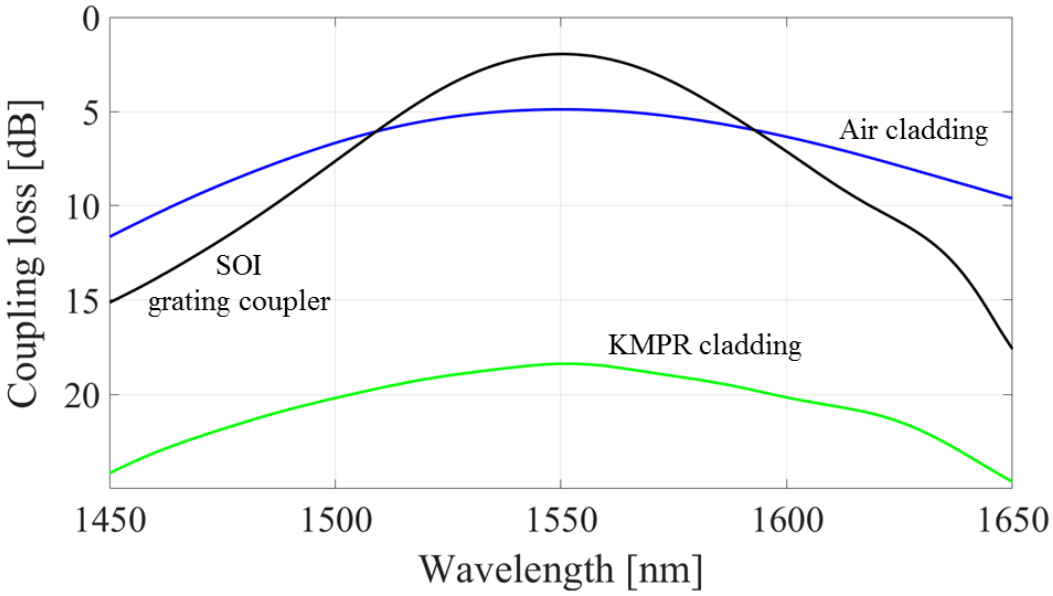

Figure 5.5: Calculated coupling loss to a single-mode optical fibre vs. wavelength for a TE mode SU-8 grating coupler with bottom air cladding (blue solid line) and with bottom KMPR cladding (green solid line) in comparison to a regular SOI grating coupler (black solid line, data according to Ref. [178]).

imately 4.9 dB coupling loss, indicating a coupling efficiency of approximately 32 % at a maximum spectral response of 1550 nm. In contrast, an SU-8 grating coupler structure that is based on a polymer cladding such as KMPR has a low refractive index contrast of 1.575:1.55 ($\Delta_{RI} = 0.025$), resulting in high losses of approximately 18.5 dB and a weak maximum efficiency of 1-2 % (green solid line). In comparison to polymer grating couplers, regular SOI grating couplers employing Si ($n_{Si} = 3.47$) and SiO_2 ($n_{SiO_2} = 1.44$) can achieve higher contrasts of $\Delta_{RI} = 2.03$ and hence higher coupling efficiencies of around 2.2 dB, or approximately 60 % [178], as shown in Fig. 5.5 (black solid line). These examples clearly demonstrate that grating couplers generally require large refractive index contrasts in order to achieve practical efficiencies. The refractive index contrast that is possible with the air-suspended SU-8 waveguide can give relatively high efficiency which may be practical for optofluidic devices.

Further simulations have been carried out in order to study the influence of different grating parameters on the optical behaviour of the air-suspended grating couplers. These additional simulations can be found in the Appendix A (p. 152 ff).

For all of the described simulations, all parameters were kept constant while the investigated parameter was varied.

In summary, if the waveguide thickness is changed within the single-mode condition (Eq. 5.4 and 5.5), the effective index changes and thus the phase matching condition with approximately 7 pm shift in resonant wavelength per nm change in thickness of the waveguide (Fig. 8.1, Appendix A).

The filling factor is important to achieve the optimum coupling efficiency. The optimum value of filling factor is around 0.5 while variations cause a shift towards shorter wavelengths for values lower than 0.5, while higher values result in a shift towards longer wavelengths (Fig. 8.2, Appendix A).

Variations of the groove depth cause a shift of the grating coupler spectrum and a change in the coupling loss. The shallower a grating is the weaker it is in terms of coupled light efficiency. Deeper gratings result in a shift towards shorter wavelengths (Fig. 8.3, Appendix A).

When the grating period is varied, the spectral response of the grating coupler shifts towards longer wavelengths with increasing period which can also be theoretically predicted from the grating equation (Eq. 5.6) while the coupling loss stays almost constant at around 5 dB (Fig. 8.4, Appendix A).

Adjusting the angle of the incident light over a range of about 4° to 18°, can cause a shift in the resonant wavelength towards shorter wavelengths of about 15 nm/° (Fig. 8.5, Appendix A). This behaviour can be the most useful option in the experiment as it does not require structural changes on the grating couplers to bring the optimum coupling wavelength in the centre of the measurement window of the optical spectrum analyser.

5.4 Grating coupler realisation

Air-suspended SU-8 waveguide grating couplers have been fabricated as explained in Chapter 3 using a 0.5 μm thick SU-8 film and a PDMS carrier stamp which contains the waveguide and grating coupler structures. Due to the small feature sizes of the gratings in the submicron range, first a silicon master with the waveguide and grating structures is produced by electron beam lithography and subsequent Ar^+ ion beam etching (IBE). Fig. 5.6 (a) shows a part of the master of the grating coupler structures. From Fig. 5.6 (b) it can be seen that the side walls of the

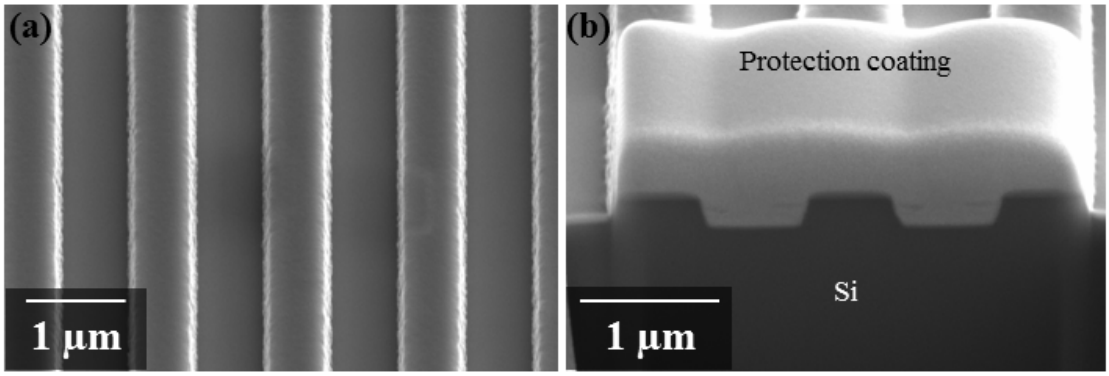

Figure 5.6: (a) Scanning electron microscope image (SEM) of the silicon master of the grating coupler structures and (b) SEM image showing not perfectly rectangular lines and spaces of the grating with an angle of approximately 72°.

lines and spaces of the grating are not perfectly rectangular having an angle of approximately 72°.

Then the microchannels acting as a base for the grating coupler structures are patterned in a 25 μm thick layer of the KMPR by standard photolithography on top of a Si substrate as shown in Fig. 5.7 (a). In order to reduce wear on the silicon master, a PFPE working mould is cast (Fig. 5.7 (b)). From this working mould multiple PDMS carrier stamps can be cast as shown in Section 3.3.1 (Fig. 5.7 (c)). In order to avoid temperature induced expansion of the materials, the curing for PDMS was carried out at room temperature for 48 h. Then the PDMS carrier stamp is plasma treated as explained in Section 3.3.1 and a 0.5 μm thick SU-8 layer is spin coated on top (Fig. 5.7 (d)). In contrast to the method used in Chapter 3, cross-linking of the laminated SU-8 layer is carried out at room temperature as well for 48 h to avoid possible expansion of the materials (Fig. 5.7 (e)). Finally, the PDMS carrier stamp can be peeled off (Fig. 5.7 (f)). In the employed carrier stamp design 54 grating coupler structures of different size, period and length can be laminated onto one sample at the same time.

Due to current limitations in the fabrication process of the master by electron beam lithography and subsequent IBE, the depth of the gratings is approximately 120 nm less than the optimum depth calculated in the simulation, resulting in a weaker perturbation of the grating couplers and hence in lower coupling efficiencies in the experiment. Mainly, the currently employed etching process using IBE only allows a grating depth of approximately 200 nm in combination with a reasonable side-wall steepness of the structures.

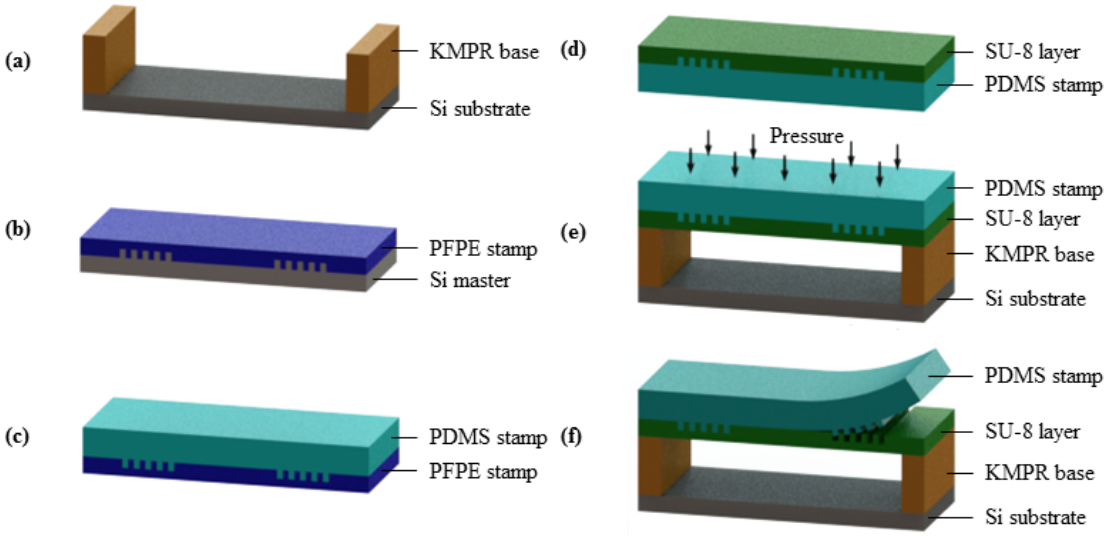

Figure 5.7: Overview of the fabrication steps of air-suspended SU-8 waveguide grating couplers. (a) definition KMPR microchannels by standard photolithography; (b) PFPE working mould casting from silicon master; (c) PDMS casting from PFPE working mould; (d) plasma treatment of PDMS and spin coating of SU-8 layer; (e) cross-linking of SU-8 onto KMPR microchannels by applying pressure; (f) peeling off the PDMS carrier stamp after cross-linking of the SU-8 film.

Fig. 5.8 (a) presents a top view of such a structure taken with an optical microscope. The KMPR base that sustains the air-suspended SU-8 film can be seen on the left and right side of the image. The laminated SU-8 film itself appears in a reddish colour due to thin film interference while deeper structures such as the waveguide trenches and the spaces of the grating appear blueish. In order to define the waveguides in the laminated SU-8 layer, waveguide trenches are employed that have the same depth as the grating structures. In addition to the 2D simulation model of the grating couplers in Fig. 5.3 which provided information about the height and the length, the trenches define the width of the structures.
Fig. 5.8 (b) shows an angled cross-section taken with a scanning electron microscope (SEM) after cleaving the sample. The dimensions of the microchannel are approximately 250 μm width and 25 μm height. An additional 50 μm thick SU-8 coating has been introduced and processed on top of the Si substrate which functionality is explained in detail Section 5.5. It can be seen that the complete grating coupler and waveguide structure is suspended in air. As can be assumed from the colours in the microscope image, the thickness of the features in the laminated SU-8 layer is uniform along the microchannel structure.

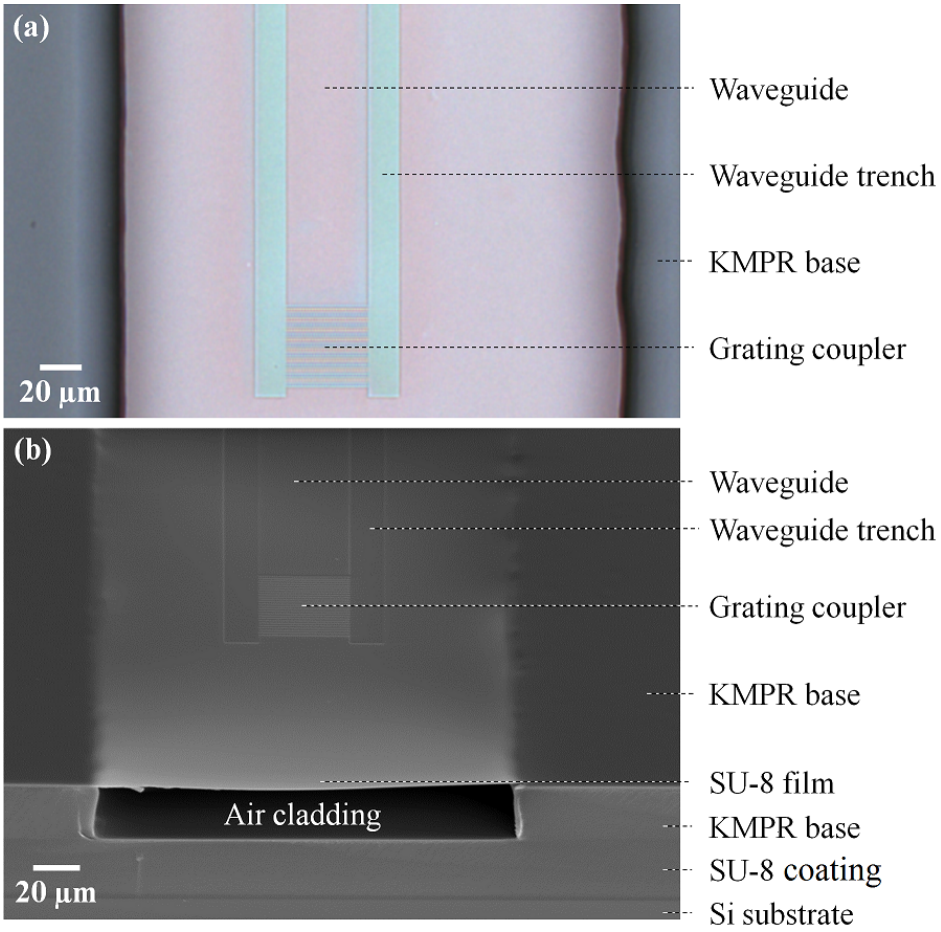

Figure 5.8: Visual inspection of the fabricated air-suspended grating coupler, (a) top view microscope image and (b) angled scanning electron microscope (SEM) micrograph after cleaving the sample.

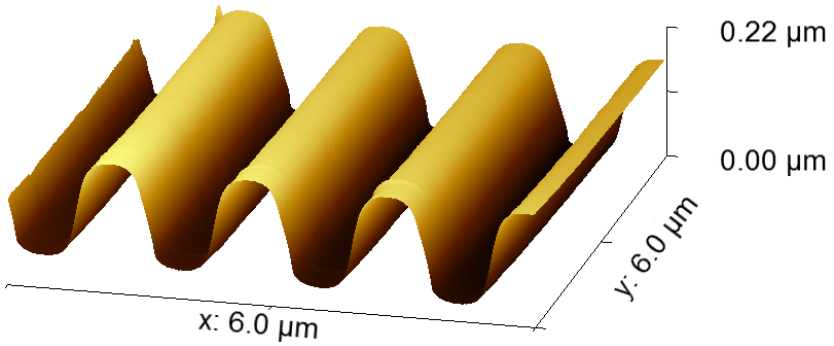

Figure 5.9: Atomic force microscope (AFM) measurement of the final grating coupler structures in SU-8.

The size of the fabricated test grating couplers are 40 μm in width and length with different periodicities (1.46 μm to 1.65 μm) and waveguide lengths (500 μm, 750 μm and 1000 μm). The height of the waveguides fulfil the single-mode condition (Eq. 5.4) for $\lambda = 1550$ nm, while the width is kept constant at 40 μm. Atomic force microscope (AFM) measurements have been carried out in order to evaluate the dimensions of the fabricated grating couplers. Fig. 5.9 shows a tip-convolution corrected three-dimensional image of a part of a grating coupler. It can be seen that the shape of the resulting grating has rounded corners. The rounded shape can be explained by the not perfectly rectangular lines and spaces of the grating with an angle of approximately 72° as shown in Fig. 5.6 and by the threefold replication process using a PFPE working mould and a PDMS carrier stamp to transfer the structures into SU-8.

Furthermore, it has to be considered that during AFM scanning, a geometrical interaction (convolution) between the tip and the sample surface features is being imaged due to the finite sharpness and the characteristic geometry of the tip [179, 180]. This convolution effect is responsible for lateral broadening of surface protrusions [181]. However, the periodicity of the gratings is measured accurately.

Due to the fabrication tolerances of the processes and the thermal expansion in the threefold replication of the master, the fabricated grating structures were on average 1.5 % smaller in the periodicity than designed. The height of the line and spaces of the gratings was measured to be on average 178 nm.

5.5 Grating coupler characterisation

Coupling efficiency studies of the fabricated air-suspended waveguide grating couplers have been carried out using a transmission measurement setup as shown in Fig. 5.10. A custom-made Python[2] based software controls the translation stages and associated equipment (tunable laser, optical spectrum analyser). The software can directly interpret photonic structure designs such as grating couplers that have been created using the software IPKISS[3] and can perform custom measurement

[2]Python is a free-to-use, open source, object-oriented programming language designed for simplicity. [182]

[3]IPKISS is a parametric design framework focused (but not limited) to Photonic circuit design, constructed at Ghent University and IMEC. Through a python scripting interface, IPKISS allows the designer a fine-grained control of the different steps in photonic design. [183]

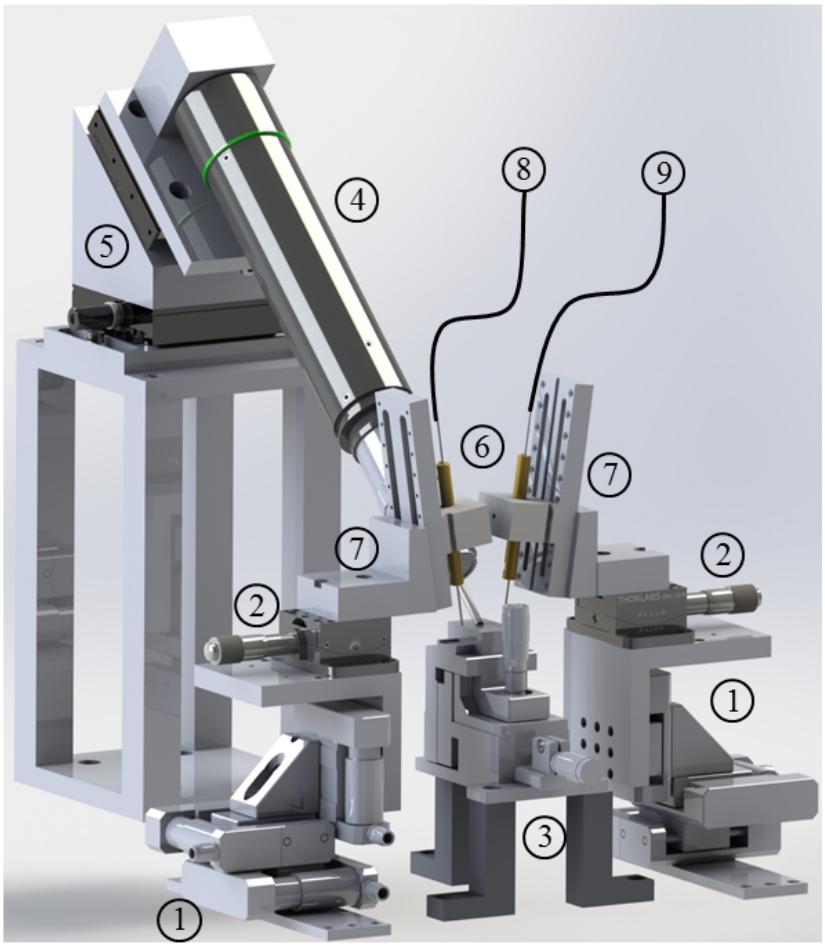

Figure 5.10: Schematic model of the experimental setup to characterise air-suspended grating couplers (not to scale). The employed parts of the transmission measurement setup are following: (1) YXZ linear stages, (2) goniometers, (3) sample stage, (4) telecentric camera, (5) camera stages, (6) input/output single-mode optical fibres, (7) fibre holder, (8) from tunable laser and (9) towards optical spectrum analyser.

sweeps and data views. In order to find the maximum spot of transmission trough the grating couplers and the waveguide in between, an automatic alignment tool was implemented which can scan the complete grating areas in a grid by intensity. Different parameters can be set including the scanning area, resolution (step size of the stage), laser power, wavelength and number of measurements taken at each individual scan position. After each scan, the user can select whether the optical fibre should move back to its initial position or to the highest spot of transmission that has been measured. Fig. 5.11 (a) shows an image of a scanned grating. The scanned area is 80 $\times$ 80 μm where the cold colours (bluish) indicate low inten-

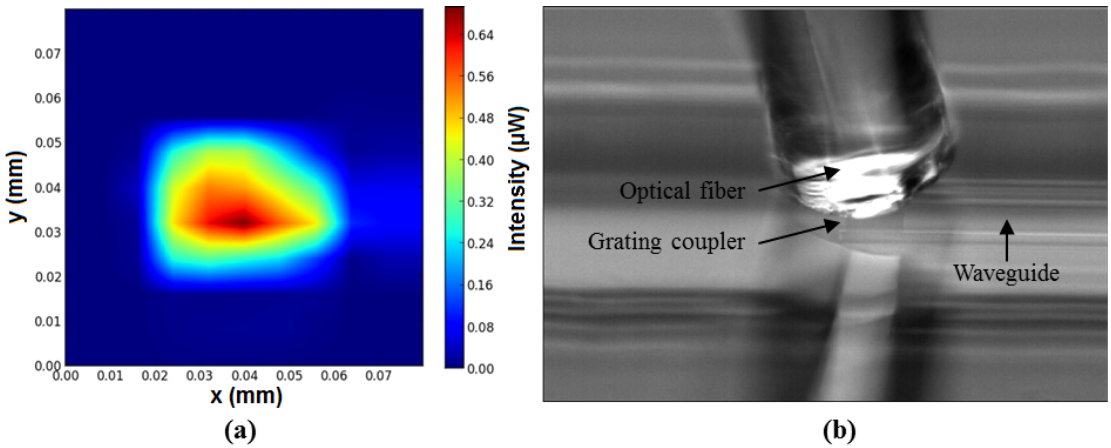

Figure 5.11: Automatic alignment of the optical fibres in the transmission measurement setup. (a) Intensity profile of a grating scanned by the alignment software and (b) positioned fibre over an air-suspended grating coupler after the alignment procedure.

sity and warm colours (reddish) high intensity. Interestingly, the grating area of 40 × 40 μm can be easily identified.

The maximum transmission of the grating can be found almost in the centre of the grating. As explained above, the fibre can be positioned exactly at this position after the automatic scanning process.

Fig. 5.11 (b) shows an image taken with the telecentric camera of the setup of a positioned fibre above a grating coupler after the scanning process. In order to obtain the best spot of transmission the scanning procedure is carried out multiple times for the input and output grating coupler. For the measurements, two identical cleaved standard single-mode fibres providing light to the input and collecting light at the output grating are connected to a tunable laser (TUNICS T100S-HP, Yenista Optics S.A) and an optical spectrum analyser (OSA, AQ6370C, Yokogawa Electric Corporation), respectively. A polarization controller is employed to launch TE polarized light into the input coupler. Both fibres are positioned at a tilted angle to the grating surface and are automatically aligned to the position where the highest transmission occurs by scanning the grating couplers in a fine mesh grid.

The grating coupler efficiency is determined by subtracting the coupling loss, the loss of the straight waveguide between the couplers and the assumed mode mismatch loss between the fibre mode and the diffracted field of the output grating

Loss	[%]	[dB]
System loss (opt. fibre and polarization controller)	64 %	1.93 dB
Waveguide loss (cut-back method)	59.29 $\frac{\%}{cm}$	2.27 $\frac{dB}{cm}$
Coupling loss both gratings	0.35 %	24.61 dB
Coupling loss single grating	5.88 %	12.31 dB
Calc. mode mismatch loss for 40 μm wide grating	39.8 %	4 dB

Table 5.1: Overview of the different system and grating coupler losses.

coupler. The waveguide losses were obtained from average values of more than 350 individual measurements of waveguides with different lengths exploiting the cut-back method and were measured to be a maximum of 13 dB cm^{-1} depending on the waveguide quality, whereas the best results have been in the range of previously reported losses in SU-8 waveguides of around 3 dB cm^{-1} [184]. For the experiments the attenuation is assumed to be 3 dB cm^{-1}. The losses of the input and output grating couplers are assumed to be equal due to the symmetric structures and measurement setup. Tab. 5.1 shows a complete overview of the different system and grating coupler losses.

The experimental results taken with a wavelength resolution of the OSA of 0.25 nm are shown in Fig. 5.12. The black solid line (measurement (a)) presents the coupling loss to a single-mode optical fibre vs. wavelength graph for the initial grating coupler design with a periodicity of 1.44 μm, measured at a fibre angle of 12°. It can be clearly seen that the spectral response of the grating coupler is oscillating suggesting multi-path interference.

One possibility is that the observed interference is due to a Fabry-Pérot type resonance which could occur from multiple reflections from various parts of the grating coupler design. Multiple potential locations at which reflections could occur can be identified including inferences within the gratings, fibre-to-fibre, grating-to-grating, fibre-to-grating, fibre-to-OSA and grating-to-substrate interferences.

However, as can be seen in Fig. 5.12, the oscillations are spanning approximately 15 dB in coupling loss which would suggest that the reflections for any Fabry-Pérot cavity would need to be very strong and well matched. Furthermore, it seems that these oscillations have a dominant period with a large spectral range indicating a very small cavity which is much smaller than the length of the waveguide between the gratings (1000 μm).

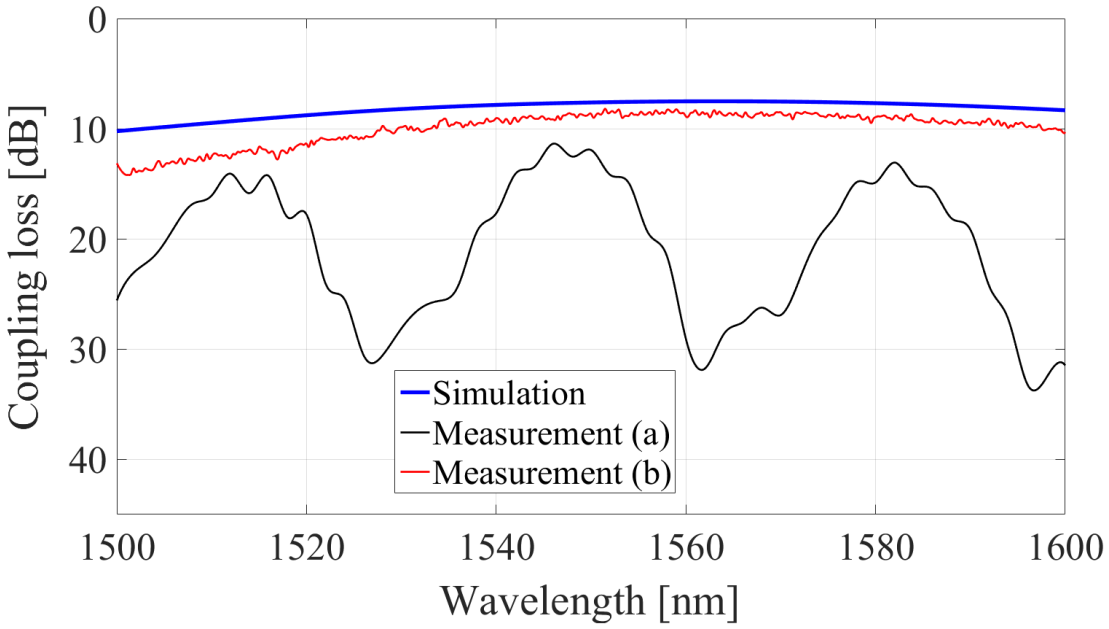

Figure 5.12: Measured coupling loss to a single-mode optical fibre vs. wavelength of the fabricated air-suspended grating couplers, (a) without (black solid line, $\Lambda = 1.44$ μm, $\theta = 12°$)) and (b) with (red solid line, $\Lambda = 1.46$ μm, $\theta = 16°$) a 50 μm thick SU-8 coating on the silicon substrate and additional temperature stabilisation at 23 °C. The blue solid line shows the simulation result for updated experimental parameters.

A second possibility is that the observed resonance is due to a type of Mach-Zehnder interference between two co-propagating waves with a slightly different phase velocity. Assuming this case, another mode with a lower effective refractive index would be present. This mode could be a so called anti-resonant reflecting optical waveguide (ARROW) mode [185]. Such modes are not true guided modes and thus always leaky. Even though, a ARROW mode can be formed in a low index core with a high index cladding and can propagate with relatively low loss over large distances. The key is that the mode must propagate almost paraxially within the low index material, making an almost glancing angle with the high index cladding to achieve almost 100% reflectivity.

Here, in the grating coupler design, this case could be possible with the high index silicon substrate and the air-cavity beneath the suspended SU-8 layer. The first order mode of the air-suspended SU-8 waveguide is just cut-off and hence radiates into the air almost parallel to the waveguide. When this mode is incident on the silicon substrate, almost 100% reflection will occur and thus this light can

be returned to the waveguide. It is thus possible that a significant amount of power could be returned to the output grating coupler where it will interfere with the light that was guided through the SU-8 waveguide. In order to suppress the secondary light path in the air-cavity, an additional SU-8 coating, approximately 50 μm thick, was introduced on the silicon substrate as shown in Fig. 5.8 (b).

A 50 μm thick SU-8 layer can support many modes and also all modes which would leak into the silicon substrate. The effective refractive index of these SU-8 slab modes will be close to the effective refractive index of the air-suspended SU-8 waveguide modes. Thus, it is reasonable to expect that the leaky first order SU-8 waveguide mode could easily couple to a resonance in the SU-8 slab and be subsequently radiated into the silicon substrate. This should suppress any ARROW resonance that was present in the substrate without the addition of the SU-8 layer on the silicon substrate.

The red solid line (measurement (b)) in Fig. 5.12 shows the coupling loss to a single-mode optical fibre vs. wavelength graph of a similar grating coupler structure with the additional SU-8 coating on the silicon substrate. Furthermore, the temperature of the sample was stabilized at 23 °C during the measurement. From the graph, it can be seen that the observed resonance behaviour is suppressed supporting the hypothesis that an ARROW resonance was responsible for this phenomenon. Further investigations in terms of numerical simulations would be required in order to pursue this hypothesis.

The grating coupler shown in measurement (b) has a periodicity of 1.46 μm and is measured at a fibre angle of 16° in order to have the optimum coupling wavelength in the centre of the measurement window of the optical spectrum analyser. The centre wavelength of the spectral response is at 1557 nm with approximately 8 dB coupling loss per grating indicating a coupling efficiency of 16 %. According to the cut-back method measurements, the waveguide losses in the experiments could be estimated as 3 dB cm^{-1}. A higher loss is expected from the mode mismatch of the diffracted field of the output grating coupler with approximately 40 μm width and the spot size of the output single-mode optical fibre with approximately 10 μm diameter. As a result, only a fraction of the light that is coupled out of the output grating coupler is collected by the single-mode optical fibre. Since the waveguide between the two grating couplers can act as a multi-mode interferometer, after a certain distance, all of the modes will accumulate multiples of 2 π phase shift and

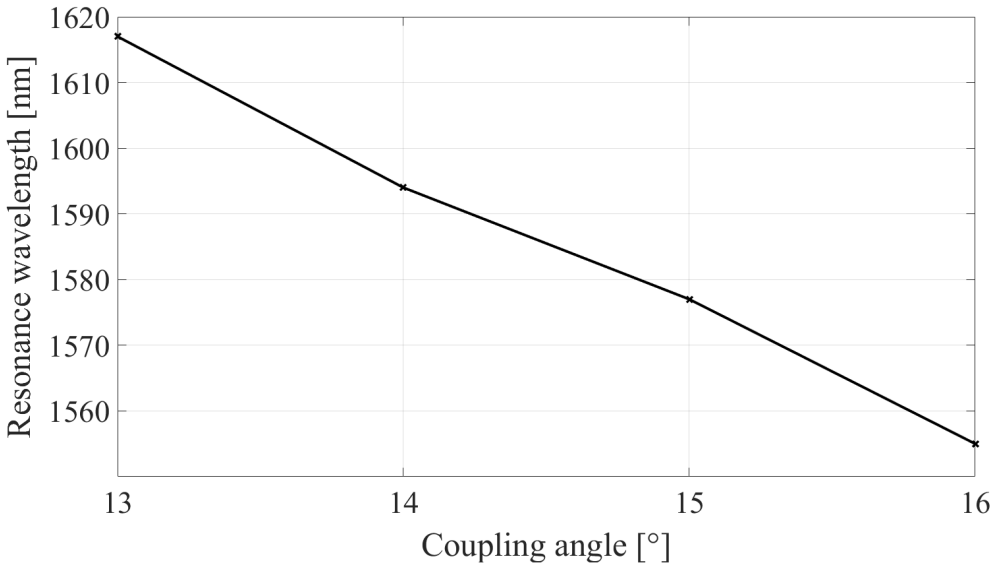

Figure 5.13: Measurement of the spectral response vs. the coupling angle. With increasing the coupling angle, the spectral response shifts towards shorter wavelengths with an average shift of approximately 21 nm/° over 60 nm.

will form an image of the input fibre spot. This would be the optimal situation for minimal coupling loss in the system. To obtain an estimate of the mode mismatch loss, we assume that the light at the output is a Gaussian distribution over the waveguide width and can be calculated by their integrals being in the range of about 4 dB.

Based on the experimental dimensions of the grating ($\Lambda = 1.46$ μm, $e = 0.178$ μm and $\theta = 16°$) the grating structure was re-simulated as shown by the blue solid line in Fig. 5.12. Here it can be seen that a single grating coupler exhibits approximately 7.5 dB coupling loss, which is 0.5 dB less than the experimental results. The discrepancy in the efficiency between the simulation and the experiment can be explained by several factors including the alignment of the optical fibre and the diffracted field as well as the assumed mode mismatch between the fibre mode and the diffracted field. One possible method to improve the efficiency of coupling could be the use of curved grating couplers to focus the light towards the output fibre [186].

As the coupling angle is the easiest available parameter to shift the spectral response and to bring the optimum coupling wavelength into the centre of the measurement window of the optical spectrum analyser, its influence has been studied.

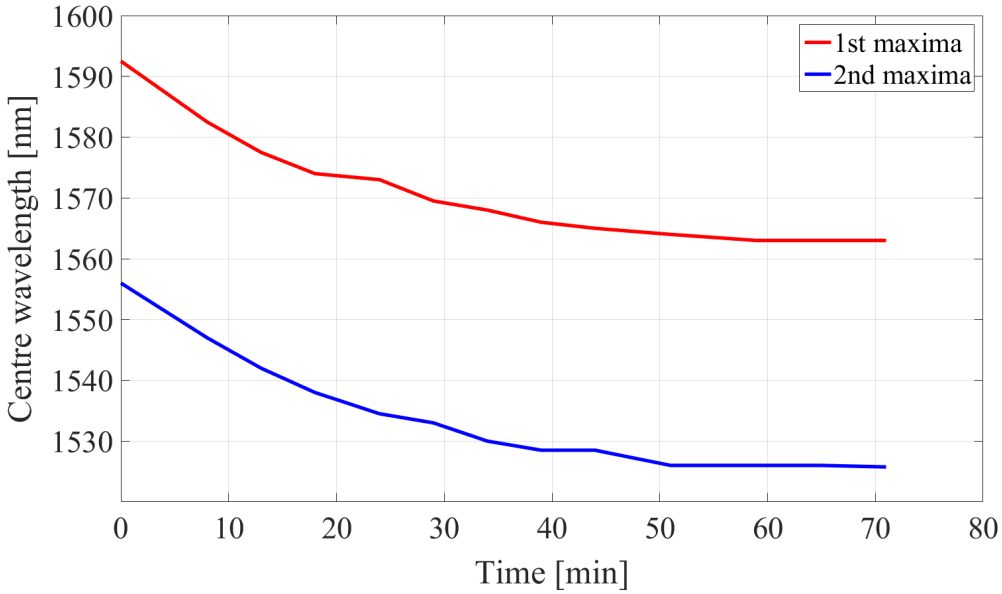

Figure 5.14: Heating curve (centre wavelength of the individual interference maxima vs. time) of air-suspended SU-8 grating couplers without an SU-8 coating on the silicon substrate when heating the sample from 24 °C to 26 °C. In the beginning of the heating procedure, three interference maxima can be seen (similar to Fig. 5.12) while the last two are monitored. Their centre wavelengths are at around 1556 nm for the first maxima (blue solid line) and 1592 nm for the second maxima (red solid line). After approximately 60 min the centre wavelengths have shifted towards 1526 nm and 1563 nm, respectively, and no further shift in the spectrum can be observed. The shift in the centre wavelength caused by the temperature change is approximately -15 nm K^{-1}.

In the experiment, the angles of both optical fibres (input and output) have been varied in the same manner between coupling angles of 13° to 16°.

Fig. 5.13 shows the measurement results. As can be seen, with increasing the coupling angle, the resonance wavelength shifts towards shorter wavelengths with an average shift of approximately 21 nm/° over 60 nm which is about 5 nm higher than simulated in Section 5.3 (Fig. 8.5, Appendix A). However, this graph should mainly demonstrate that the spectral response can easily be shifted by adjusting the angle of the coupling optical fibres.

Furthermore, during the measurements of the grating couplers without the SU-8 coating on the silicon substrate, a relatively high sensitivity to temperature changes has been observed. To evaluate the temperature influence on the grating coupler spectrum, a temperature control was implemented into the measurement setup.

Then a sample was heated from 24 °C to 26 °C. Three interference maxima were obtained in the measurement window of the OSA (similar to Fig. 5.12) while the last two have been monitored. Fig. 5.14 shows the corresponding heating curve (centre wavelength of the individual interference maxima vs. time). It can be seen that in the beginning of the heating procedure, the centre wavelength of the first maxima (blue solid line) is at around 1556 nm while the second maxima (red solid line) is at around 1592 nm. After approximately 60 min no further shift of the centre wavelengths of the two interference maxima can be observed and the spectrum seems to be stable. However, the the centre wavelength of the two maxima have shifted towards 1526 nm (blue solid line) and 1563 nm (red solid line), respectively resulting in a huge shift of approximately -15 nm K^{-1}. Thus, all further measurements of grating coupler samples have been carried out at 23 °C to keep the spectrum of the sample stabilized. However, the temperature sensitivity for grating couplers with SU-8 coating on the silicon substrate should be evaluated.

5.6 Conclusions

In this Chapter, a grating coupler interface for air-suspended SU-8 waveguides has been designed, realised and demonstrated.

In the proof-of-concept design, two grating couplers are connected by a waveguide with single-mode condition in the vertical dimension. The numerical simulations that have been carried out demonstrated a maximum coupling loss of 4.9 dB, indicating a coupling efficiency of approximately 32 % at a maximum spectral response of 1550 nm. Transmission measurements of the fabricated structures have shown that a single grating coupler exhibits approximately 8 dB coupling loss at a centre wavelength of 1557 nm indicating a coupling efficiency of 16 %. Even though the achieved coupling efficiencies are lower than for SOI couplers, mainly due to current fabrication limits of the master structures, the fabrication method employing widely used polymer materials has the advantage that multiple air-suspended structures can directly be created in only one simple lamination process without the need of additional etching steps.

The slightly lower coupling efficiencies in the experiment can be explained by the current limitations of the depth of the grating couplers in the fabrication process of the master by electron beam lithography and subsequent IBE resulting in a generally weaker perturbation of the gratings. Mainly, the currently employed

etching process using IBE only allows a grating depth of approximately 200 nm in combination with a reasonable side-wall steepness of the structures.

The first transmission measurements have shown, that the configuration of the fabricated grating couplers exhibited oscillating spectral responses suggesting multi-path interference. One possibility is that the observed interference is due to a Fabry-Pérot type resonance which could occur from multiple reflections from various parts of the grating coupler design.

A second possibility is that the observed resonance is due to a type of Mach-Zehnder interference between two co-propagating waves with a slightly different phase velocity. In the grating coupler design, this case could be possible with the high index silicon substrate and the air-cavity beneath the suspended SU-8 layer. In order to suppress the secondary light path in the air-cavity, an SU-8 coating on the silicon substrate, approximately 50 μm thick, was introduced for all further measurements. However, the introduced coating is not the optimal solution as depending on the alignment and the distances of the optical single-mode fibres to the grating couplers, such interferences can occasionally still occur.

Future work on the air-suspended grating coupler should include the implementation of a high-quality anti-reflection layer. Further improvements of the general performance of the grating couplers can be made by reducing the grating coupler width to minimize the mode mismatch of the diffracted field of the output grating coupler and the spot size of the output single-mode optical fibre and by tapering the waveguide down to single-mode conditions in the horizontal dimension. Another significant improvement towards higher coupling efficiencies would be to employ curved grating couplers to focus the light towards the output fibre.

Furthermore, it was seen that the spectrum of the polymer grating couplers without SU-8 coating on the silicon substrate is very sensitive to temperature changes and thus a temperature control was implemented into the measurement setup to stabilize the temperature of the samples at 23 °C. Since polymer materials exhibit a strong temperature dependence, the thermal sensitivity of the proposed air-suspended SU-8 grating coupler is studied in the following Chapter.

6 Thermal sensitivity of air-suspended SU-8 grating couplers

In Chapter 5 it was observed that the polymer grating coupler spectra can be sensitive to temperature changes. Since polymer materials generally exhibit a strong temperature dependence, both in thermal expansion and also in terms of thermo-optic variations in refractive index, the temperature sensitivity of air-suspended SU-8 polymer waveguide grating couplers for TE polarized light are studied in this Chapter.

Numerical simulations are carried out in order to estimate the wavelength shift expected due to the change of the temperature followed by experimental evaluation. Due to the small positive thermal expansion and large negative thermo-optic coefficient of SU-8, a shift towards shorter wavelengths is expected. The main part of this Chapter is adapted from the published journal paper *"Tunable air-suspended polymer grating couplers"* [187].

6.1 Introduction

In Chapter 3 a polymer fabrication method for air-suspended integrated photonic devices was presented that is maximizing the refractive index contrast by exploiting air as the top and bottom cladding layer. Furthermore, based on the presented method, polymer surface grating couplers in SU-8 photoresist were demonstrated in Chapter 5. However, to avoid any variations due to temperature, all measurements were conducted at 23 °C. Compared to SOI materials, polymers offer strong temperature dependence with fairly high negative thermo-optic coefficients (-1 to -3×10^{-4} K^{-1} [188], silica 8.5×10^{-6} K^{-1} [189]) making them suitable for thermo-optically tunable photonic applications, especially for grating couplers which generally show a rapid decay of coupling efficiency outside the centre wavelength [190]. Tuning the centre wavelength of an air-suspended grating coupler can be required to compensate fabrication process variations for optofluidic sensors where an analyte needs to be probed at a specific wavelength in a microchannel below the grating coupler.

In this Chapter, the behaviour to temperature changes of the centre wavelength of air-suspended SU-8 waveguide grating couplers including SU-8 coating on the

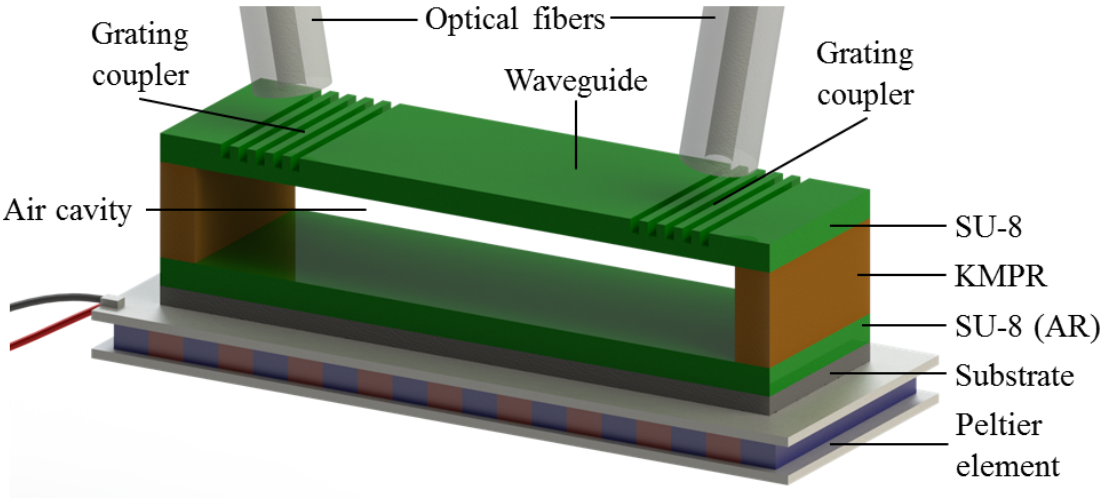

Figure 6.1: Schematic of the studied air-suspended SU-8 polymer waveguide grating couplers (cross-section, not to scale).

silicon substrate is evaluated. First, numerical simulations are carried out in order to estimate the expected wavelength shift followed by experimental evaluation.

6.2 Numerical simulation

The schematic of the structure studied in this work is shown in Fig. 6.1. It consists of an air-suspended straight polymer waveguide with a grating coupler element at each end for in- and out-coupling of light.

The grating and the waveguide structures are both realized in SU-8 on top of a previously defined KMPR microchannel which acts as the base structure and provides the bottom air cladding. An SU-8 coating on the silicon substrate is implemented as explained in Section 5.5.

When heat is applied, a shift of the spectrum of the grating coupler should occur due to thermal expansion and change of the refractive index of the material. The shift of the wavelength caused by temperature $\delta\lambda_B/\delta T$ can be described by Eq. 6.1 [191],

$$\frac{\delta\lambda_B}{\delta T} = \lambda_B \left(\frac{1}{\Lambda}\frac{\delta\Lambda}{\delta T} + \frac{1}{n}\frac{\delta n}{\delta T} \right) \tag{6.1}$$

with $(1/\Lambda)(\delta\Lambda/\delta T)$ the thermal expansion coefficient α and $(1/n)(\delta n/\delta T)$ the thermo-optic coefficient κ which causes a refractive index change due to a tem-

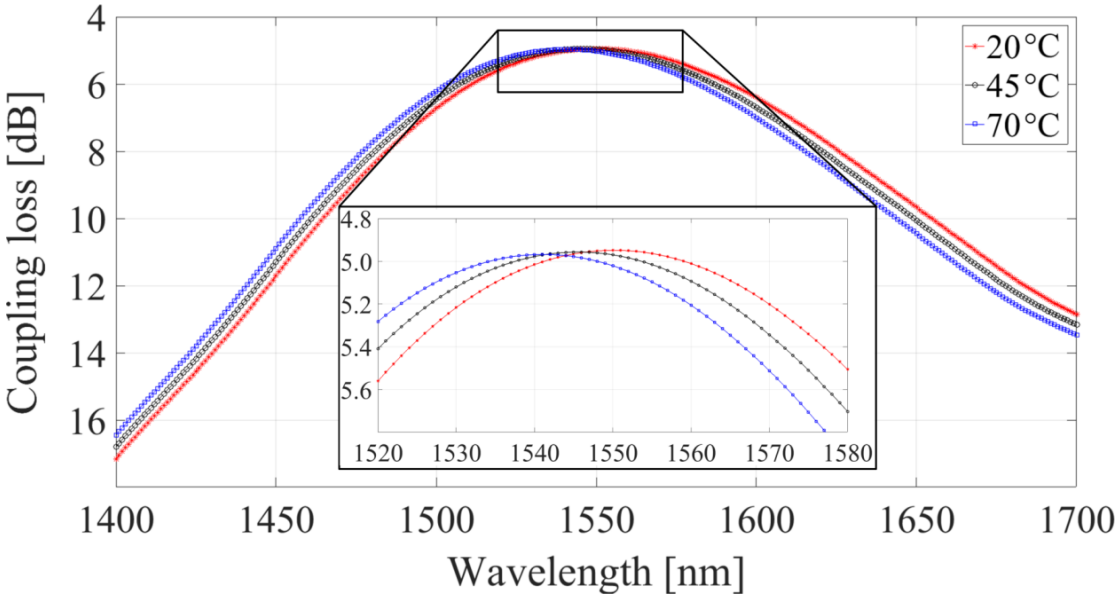

Figure 6.2: Calculated coupling loss to a single-mode optical fibre vs. wavelength for TE polarized light of a grating coupler with bottom and top air cladding at three different temperatures (20 °C, 45 °C and 70 °C). The calculated wavelength shift towards lower wavelength is approximately -0.2 nm K^{-1}.

perature change. In this work α is assumed to be 52 $\times$ 10^{-6} K^{-1} [192] and κ = -1.87 $\times$ 10^{-4} K^{-1} [193]. From the given values it can be seen that the positive α results in a shift towards longer wavelengths whereas the negative κ contributes to a shift towards shorter wavelengths.

In order to calculate the wavelength shift of SU-8 grating couplers due to a temperature change, numerical simulations are carried out using the eigenmode expansion tool CAMFR (CAvity Modelling FRamework) [166]. The centre wavelength of light used in the simulations is λ = 1550 nm with material refractive indices of n_t = 1.0 (air) and n_g = 1.575 (SU-8). The refractive index of the fibre core is 1.44 (silica). The dimensions of the grating couplers are according to Chapter 5 and are the following: thickness of the waveguide core t = 0.6 μm, groove depth of the grating e = 0.3 μm, grating period Λ = 1.397 μm and fibre coupling angle θ = 10°.

Fig. 6.2 shows the calculated coupling loss to a single-mode optical fibre vs. wavelength of an air-suspended grating coupler with the given parameters for transverse electric (TE) polarized light at three different temperatures (20 °C, 45 °C and 70 °C). The red line shows the grating coupler response of the initial parameters at 20 °C with approximately 4.9 dB coupling loss with respect to a single-mode

optical fibre at a centre wavelength of 1550 nm.

When heat is applied to the grating coupler, the thermal expansion and the thermo-optic effect are taken into account according to Eq. 6.1. Due to the higher influence of the negative thermo-optic coefficient compared to the thermal expansion coefficient of SU-8, the grating coupler response shifts towards shorter wavelengths, as can be seen in Fig. 6.2 for temperatures of 45 °C (black line) and 70 °C (blue line). The wavelength shift calculated by the numerical simulations is approximately -0.2 nm K^{-1} which is matching the expected sensitivity from Eq. 6.1.

6.3 Experimental evaluation

The spectral response of the fabricated grating couplers including an SU-8 coating on the silicon substrate has been studied using the transmission measurement setup introduced in Section 5.5. In order to investigate the behaviour to temperature changes of the grating couplers, a Peltier element (40 × 40 × 3.3 mm (length × width × height), max. 65 W power) was implemented into the test setup as it provides a fairly uniform heat distribution and can be used for heating and cooling of a sample. The Peltier element is controlled by a microcontroller in combination with a temperature sensor with an accuracy of 1 °C. The experimental transmission spectra for various temperatures for TE polarization measured with a wavelength resolution of the OSA of 0.25 nm are shown in Fig. 6.3. The black lines show the originally obtained data while the coloured lines represent data points smoothed by a moving average filter. With no heat applied (20 °C), the centre wavelength of the grating coupler (periodicity 1.46 μm, fibre angle $\theta = 10°$) is at approximately 1542 nm with approximately 11 dB coupling loss per grating coupler with respect to a single-mode optical fibre.

The expected negative wavelength shift due to the dominant thermo-optic effect with increasing the sample temperature can clearly been seen in Fig. 6.3. At the maximum temperature of 56 °C, the centre wavelength is approximately 1527 nm indicating a wavelength shift of 15 nm over 36 °C.

The centre wavelength as a function of the applied temperature is shown in Fig. 6.4 (green line). Due to the plateau-shaped measurement results, the centre wavelength was determined at the highest point of transmission from the original data with an assumed measurement uncertainty of ± 0.05 dB from the centre wavelength as shown in the inset of Fig. 6.4.

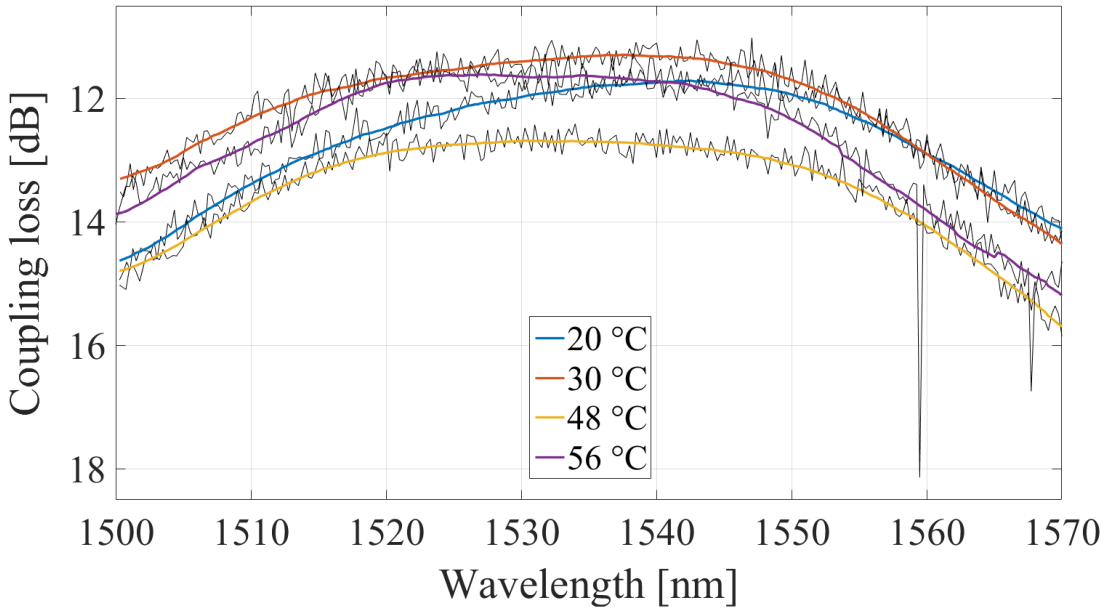

Figure 6.3: Measured coupling loss to a single-mode optical fibre vs. wavelength of fabricated air-suspended grating couplers ($\Lambda = 1.46$ μm, $\theta = 10°$) at various temperatures for TE polarization. Black coloured graphs show the original data while the coloured lines are smoothed data points using a moving average filter.

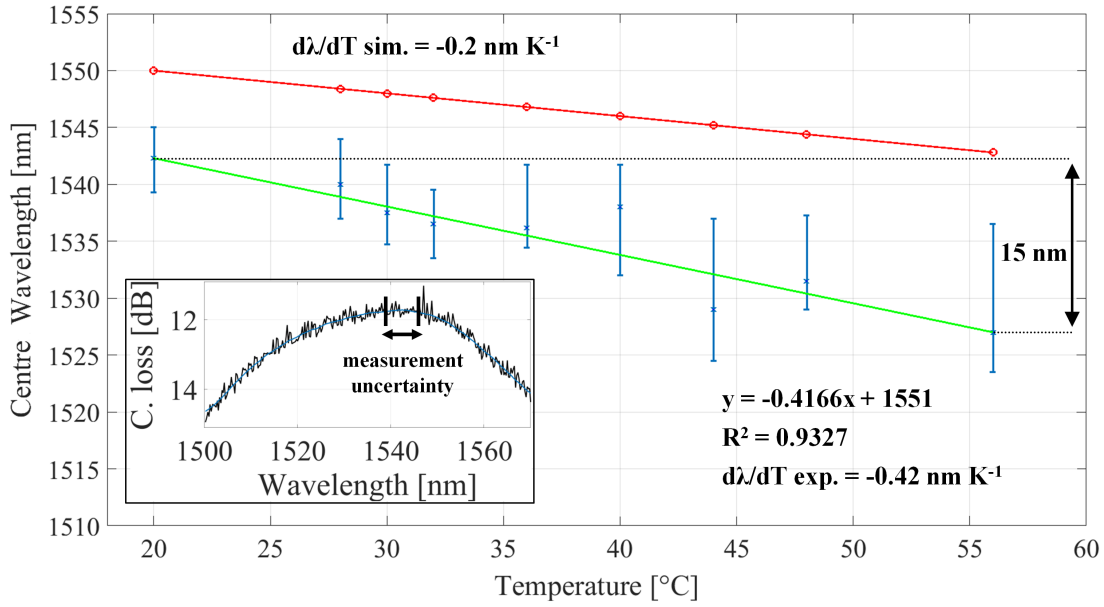

Figure 6.4: Temperature-dependent wavelength shift of air-suspended SU-8 grating couplers. The experimental results indicate a shift of -0.42 nm K^{-1} (green line) over a measurement span of 36 °C compared to -0.2 nm K^{-1} obtained by the simulation results (red line). The inset shows the determination method for the centre wavelength and the assumed measurement uncertainty.

From Fig. 6.4 it can be seen that the measurement uncertainty of the centre wavelength increases with increasing temperature. This effect is caused by vibrations of the single-mode optical fibres due to convection of the hot air above the sample to the room temperature ambient air in the laboratory resulting in deeper notches in the measurement results. From the regression line it can be seen, that the calculated wavelength shift is approximately -0.42 nm K^{-1} being slightly higher than calculated. However, due to the assumed thermal expansion and thermo-optic coefficients and the fairly high considered error in determining the centre wavelength, the simulation results match the experimental data and are in good agreement with other thermally tuned polymer gratings showing a wavelength shift of -0.36 nm K^{-1} [194] and -0.29 nm K^{-1}[195].

6.4 Conclusions

In this Chapter, the thermal sensitivity of air-suspended SU-8 surface grating couplers and waveguides including an SU-8 coating on the silicon substrate has been investigated by numerical simulations and experimental evaluation.

The numerical simulations predicted a wavelength shift in the grating coupler spectrum of approximately -0.2 nm K^{-1}. In the experiments, with no heat applied (20 °C), transmission measurements have shown that the centre wavelength of a single grating coupler is approximately 1542 nm. A tuning range of 15 nm over a temperature variation of 36 °C indicating a wavelength shift of -0.42 nm K^{-1} has been obtained. Due to the small positive thermal expansion and large negative thermo-optic coefficient of SU-8, the centre wavelength shifts towards shorter wavelengths.

However, the resulting wavelength shift caused by temperature changes is only marginally compared to the measurements of the grating couplers without the SU-8 coating on the silicon substrate which showed a relatively high sensitivity to temperature changes. It seems that for air-suspended polymer grating couplers with SU-8 coating, no additional temperature stabilisation is necessarily mandatory. However, to eliminate any temperature error, thermal stabilization is recommended.

With the knowledge and insides gained from Chapter 5 and Chapter 6, the air-cavity can be now further exploited as a microfluidic channel in combination the presented SU-8 surface grating couplers. This enables for instance integrated

optofluidic sensors, which can probe a fluidic sample. When the air-cavity is exploited as microchannel for fluids or analytes, a wide range of applications in research fields such as optofluidics, biomedical sensing and environmental analysis is opened up.

7 Optofluidic sensors based on air-suspended photonic structures

In Chapter 3 a method has been introduced to bond structured SU-8 films down to sub-micron thicknesses onto KMPR microchannels using a PDMS carrier stamp. Chapter 5 has then demonstrated how light can be coupled into such thin SU-8 layers using surface grating couplers. Based on the insights gained from Chapter 3 and Chapter 5, this Chapter exploits both methods to create highly sensitive optofluidic sensors.

A first sensor concept, which is numerically simulated and experimentally realized, is based on two surface grating couplers, whereas one grating coupler acts as input and the other coupler as output and sensing grating coupler for the test solution. This part of the Chapter is adapted from the accepted journal paper *"Optofluidic refractive index sensor based on air-suspended SU-8 grating couplers"* [196].

Two more sensitive sensor concepts are then proposed based on long-period gratings and Bragg gratings which would provide a suitable sensitivity level for novel, single-use, point-of-care biomedical diagnostic systems as proposed in the motivation of this work.

7.1 Introduction

Microfabrication in the field of fluidic and integrated photonic applications is of great interest. The term optofluidics, the combination of fluidic and optical elements, has even led to a new field of research that has attracted much interest in the last decade [197]. Combining microfluidics and integrated photonic circuits enables devices that can carry analytes in microchannels to be probed by the light or conversely, a photonic device can be modulated by a fluid. The advent of optofluidics took place at a time where polymers became a recent key technology towards mass-producible miniaturized devices due to low-cost, rapid and flexible processing. As a result, most of the recent optofluidic devices have been fabricated by soft lithography, particularly with the widely used elastomeric PDMS [56]. Furthermore, SU-8 was found to be suitable for microfluidic systems [57] and is nowadays of great popularity in the research community. The simple and easy processing of PDMS and SU-8 allow the fabrication of almost any

desired shape and structure.

In the context of sensing applications, optofluidic approaches allow the realization of an innovative class of sensors promising miniaturized, compact devices with improved sensor sensitivity and smaller sample consumption [198]. Especially in the research area of biochemical and chemical analysis, a growing interest in compact devices can be found for lab-on-a-chip (LOC) devices or micro total analysis systems (μTASs) [199, 200] as liquids can be efficiently used to transport analytes such as cells or biological molecules and optical elements can be employed to probe the samples [198]. In optofluidic devices, the microfluidic and optical parts are not really separated entities as they are merged and integrated into the same chip resulting in high interaction efficiency between light and fluids, which is very desirable for sensing applications [198].

For example, optical refractive index sensors are widely used and promise real-time results and minimal sample preparation with no fluorescent labelling required [22]. Refractive index sensors can be based on different sensing principles including surface plasmon resonance (SPR) [201], 2D photonic crystal structures [202, 203], long-period fibre grating (LPFG) [204] and various forms of waveguides and ring resonators [205–207]. However, one crucial prerequisite for the success of a technology is the sensitivity which can be directly linked to the refractive index. Commonly, such sensors are based on optical resonance so that at least a fraction of the corresponding mode is interacting with the fluidic sample. If the refractive index of the region probed by the resonant mode changes, a corresponding frequency shift of the optical resonance occurs which can then be converted into a sensing signal and be monitored [22]. For applications requiring the analysis of a liquid sample, the sensing signal can be used to determine the refractive index and then it can be compared to a reference sample. For biomolecule detection applications, the specific capture of biomolecules at the sensor surface results in a local change in refractive index, producing a sensing signal that enables quantification of the biomolecules in the sample [203, 205, 208–210]. However, in order to enable the detection of the smallest differences between liquid samples, high sensor sensitivities are required. In sensor development, sensitivity is an important parameter to evaluate the sensor performance. Increasing the sensitivity is an ever-lasting goal in chemical and biological sensor development [211, 212]. This is particularly important for label-free sensors, as a change in the properties of the fluid is directly proportional to the amount of detected biomolecules.

Therefore, increasing the sensitivity is crucial to detect such small changes. In order to achieve high sensitivities, a large overlap between the resonant mode of the light and the analyte is required [22].

However, it should be noted, that the requirement for sensitivity varies from application to application. Even though there is a rapid progress in biosensor development for various applications ranging from environmental monitoring to biotechnology, energy and food industries, clinical applications of biosensors are still rare, with glucose monitoring as an exception. This is in sharp contrast to the urgent need in small clinics and point-of-care tests. One reason for the success of the glucose monitors is that it does not require very high sensitivities for glucose detection since glucose concentration is high in blood [211, 213].

Moreover, the sensitivity is usually limited to the nanomolar range which is extremely useful for diverse applications [214–216], but in many cases it is very important to develop highly sensitive biosensors in order to meet clinical requirement of molecular diagnostics and pathogen detection requiring lower detection levels (pM-fM or single-molecule detection) [211, 217].

In the following two optofluidic refractive index sensor concepts based on the SU-8 lamination method of Chapter 3, the air-suspended waveguides of Chapter 4 and the grating coupler interfaced waveguides of Chapter 5 and 6 are presented.

The first sensor concept exploits directly air-suspended gratings and has been modelled, simulated and experimentally realized, while the second concept aims to improve the sensitivity by increasing the light-matter interaction by long-period gratings.

7.2 Refractive index sensor based on air-suspended SU-8 grating couplers

This Section presents the design, numerical simulation, fabrication and characterization of a label-free optofluidic refractive index sensor based on the air-suspended SU-8 grating couplers of Chapter 5. By exploiting the SU-8 bonding method for thin structured SU-8 films of Chapter 3, waveguide grating couplers can be fabricated in a layer on top of a microfluidic channel system. A capillary force valve, integrated into the microchannels, precisely positions the analyte, which in the experiments are different DI water based sugar solutions, below the sensing grat-

ing coupler. The main part of this Section is adapted from the published journal paper *"Optofluidic refractive index sensor based on air-suspended SU-8 grating couplers"* [196].

7.2.1 Introduction

Since the last decade, research in optofluidics has strong impact on new optical sensing concepts especially for lab-on-a-chip applications in biomedicine and biochemistry, healthcare, and drug screening [1, 218]. In addition, surface grating couplers have been extensively used as sensor elements in many different sensing configurations [219–221]. With the growing trend towards mass-producible and disposable sensing devices, polymer materials have gained great interest due to low-cost, rapid and flexible processing [222, 223].

By exploiting the microchannels available below the air-suspended grating couplers as microfluidic channels, new optofluidic sensor concepts can be realized using the SU-8 bonding method of Chapter 3 and the SU-8 grating couplers of Chapter 5.

In the following an optofluidic refractive index sensor based on air-suspended SU-8 grating couplers is proposed, simulated, fabricated, and characterised.

7.2.2 Concept and theory

The concept of the proposed microfluidic refractive index sensor consists of two grating couplers that are integrated into an air-suspended SU-8 layer on top of a microfluidic channel of KMPR. Fig. 7.1 illustrates the schematic of the sensor.

Light is coupled into the waveguide from an input grating coupler, which is suspended over air, whereas the sensing output grating coupler is completely suspended over the analyte solution. When a supported mode that is coupled into the waveguide by the input grating coupler reaches the sensing output grating coupler, the evanescent field of the mode is exposed to the analyte. According to the grating equation (Eq. 5.6, Chapter 5, Section 5.3), variations in the refractive index of the analyte change the effective refractive index of the supported mode at the grating-liquid interface. It also changes the index of the cladding into which the grating couples the radiation, resulting in a change in the outcoupling efficiency and a shift of the outcoupled spectral response, which can then be monitored.

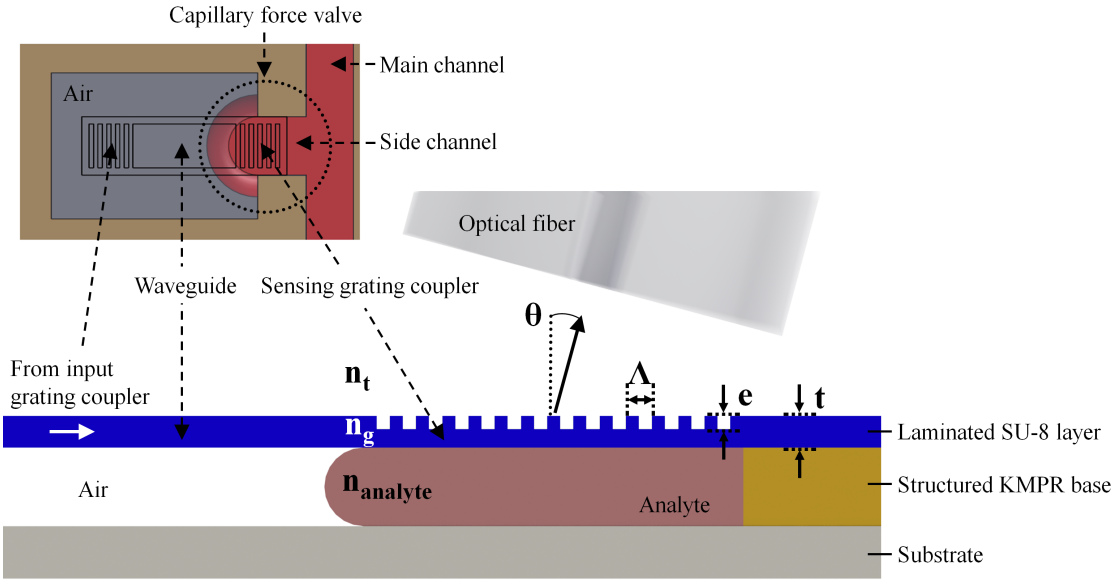

Figure 7.1: Schematic model of the proposed microfluidic refractive index sensor (not to scale). The top view (top left) illustrates the layout of the sensor, while the cross-section (bottom) gives an overview about the working principle and the individual design parameters.

In order to precisely position the analyte solution below the sensing grating coupler, a capillary force valve is employed. The capillary force valve acts as a temporary barrier for the advancing analyte and reduces the flow velocity by a local change of the microfluidic channel diameter. Due to the valve mechanism, it requires a higher pressure to move the analyte and the analyte is held back for a certain time [224]. In the design, a T-shaped microfluidic channel with a main channel and a side channel is employed, where both channels are connected by the capillary force valve as shown in the top view inset of Fig. 7.1.

7.2.3 Numerical simulation

Numerical simulations using the eigenmode expansion tool CAvity Modelling FRamework (CAMFR) [166] have been carried out in order to find the optimum dimensions of the grating coupler structures. The main design parameters are the height of the waveguide t, the groove depth of the grating e, the period Λ and the coupling angle θ as illustrated in Fig. 7.1. The wavelength of the light used in the simulations is $\lambda = 1550$ nm, the material refractive indices of SU-8 $n_g = 1.575$ [122] and of air $n_t = 1.0$. Since many analytes are based on aqueous solutions, the refractive

index of the test solution was chosen to be $n_{\text{water}} = 1.33$. The refractive index of the coupling fibre core is 1.44 (silica).

The geometrical parameters of the waveguide and the grating coupler are chosen to be within the single-mode wavelength regime in order to simplify the simulation and to achieve a well-known mode profile in the experiment. Fig. 7.2 shows the calculated coupling loss to a single-mode fibre vs. wavelength for optimized grating coupler structures over air ($n_{\text{air}} = 1.0$) and with water ($n_{\text{water}} = 1.33$) as lower cladding layer for TE polarized light at a coupling angle of $\theta = 15°$ and the following dimensional parameters: thickness of the waveguide core $t = 0.5$ μm, groove depth of the grating $e = 0.2$ μm and grating period $\Lambda = 1.34$ μm.

When water as analyte is present below the output sensing grating, it can be seen that the coupler exhibits approximately 8.87 dB coupling loss, indicating a coupling efficiency of approximately 13 % at a centre wavelength of 1586 nm (red line). If the refractive index of the analyte increases, it can be seen that the spectrum of the sensing grating coupler shifts towards longer wavelengths. Simultaneously, the intensity of the transmitted light decreases due to the higher refractive index values of the analytes. This is due to more light being coupled to the fluid filled side of the grating rather than the air side of the grating.

Fig. 7.2 (b) shows the peak wavelength of each graph vs. fluid refractive index. A linear behaviour of the shift of the centre wavelength (λ_p) can be found with increasing refractive index of the analyte. This results in a refractive index sensitivity of the sensor of 500 nm per refractive index unit (RIU). Furthermore, the intensity of the grating coupler spectrum decreases with increasing refractive index of the analyte. The decrease of the peak intensity at the individual centre wavelength behaves slightly exponential with a sensitivity of approximately 20 dB RIU^{-1}. This behaviour is represented in Fig. 7.2 (c).

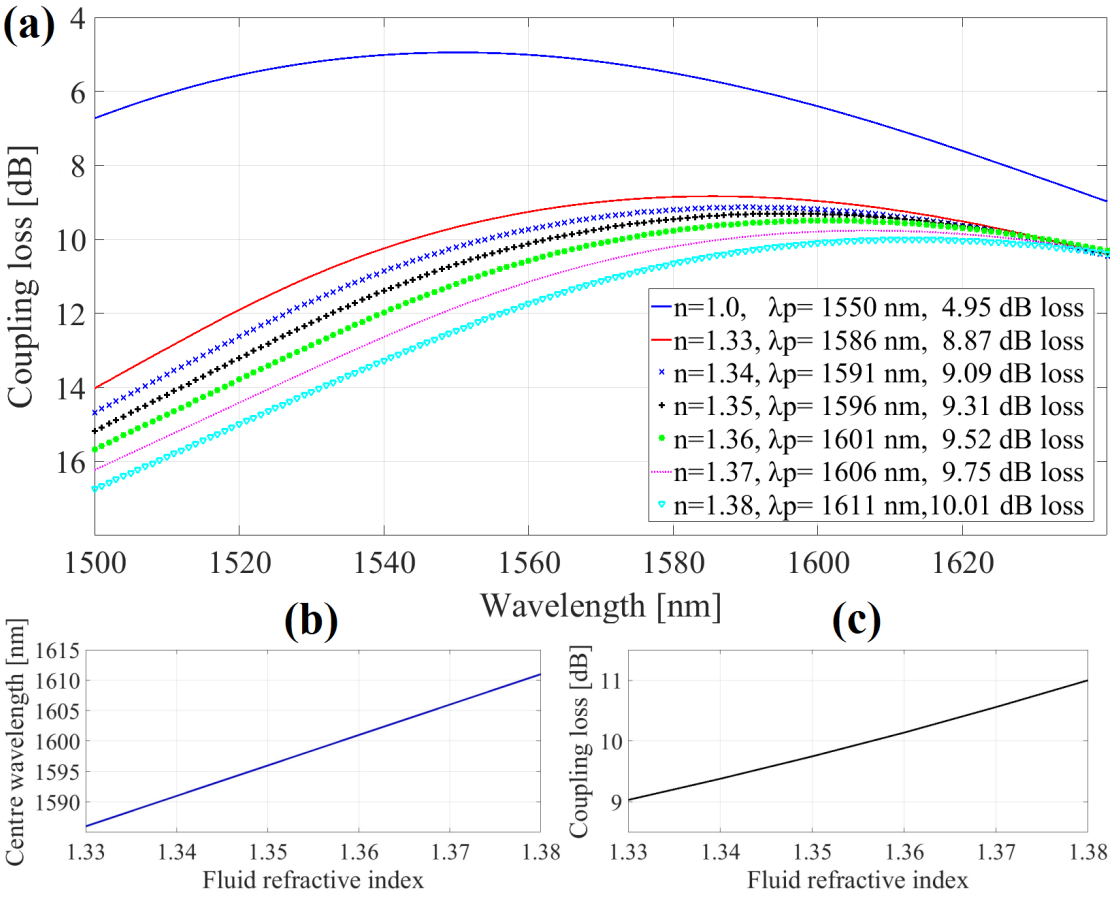

Figure 7.2: Simulation results of the microfluidic refractive index sensor. The graph in (a) shows the calculated coupling loss to a single-mode optical fibre vs. wavelength. As represented by the blue line in (b), a linear behaviour in the shift of the centre wavelength can be found with increasing refractive index of the analyte resulting in a refractive index sensitivity of the sensor of 500 nm RIU^{-1}. In addition, the intensity of the grating coupler spectrum decreases with increasing refractive index of the analyte. The decrease of the peak intensity at the individual centre wavelength behaves slightly exponential with a sensitivity of approximately 20 dB RIU^{-1} as represented by the black curve in (c).

7.2.4 Experimental demonstration

Initially, a 50 μm thick SU-8 layer has been fully processed onto a silicon wafer. As concluded from Chapter 5, Section 5.5, such layer is necessary to suppress interferences caused by the back reflected light from the silicon substrate during the measurements. Then KMPR microchannel structures and air-suspended polymer grating couplers have been fabricated on top as described in Chapter 3, Section 3.3.2 and Chapter 4, Section 5.4. Capillary force valves of different shapes have been evaluated using DI water as test solution in order to maximize the temporary barrier for the advancing liquid. Furthermore, the position of the output grating coupler has been optimized to minimize the overlap of the liquid with the waveguide. The main parameters influencing the design are the hydrophobic nature of the cured SU-8 photoresist and the surface tension of DI water.

Fig. 7.3 (a-c) presents top views of microchannel structures taken with an optical microscope at different times when DI water is flowing into the main microchannel. In the design, a 15 mm long, 200 μm wide and 25 μm high main channel and a capillary force valve with 100 $\times$ 80 $\times$ 25 μm (length $\times$ width $\times$ height) for the narrow channel part is employed, while the side channel itself is 1200 $\times$ 200 $\times$ 25 μm. When DI water is applied, the main channel is filled by capillary forces. In this experiment, no additional liquid pressure pumps have been used.

In the capillary force valve, the flow velocity of the advancing liquid is temporarily slowed down [224] and forms a lens shaped convex meniscus after approximately 5-10 min (Fig. 7.3 (c)) in the side channel that is stable up to 120 min (Fig. 7.3 (d)). This time is amply sufficient for the analyses.

From an optical point of view the convex meniscus of the water is interesting as it forms a tapered structure. This allows a smoother transition between air and the analyte and hence reduces the losses when light propagates in the waveguide structure. However, in this work the effect was not further investigated.

In the fabrication process, the grating coupler which will be exposed to the analyte can be precisely positioned over the capillary force valve in order to keep the overlap with the waveguide and hence possible losses of the guided light at a minimum. The length and width of the fabricated grating couplers are 40 μm $\times$ 40 μm with a periodicity of 1.46 μm. Due to limitations in the current fabrication process of the structures by the electron beam lithography, the depth of the grating is lower than

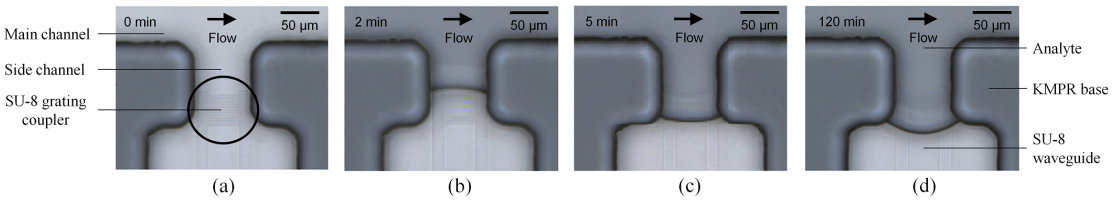

Figure 7.3: Optical micrographs of the advancing test solution meniscus inside the fabricated structures at different times (0, 2, 5 and 120 min) when DI water is applied to the main microchannel. The test solution forms a lens shaped convex meniscus after approximately 5-10 min that is stable up to 120 min directly below the sensing grating coupler.

the optimum depth calculated in the simulation and is measured with an atomic force microscope (AFM) to be 178 nm. The lengths of the waveguides used in the experiment were 0.75 and 1 mm, respectively. The height of 0.5 μm was chosen to be within the single-mode condition for 1550 nm wavelength of light, while the width is kept constant at 40 μm.

Prior to the evaluation of the sensing behaviour, DI water (electrical conductivity 0.1 μS cm^{-1} at 25 °C, Millipore DIRECT-Q3 UV, Millipore Corp.) was mixed and stirred with mass fractions between 10-50 % of conventional sugar as test solutions.

The refractive indices of the prepared test solutions have then been characterised using a refractometer (PAL-RI, Atago Co., Ltd.) at a wavelength of 589 nm at 21 °C. When a droplet of the test solution is filled into the inlet reservoir, the present capillary forces are sufficient to fill the complete main channel structure. A slight deformation of the 500 nm thick laminated SU-8 layer containing the photonic structures was observed after filling the main channel due to the compressed air inside the side channels. However, no significant influence on the measurement results has been noted.

To characterise the spectral response of the output grating coupler, a transmission measurement setup was employed as described in Section 5.5. Two identical cleaved standard single-mode fibres providing light to the input and collecting light at the output grating are connected to a tunable laser (TUNICS T100S-HP, Yenista Optics S.A) and an optical spectrum analyser (OSA, AQ6370C, Yokogawa Electric Corporation), respectively. A polarization controller is employed to launch TE polarized light into the input coupler. Both fibres are positioned at a tilted angle to the grating surface and are automatically aligned to the position

where the highest transmission occurs by scanning the grating couplers in a fine mesh grid. Further, the temperature of the sample was stabilised at 23 °C.

The experimental results taken with a wavelength resolution of the OSA of 0.25 nm are summarized in Fig. 7.4. Initially, the grating coupler response has been measured at a fibre angle of 10° without an analyte in the channels (purple line in Fig. 7.4). Then, with water applied to the microchannels, the angle of the optical fibres were optimized to 18° to obtain the grating coupler response within the measurement window of the optical spectrum analyzer. The red line in Fig. 7.4 presents the grating coupler response with its peak at around 1588 nm wavelength when pure DI water ($n = 1.3329$) is applied. It can be seen that test solutions with higher refractive indices such as $n = 1.3466$ (blue line) or $n = 1.3582$ (black line) shift the grating coupler spectrum towards longer wavelengths. This behaviour, including the reduction of the overall transmitted intensity, of analytes with higher refractive index values has been predicted in the simulations.

Due to the plateau-shaped measurement results, the centre wavelength was determined at the highest point of the transmission curves with a measurement uncertainty of ± 1 % from the highest point of the transmission, as shown in Fig. 7.4.

Fig. 7.4 (I) shows the refractive index sensitivity according to the wavelength shift being approximately 400 nm RIU^{-1}, which is in a similar range compared to the results of the numerical simulations and is comparable to published refractive index sensing devices such as planar ring resonators with 212 nm RIU^{-1} [225] or tunable grating coupler with 142 nm RIU^{-1} [226]. The discrepancy can be explained by a reduced strength of light-matter interaction in the experiment caused by fabrication imperfections of the grating structures and a slightly deviating refractive index of the SU-8 compared to the simulation.

As represented by Fig. 7.4 (II), the intensity of the grating coupler spectrum decreases with increasing refractive index of the analyte. The decrease at the individual centre wavelengths indicates a sensitivity of approximately 17 dB RIU^{-1}, which is comparable to the simulation results.

Higher refractive index values such as $n = 1.3790$ and $n = 1.3949$ have been tested as shown in Fig. 7.4; however, with the small amount of transmitted spectral response, no reliable identification of the peak wavelength could be made. Further, with increasing test cycles, the sugar solution started clogging the microchannels due to crystallization of sugar. Here, a strategy to flush and hence clean the

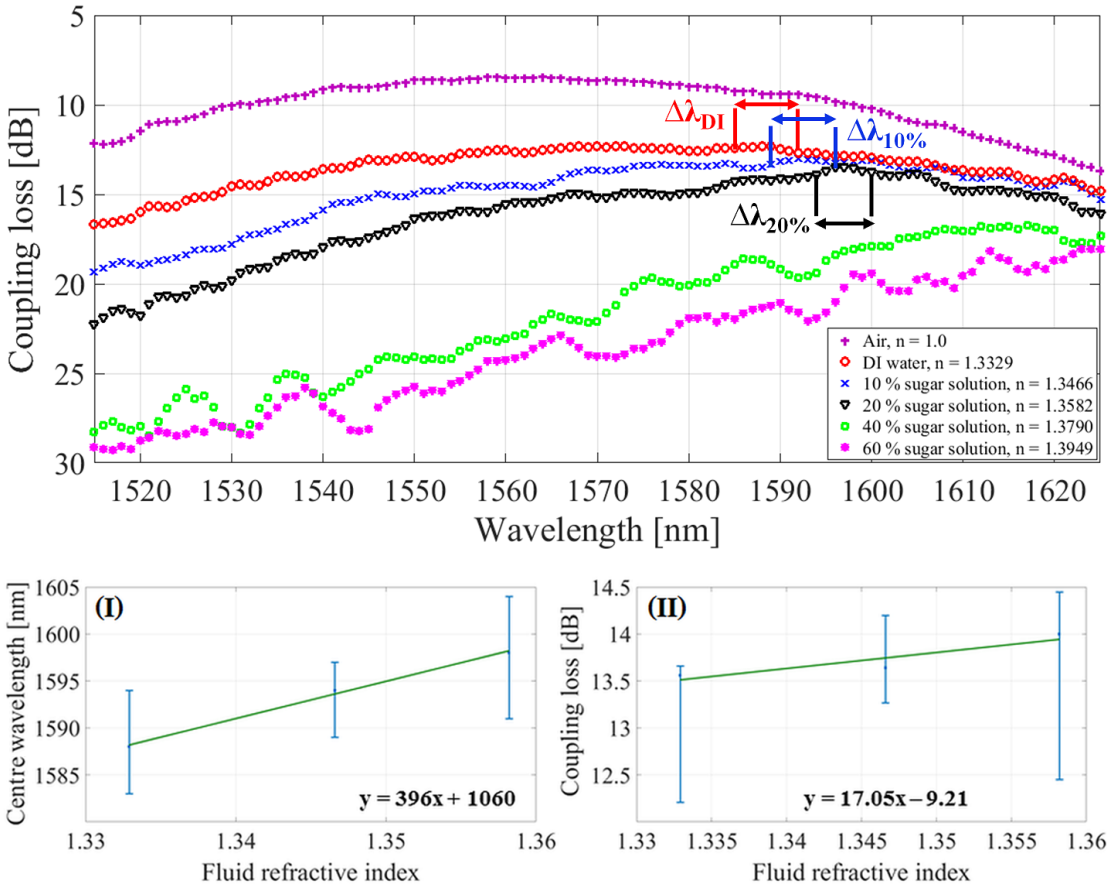

Figure 7.4: Experimental evaluation of the fabricated microfluidic refractive index sensor. Measured grating coupler spectra over air ($n = 1.0$, purple line) and of analytes with different refractive indices: $n = 1.3329$ (red line), $n = 1.3466$ (blue line) and $n = 1.3582$ (black line). Due to the plateau-shaped measurement results, the centre wavelength was determined at the highest point of the transmission curves with a measurement uncertainty of ± 1 % from the highest point of the transmission. The sensor indicates a refractive index sensitivity of approximately 400 nm RIU^{-1} with respect to the wavelength shift as shown in Fig. 7.4 (I) and 17 dB RIU^{-1} due to the intensity decrease at the individual centre wavelengths (Fig. 7.4 (II)).

microchannels after each cycle with deionized (DI) water could be utilized or other test solutions should be exploited in the future, either water based or other liquids which would then require a differently designed capillary force valve or to use stable, calibrated refractive index oils.

7.3 Refractive index sensor based on SU-8 long-period gratings

This Section presents the design and the numerical simulation of a label-free optofluidic refractive index sensor based on long-period gratings. By exploiting the SU-8 bonding method for thin and structured SU-8 films of Chapter 3 and the air-suspended SU-8 waveguide grating couplers of Chapter 4, a highly sensitive optofluidic sensor based on long-period gratings could be achieved.

7.3.1 Introduction

The refractive index sensor proposed in Section 7.2 has shown a sensitivity of about 400 nm RIU^{-1}, but with significant uncertainty in locating the resonant wavelength. Indeed, this sensor appeared to work more effectively based on the attenuation caused by the change in efficiency of the output grating. However, in order to detect even the smallest differences in analytes, higher sensitivities are required. By exploiting for example surface plasmon resonance or long-period fibre gratings, sensitivities between 3000-7000 nm RIU^{-1} have been demonstrated [204, 227, 228]. One common route to enhance the sensitivity is to increase the mode fraction or interaction length of light interacting with the analyte [22]. In order to enhance the light-matter interaction strength, numerous structures have been introduced, including cavities or resonators [229], fibres [230], surface effects [231], slow light [232], or liquid-core waveguides [233]. A promising approach are long-period grating based sensors. Long-period fibre gratings (LPFGs) are well known and are widely used in optical fibre sensors and optical communication systems. LPFGs allow the coupling of light between the guided mode and the cladding modes of an optical fibre at specific wavelengths. The wavelength and the power of the attenuation band of LPFGs are sensitive to environmental changes allowing LPFGs to be used as multi-parameter sensors for temperature [234], bend [235], strain [234], chemicals, and biological compounds [236]. Further applications include chan-

nel equalisation filtering in erbium-doped fibre amplifiers [237], band-rejection filters [238], add-drop couplers [239] and dispersion controllers [240].

Since optical fibres are limited in its materials and its round geometry, long-period waveguide gratings (LPGs) have been proposed as gratings in planar waveguides [241, 242] fabricated in various materials such as glass, lithium niobate, semiconductor, and polymers [243]. Although the light-coupling mechanism in waveguide-based LPGs and fibre LPGs are basically the same, a waveguide-based LPG offers more flexibility and optical characteristics due to the additional degrees of freedom being available in the design of optical waveguides [244].

Especially polymers are easy to process and offer many favourable properties such as large thermo-optic coefficients making them good candidates for low-cost integrated photonic applications and sensors. LPG sensors have been proposed and are nowadays popular due to the high sensitivity and wide-range tuning capabilities of LPGs [242, 243, 245, 246].

In the following and based on the knowledge gained from Chapters 3 to 6, an optofluidic refractive index sensor using air-suspended SU-8 long-period gratings is proposed and numerically simulated.

7.3.2 Concept and theory

In the concept of the proposed sensor a long-period grating (LPG) is introduced into an air-suspended SU-8 waveguide as shown in Fig. 7.5. In general, a LPG consists of a high-index partially corrugated guiding layer with lower index cladding layers. The thickness of the waveguide can be selected to support only the fundamental mode, while higher order modes are supported by the upper cladding layer. The grating in the waveguide behaves as a perturbation for the guided mode and enables coupling from the guided mode to the cladding modes. This results in a notch in the transmission spectrum of the waveguide at specific resonance wavelengths [244].

In this concept, an analyte is employed as an upper cladding layer and is simply spotted on top of the LPG. Due to the hydrophobic nature of SU-8, water based analytes form a stable droplet as illustrated in Fig. 7.5. If other analytes should be used, a microchannel structure could be considered to provide the analyte on top of the LPG. In order to couple light into the air-suspended SU-8 waveguide, the air-suspended surface waveguide grating coupler approach of Chapter 5 can

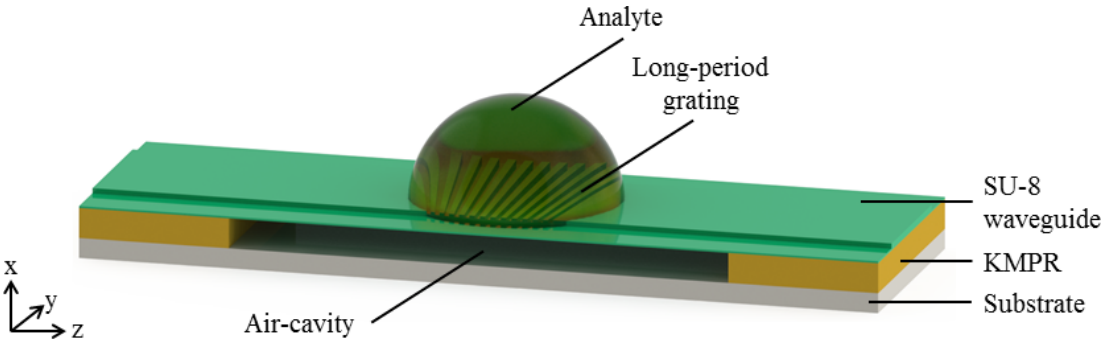

Figure 7.5: Schematic model of the proposed refractive index sensor based on SU-8 long-period gratings (not to scale). The thickness of the structure varies along the x-direction, and the width of the core varies along the y-direction, whereas the light propagates along the z-direction. When a supported mode that is coupled into the waveguide reaches the LPG, the mode is coupled into the analyte at a specific resonance wavelength producing a noticeable notch in the transmission spectrum of the waveguide. Variations in the refractive index of the analyte result in a shift of the resonance wavelength that can then be monitored.

be exploited. When a supported mode that is coupled into the waveguide reaches the LPG, the mode is coupled into the analyte at a specific resonance wavelength producing a noticeable notch in the transmission spectrum of the waveguide. Variations in the refractive index of the analytes result in a shift of the resonance wavelength that can then be monitored.

7.3.3 Numerical simulation

Numerical simulations have to be carried out to obtain a set of parameters to design the LPG to be resonant at a desired wavelength. The basic idea in the design is to determine the period and the groove depth of the corrugated grating so that a strong rejection band is developed at the desired resonance wavelength [247]. Based on the coupled mode theory [248], the period Λ and the resonance wavelength of the grating λ_{0m} can be described by the following phase-matching condition (Eq. 7.1):

$$\lambda_{0m} = \left(N_{eff}^{0} - N_{eff}^{m}\right)\Lambda \tag{7.1}$$

where N_{eff}^{0} and N_{eff}^{m} (m = 1, 2, 3,...) are the effective refractive indices of the fundamental waveguide mode and the higher order cladding modes, respectively.

For a given waveguide structure, both parameters can be calculated by using a numerical mode solver.

The strength of a LPG is mainly determined by its coupling coefficient, which can be obtained by the overlap of the transverse field distribution of the guided fundamental mode in the core of the waveguide $\psi_0(x, y)$ and that of the nominally radiating modes or resonances in the waveguide cladding modes $\psi_m(x, y)$, along with the transverse distribution of the refractive-index modulation of the grating $\Delta_n(x, y)$ [247]. Therefore, the coupling coefficient equation may be expressed as (Eq. 7.2 [247]):

$$\kappa_{0m} \propto \int\int \psi_0^*(x, y)\psi_m(x, y)\Delta_n(x, y)dxdy \tag{7.2}$$

with $\psi_0^*(x, y)$ being the complex conjugate of the core-mode transverse field distribution. The spatial distributions of these three functions depend on the characteristics of the waveguide, the cladding, and the grating. In order to calculate the overlap of the three spatial distributions, the corrugated grating structure can be either treated as a periodic perturbation in a uniform waveguide or as an average refractive index layer as shown in Fig. 7.6. An overview of the simulated structure including all employed materials and parameters is given as well as the two different methods the grating can be treated with. In the figure itself the thickness of the structure varies along the x-direction, whereas the light propagates along the z-direction.

In the case of treating the corrugation of the grating as a periodic perturbation in a uniform waveguide as shown in Fig. 7.6 (a), the bounds of integration are determined by the guiding layer thickness $t_f - \mathit{grating\ depth}/2$ and the cladding layer thickness $t_{cl} + \mathit{grating\ depth}/2$. As most analytes are water based, water was considered as analyte, respectively cladding layer.

In the case of treating the corrugation of the grating as an average refractive index layer as shown in Fig. 7.6 (b), the bounds of integration and the thickness t_{gr} of the the average refractive index layer are determined by the grating depth, where the refractive index of this layer is obtained by $n_{gr} = n_{water} + n_{SU\text{-}8}/2$.

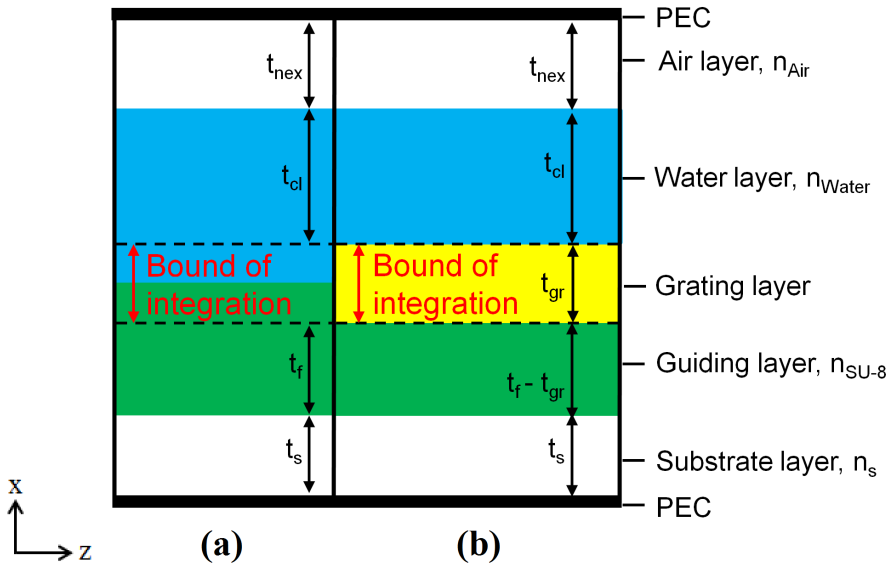

Figure 7.6: Schematic overview of the simulated LPG structure (not to scale) and two possible methods to treat the corrugated grating structure in the simulation: (a) as periodic perturbation in a uniform waveguide and (b) as an average refractive index layer. The thickness of the structure varies along the x-direction and the light propagates along the z-direction.

As the first method has been more commonly employed for LPGs, all following simulations are carried out using this technique.

To design the LPG, the eigenmode expansion tool CAMFR (CAvity Modelling FRamework) [166] is employed to first calculate the phase matching curves by Eq. 7.1 followed by the calculation of the overlap coefficient as given in Eq. 7.2. Finally, the transmission spectra of the waveguide can be plotted by using the obtained grating parameters period Λ, grating depth and grating length L with $K = \pi/2L$. In order to verify the written CAMFR code, two published LPGs have been re-simulated [241, 244]. It was found, that by using the employed simulation methods, the results of both LPGs could be obtained.

For the proof-of-concept design of the LPG, a multi-mode air-suspended SU-8 waveguide was selected. The simulation model is similar to Fig. 7.6 (a) with the parameters as given in Tab. 7.1.

Initially, a mode solver was employed to evaluate which of the higher order TE polarized modes can be coupled from the waveguide into the upper cladding/analyte layer. For the configuration proposed in Tab. 7.1 the fourth higher order TE mode is the first (cladding) mode that can be coupled to the upper cladding layer as il-

Parameter	Thickness	Refractive index
Air layer, t_{ex}	10 μm	1.0
Analyte/cladding layer (water) t_{cl}	30 μm	1.33
Guiding layer (SU-8) t_f	3.3 μm	1.575
Substrate layer (air) t_s	10 μm	1.0

Table 7.1: Simulation parameters of an multi-mode air-suspended SU-8 LPG.

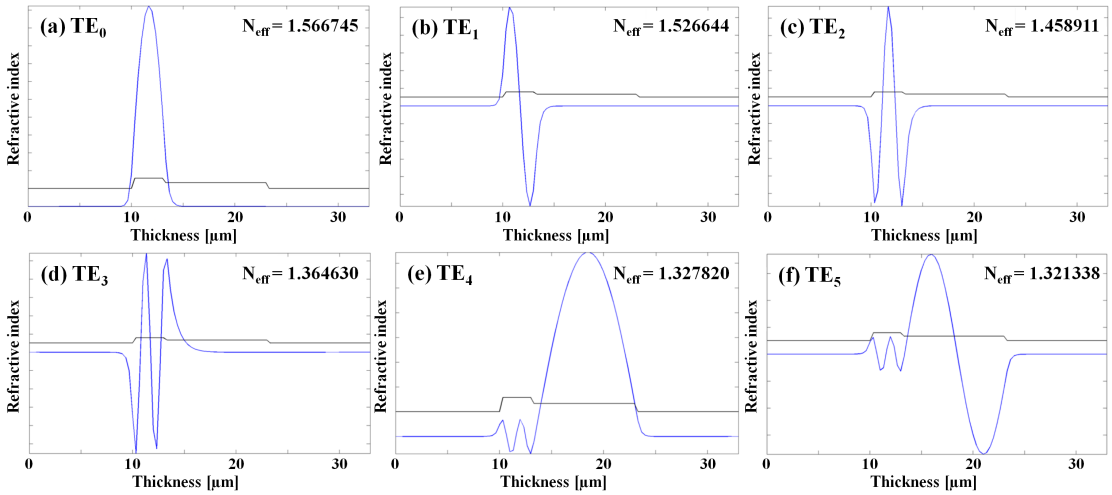

Figure 7.7: Illustration of the first six TE modes in the waveguide of the proposed LPG sensor. (a-d) show that the fundamental and the first three higher order modes (TE_0 to TE_3 (a-d)) are guided in the high index waveguide while the fourth higher order mode (TE_4 (e)) is the first mode that is guided in the upper cladding/analyte layer. The black line in each plot represents the refractive index profile of the waveguide according to Table 7.1.

lustrated in Fig 7.7. It can be seen that the fundamental and the first three higher order modes (TE_0 to TE_3 (a-d)) are guided in the high index waveguide while the fourth higher order mode (TE_4 (e)) is the first mode that is guided in the upper cladding/analyte layer. The black line in each plot represents the refractive index profile of the waveguide according to Table 7.1 (in the order from top to bottom). Then the phase matching curves have been calculated for TE polarization of light in a wavelength range between 1500 nm and 1630 nm using Eq. 7.1 to study the relationship between the resonance wavelength and the period of the LPG.

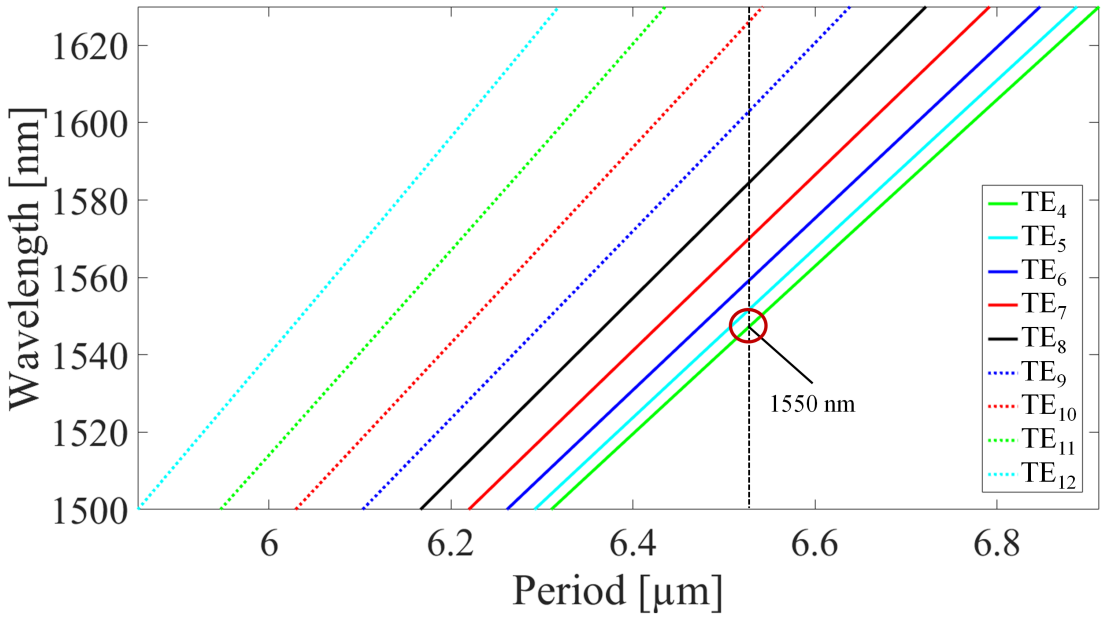

Figure 7.8: Phase matching curves of a multi-mode LPG with variations of the cladding/analyte refractive index.

Fig. 7.8 shows the resonance wavelength for various TE_m modes (m = 4 to 12) that can be coupled into the upper cladding/analyte layer. As can be seen from the figure, at a resonance wavelength of 1550 nm, the period to couple from the fundamental mode of the waveguide to the first cladding mode TE_4 is approximately 6.5 μm. At the same time, as can be seen from the dashed black line, that at this period several other higher order modes (TE_5–TE_{10}) can be coupled into the cladding layer as well. The slope of the phase-matching curves depend on the dispersion characteristics of the guided mode and the cladding mode of concern [249]. For example for fibre based LPG, it has been shown that this parameter governs the sensitivity of the resonance wavelength to any physical parameter, which can be an environmental parameter, such as temperature, strain, pressure or surrounding refractive index [250].

In the next step, the coupling coefficients K are calculated by overlap integrals according to Eq. 7.2 using CAMFR to determine the depth and length of the grating. Fig. 7.9 shows the dependence of the coupling coefficients of the $TE_0 \rightarrow TE_4$ coupling on the grating depth. From the graph in Fig. 7.9 a suitable grating depth can be chosen according to the waveguide thickness. By using the equation $K = \pi/2L$, the grating length L can be calculated. Generally, deeper corrugation or grating depths are preferable to make strong gratings, and hence a high cou-

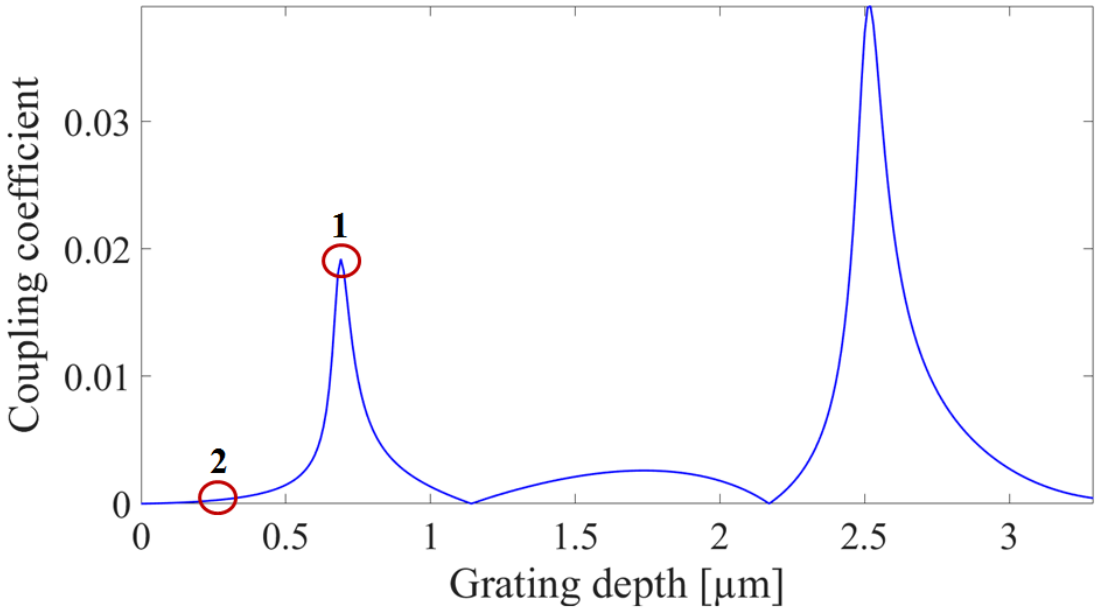

Figure 7.9: Dependence of the coupling coefficients of the $TE_0 \rightarrow TE_4$ coupling on the grating depth.

pling coefficient as marked in the figure with the red circle (1), the peak of the half of the first oscillation. However, due to the constrains with the current fabrication capabilities, a weaker grating depth of 0.2 μm as marked in the figure with the red circle (2) has been chosen for further simulations, resulting in a grating length of approximately 10 mm, which is in the range of similar LPGs with grating lengths of several centimetres [235, 238]. With the calculation of the grating period using the phase matching curves, the grating depth and length have been obtained by the coupling coefficient calculation describing all required parameters for a 2D LPG.

In the final step, the grating structure is drawn in CAMFR and the transmission for a specific wavelength range trough the LPG can be simulated.

The black solid line in Fig. 7.10 shows the transmission spectra for TE polarized light of a multi-mode LPG with a grating period of 6.5 μm, a grating depth of 0.2 μm, and a grating length of approximately 10 mm while having water ($n = 1.33$) as upper cladding/analyte layer. The resolution employed in this simulation is 100 pm. As can be seen in Fig. 7.10, the first notch in the transmission spectra occurs at around 1550 nm as selected from the phase matching curve in Fig. 7.8 when light is coupled to the first cladding mode TE_4. As can be seen, all other higher order modes that can couple ($TE_5 - TE_{10}$) also produce a notch at

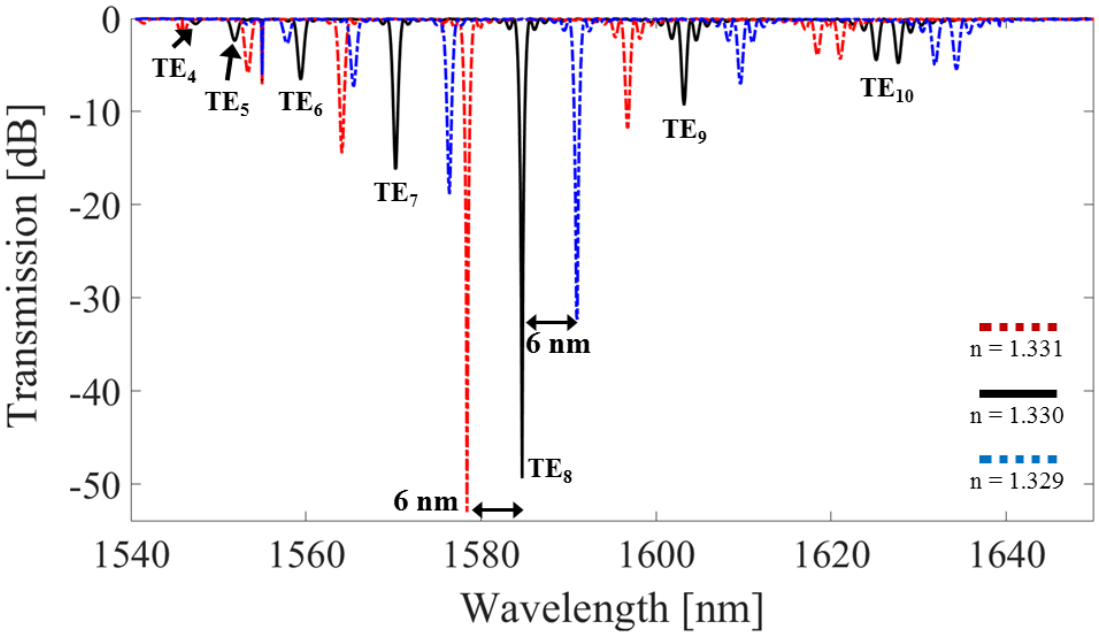

Figure 7.10: Transmission spectra for TE polarized light of a multi-mode LPG with a grating period of 6.5 μm, a grating depth of 0.2 μm, and a grating length of approximately 10 mm.

their specific resonance wavelength.

If the refractive index of the cladding/analyte layer is slightly varied, for example by $\pm$ 0.001 all notches of the transmission spectra shift consistently towards shorter wavelength when the refractive index is increased (red dashed line) while slightly lower refractive indices produce a shift towards longer wavelengths (blue dashed line). As can be seen, a change in the refractive index of 0.001 results in a shift of the resonance wavelengths in the order of 6 nm, indicating a very high refractive index sensitivity of 6000 nm RIU^{-1} of the proposed LPG sensor.

It should be noted, that for a realization of this proposed sensor structure, a cross-flow microfluidic channel to precisely control the liquid on top of the grating area might be more practical instead of placing a droplet. Furthermore, it has to be considered, that by using such small gratings, air could be trapped in between the corrugated structures.

7.4 Future work – Bragg guided optofluidic sensor

As mentioned in the introduction of this Section, increasing the mode fraction of light that interacts with the analyte is a common route to enhance the sensitivity of optofluidic sensors. In the previous Section, Section 7.3, a planar long-period grating based refractive index sensor was introduced that can couple light into the analyte and hence can achieve a high sensitivity.

A second promising approach is to confine light in a low refractive index material such as an analyte by surrounding the material with a high-index dielectric periodic structure. This periodic structure is designed in a way that the cladding layer(s) function as highly efficient mirrors at one or more wavelengths so that the optical confinement relies on constructive interference of multiple reflections at the boundaries of the periodic structure. This principle works over a wide range of layers, from devices using only one or a few cladding layers such as anti-resonant reflecting optical waveguides (ARROW) [251] to extended periodic structures such as Bragg waveguides. Bragg photonic band gap guidance has been demonstrated in hollow core photonic fibres [252] as well as in hollow core Bragg fibres made of tellurium and polymer [253] and for integrated waveguides with silica cores [254]. Also fibre-based platforms based on periodicity have been realised with aqueous fluid-infiltrated cores in structured photonic crystal fibres [255], hollow polymer fibres [256] and infiltrated Bragg fibres [257].

Planar polymer optofluidic Bragg photonic band gap guided platforms have so far only been reported by E. Zeller who theoretically and numerically investigated different novel concepts in his Ph.D. thesis (RMIT University, 2014 [258]). Zeller showed in 2D simulation, that refractive index sensitivities up to 3000 nm RIU^{-1} could be achieved.

Fig. 7.11 shows one of the proposed refractive index sensing platforms. It consists of a structured and laminated air-suspended SU-8 waveguide layer on top of a KMPR base structure. The SU-8 layer combines two different waveguide mechanisms. First, in order to increase the overlap between light and analyte and to confine the light in the vertical (x) direction, reverse symmetry waveguides are exploited. In contrast to conventional waveguides, the refractive index of the lower cladding layer is usually higher than the refractive index of the upper cladding layer while in a reverse symmetry waveguide the upper cladding layer has a higher refractive index than the lower cladding [259]. Here, the evanescent tail of the

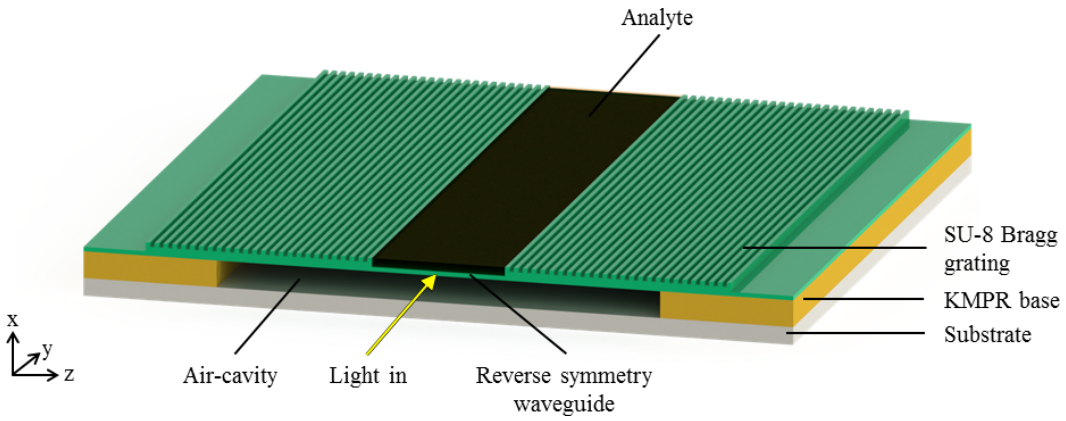

Figure 7.11: Concept of a highly sensitive refractive index sensing platform based on a reverse symmetry waveguide to confine light in the vertical direction and a high-index periodic Bragg grating to confine the light in the horizontal direction. The proposed refractive index sensitivity is up to 3000 nm RIU^{-1}.

guided light will be forced into the upper cladding layer (the analyte), as the lower cladding layer consists of an air cavity and exhibits a lower refractive index. In this concept, light will be guided along the y-direction and can e.g. be coupled into the reverse symmetry waveguide by butt-coupling at the end-facet, while the analyte itself is only located on top of this waveguide type as shown in Fig. 7.11.

Secondly, to confine the light in the analyte and in the horizontal (z) direction, the analyte is surrounded by high-index dielectric periodic Bragg gratings as can be seen in the figure. By employing this two guiding mechanisms, three different sensing platforms have been investigated in 2D simulations by Zeller [258]. The proposed sensor structures exhibit an excellent overlap between light and analyte resulting in refractive index sensitivities up to 3000 nm RIU^{-1}. However, in order to be able to fabricate such optofluidic sensors, additional 2D and 3D simulations would be required to further study the behaviour of the sensors and to obtain parameters for the fabrication.

To enable the fabrication, the presented lamination method of Chapter 3 can be exploited by either directly patterning the sensor structures or by a combination of a flat laminated layer and a subsequently lithographically defined Bragg grating depending on the geometry of the sensor structure. Light coupling into and out of the devices can be realized for example by the proposed air-suspended grating coupler presented in Chapter 5 which are advantageous as they can be placed everywhere in the sample making the design of the analyte channel easier.

7.5 Conclusions

In this Chapter three different optofluidic sensor concepts have been proposed based on the SU-8 bonding method shown in Chapter 3. In order to couple light into these sensors, the air-suspended SU-8 grating couplers proposed in Chapter 5 have been employed.

The first sensor concept has been fully numerically simulated, experimentally realized and characterised. By exploiting the SU-8 lamination method for thin and structured SU-8 films, waveguide grating couplers are fabricated in a film on top of a microfluidic channel system. A capillary force valve, integrated into the microchannels, precisely positions the employed test analytes, which are different DI water based sugar solutions, below the sensing grating coupler. Numerical simulations have been carried out in order to estimate the expected sensitivity of the refractive index sensor and to obtain a set of parameters for the fabrication process. The sensing grating coupler is optimized for a maximum spectral response at 1550 nm wavelength when regular DI water ($n = 1.33$) is applied to the microfluidic channel. When the guided mode of the waveguide reaches the sensing grating region, it is exposed to the analyte resulting in a change of the effective refractive index of the mode. Transmission measurements have shown a linear behaviour in the shift of the centre wavelength of the sensing grating coupler response with increasing refractive index of the analyte resulting in a refractive index sensitivity of the sensor of 400 nm RIU^{-1}. Additionally, the intensity of the grating coupler spectrum decreases with increasing refractive index of the analyte indicating a sensitivity to the decrease of 17 dB RIU^{-1}, which is similar to the results of the numerical simulations.

One drawback of the sugar based test solutions is, that after a few test runs the microchannels start to clog due to crystallization of sugar. For future applications based on this approach, flushing the channels with DI water might be a useful option when the test solutions show this behaviour or to use stable, calibrated refractive index oils. Another issue that should be always considered for test solutions other than based on water, is that a differently designed capillary force valve will be required. An advantage of having an analyte below the sensing grating coupler is, that no extra coating on the silicon subtrate to suppress the substrate resonance is necessarily needed as explained in, Section 5.5 due to the higher refractive index of the analyte.

A major advantage of the presented optofluidic sensor concept is that in comparison to previously shown sensing applications using grating coupler structures, the analytes can directly be probed in-line in a microfluidic channel due to the combination of a microfluidic channel and air-suspended grating couplers. This makes the proposed sensor concept highly suitable for in-line polymer optofluidics and low-cost optofluidic and photonics sensor concepts in the fields of biochemical processes (e.g. differences in glucose concentrations in an aqueous solution), medicine or food industry (e.g. silicone oil) or environmental sensing. In addition, as the capillary force valve can in principle be optimized for various types of liquids, the presented sensor is not only restricted to water-based analytes. However, in order to detect even the smallest differences in analytes, higher sensitivities are required.

As the first proposed optofluidic sensor achieved a decent refractive index sensitivity of approximately 400 nm RIU^{-1}, the second sensor concept aimed to increase the sensitivity by introducing a long-period grating (LPG) into an air-suspended SU-8 waveguide in order to enhance the light-matter interaction strength. When a supported mode that is coupled into the waveguide reaches the LPG, the mode is coupled into the analyte at a specific resonance wavelength producing a noticeable notch in the transmission spectrum of the waveguide. Variations in the refractive index of the analytes result in a shift of the resonance wavelength which can then be monitored. Numerical phase matching curve calculations have been carried out to obtain the grating period for TE polarized light at a resonance wavelength of 1550 nm for an LPG with a multi-mode waveguide. By calculating the coupling coefficients using overlap integrals of the fundamental core mode in the waveguide and the cladding modes, the parameters of the 2D LPG sensor have been fully described. Transmission calculations versus the wavelength have shown that the proof-of-concept design exhibits a very high refractive index sensitivity of 6000 nm RIU^{-1}, which is comparable with other LPG sensors [204].

However, in order to be able to fabricate such optofluidic sensors, additional 3D simulations would be required to further study the behaviour of the sensor design and to obtain information for the width of the LPG. On the other hand, different waveguide and grating widths could directly be fabricated and tested. For the fabrication the proposed SU-8 bonding method described in Chapter 3 can be employed. Air-suspended LPG are not necessarily required for an entirely polymer-based sensor; however, the light coupling using air-suspended grating coupler has been shown as a suitable light coupling method in Chapter 5. Another param-

eter that should be considered in further simulations is the waveguide thickness and the grating depth, as with both parameters light coupling in and out of the waveguide as well as coupling with the LPG should be feasible. If such structures can be experimentally realized, arrays of sensor structures could be fabricated in parallel, enabling multi-parameter optofluidic sensors with high refractive index sensitivities.

The third presented concept described in Section 7.4 was originally proposed in the Ph.D. thesis of Zeller [258] and employs reverse symmetry waveguide to confine guided light horizontally and Bragg gratings to confine the light vertically in an analyte. Such sensors can achieve refractive index sensitivities up to 3000 nm RIU^{-1}. However, in order to enable the fabrication and hence the experimental realization in the future, the proposed SU-8 bonding and air-suspended grating coupling methods demonstrated in this thesis are required.

8 Conclusions and future work

This Chapter summarizes and concludes the presented work and gives an outlook and recommendations for future research.

8.1 Conclusions

The focus of this thesis was to work towards highly sensitive, miniaturized, integrated optofluidic sensors that could possibly replace bulky and stationary medical diagnostic devices in the future. The growing trend towards mass-producible and low-cost sensing devices makes polymer materials an interesting candidate for single-use, miniaturized systems which would allow for example local point-of-care measurements in medical offices or ambulances. Enabling such devices would enhance the accessibility of such tests and would allow an earlier diagnosis of the symptoms of a patient and hence increase the potential for a successful therapy.

In the progress of downscaling polymer integrated optofluidic devices, it is important to provide a high refractive index contrast to enable strong light confinement in the waveguide of the sensor and therefore the capability of reducing device proportions. However, due to the low refractive index contrast available between various polymer materials, the efficiency of such devices is often limited.

A method to increase the refractive index contrast for polymer photonic and optofluidic devices has been explored and described in Chapter 3. By bonding unstructured and structured SU-8 films down to sub-micron thicknesses onto microchannels fabricated in KMPR using a flexible PDMS carrier stamp, it is possible to create air-suspended SU-8 layers with the highest possible refractive index contrast. To the best knowledge, this is the first experimental realization of the bonding of structured and unstructured SU-8 films below 1 μm of thickness. Such bonded layers could be patterned for example for optical structures and could be bonded down to a thickness of 0.5 μm, which in principal allows to guide light in the single-mode regime for infrared light. Most importantly, the combination of possible fluid handling in the microchannels and photonic structures realized in the laminated SU-8 layer enables research towards a large range of applications in microfluidics, optics and optofluidics.

However, in order to exploit this approach for optical and optofluidic sensing applications, light needs to be coupled and launched into the thin air-suspended SU-8 layers. In Chapter 4 light coupling into bonded SU-8 layers was demonstrated using air-suspended SU-8 rib waveguides and butt coupling. First, single-mode rib waveguides have been numerically simulated. Then, by exploiting the bonding method to seal air cavities of KMPR with a thin SU-8 film by using a flexible PDMS carrier stamp, combined with a subsequent photolithography step to define a rib structure, air-suspended rib waveguides have been fabricated. Although single-mode guidance of light in an air-suspended SU-8 waveguide was demonstrated in the experiment, end facet demonstration damages the fluidic channel underneath for the end-facet preparation, limiting the usefulness for optofluidic devices. Furthermore, defining the optical structure by photolithography adds an extra step to the process.

More promising are SU-8 surface grating couplers which have been investigated in Chapter 5. In a proof-of-concept design two grating couplers are connected by a waveguide with single-mode condition in the vertical dimension. The numerical simulations that have been carried out demonstrated a maximum coupling loss of 4.9 dB, indicating a coupling efficiency of approximately 32 % at a maximum spectral response of 1550 nm. The first experimental transmission measurements have shown, that the configuration of the fabricated grating couplers exhibited oscillating spectral responses suggesting multi-path interference. In order to suppress this behaviour, an SU-8 coating on the silicon substrate, approximately 50 μm thick, was introduced and it was demonstrated that this layer suppressed the observed oscillations. These measurements have then shown that a single grating coupler exhibits approximately 8 dB coupling loss at a centre wavelength of 1557 nm, indicating a coupling efficiency of 16 %. Even though the achieved coupling efficiencies are lower than for SOI couplers, mainly due to current fabrication limits of the master structures, the fabrication method employing widely used polymer materials has the advantage that multiple air-suspended structures can directly be created in only one simple lamination process without the need of additional etching steps making this parallel fabrication technique highly applicable for low-cost mass production of polymer photonic and optofluidic devices.

Furthermore, it was observed that the spectra of the polymer grating couplers without SU-8 coating on the silicon substrate are very sensitive to temperature changes. Measurements have shown a huge shift of the centre wavelength of ap-

proximately -15 nm K^{-1}. As a consequence, the thermal sensitivity of polymer grating couplers with SU-8 coating have been numerically studied and evaluated in Chapter 6. The measurements have shown a tuning range of 15 nm over a temperature variation of 36 °C, indicating a wavelength shift of only -0.42 nm K^{-1}. Thus, the resulting wavelength shift caused by temperature changes is only marginally compared to the measurements of the grating couplers without the SU-8 coating which showed a relatively high sensitivity to temperature changes. It seems that for air-suspended polymer grating couplers with SU-8 coating, no additional temperature stabilisation is necessarily mandatory.

Finally, in Chapter 7 different optofluidic refractive index sensor concepts have been proposed based on the SU-8 bonding method shown in Chapter 3 and air-suspended SU-8 grating couplers proposed in Chapter 5. Matching the simulation results, the experimental characterization of the first sensor structure demonstrates a refractive index sensitivity of approximately 400 nm RIU^{-1} according to the wavelength shift of the grating coupler response, and 17 dB RIU^{-1} due to the intensity loss for refractive index variations between $n = 1.33$ and $n = 1.36$. In comparison to previously shown sensing applications using grating coupler structures, the analytes can directly be probed in-line in a microfluidic channel due to the combination of a microfluidic channel and air-suspended grating couplers making the proposed sensor concept highly suitable for in-line polymer optofluidics and low-cost optofluidic and photonics sensor concepts.

However, in order to detect even the smallest differences in analytes, higher sensitivities are required. As the first proposed optofluidic sensor achieved an adequate refractive index sensitivity of approximately 400 nm RIU^{-1} the second sensor concept aimed to increase the sensitivity by introducing a long-period grating (LPG) into an air-suspended SU-8 waveguide in order to enhance the light-matter interaction strength. Numerical simulations have been carried out to obtain a set of parameters for a multi-mode LPG for TE polarized light and a resonance wavelength of 1550 nm. Transmission calculations as a function of wavelength have shown that the sensors exhibit a very high refractive index sensitivity of 6000 nm RIU^{-1}, which is comparable and in the range of other LPG sensors (Tab. 8.1). However, in order to be able to fabricate such optofluidic sensors, additional 3D simulations would be required to further study the behaviour of the sensors and to obtain information of the width of the LPG.

Sensor configuration	Sensitivity
Surface plasmon polaritons (SPPs) [260]	30000 nm RIU^{-1}
SPR (metal-film coupled) [261]	7500 nm RIU^{-1}
Long period grating (LPG), Ch. 7, Sec. 7.3	**6000 nm RIU^{-1}**
SPR (grating coupled) [262]	3365 nm RIU^{-1}
Bragg guided optofluidic sensor, Ch. 7, Sec. 7.4	**3000 nm RIU^{-1}**
SPR (Bragg fiber) [263]	3000 nm RIU^{-1}
LPFG [264]	2500 nm RIU^{-1}
Liquid ring resonator [265]	800 nm RIU^{-1}
Ring-disk nanocavities [266]	648 nm RIU^{-1}
Nanoprisms [267]	583 nm RIU^{-1}
Air-suspended grating coupler, Ch. 7, Sec. 7.2	**400 nm RIU^{-1}**
Localized SPR [268]	300 nm RIU^{-1}
Planar ring resonator [225]	212 nm RIU^{-1}
Tunable grating coupler [226]	142 nm RIU^{-1}
Microsphere ring resonator [269]	30 nm RIU^{-1}

Table 8.1: Examples of demonstrated refractive index sensitivities for various sensing technologies and comparison to the refractive index sensors presented in this work (highlighted in bold).

Linking the achieved refractive index sensitivities with real world applications is in fact difficult, as the requirement for sensitivity varies from case to case and most publications only report the achieved sensitivity and propose possible applications, mainly for biological and chemical sensing. An overview of sensitivities and a comparison of various types of optical biosensors can be found here [172, 212, 270]. However, mostly the sensitivity for different technology platforms is declared in units of Mol or gram per liter depending on the analyte to be detected which can range from proteins, DNA, urine, whole blood or serum to bacteria or cells. In order to classify and compare the sensors proposed and demonstrated in this work, sensitivities in units of nm per refractive index unit are required.

Table 8.1 presents an overview of refractive index sensitivities for various demonstrated sensing technologies compared to the refractive index sensors presented in this work. The sensitivity of the air-suspended grating couplers demonstrated in Chapter 7, Section 7.2 is with 400 nm RIU^{-1} in good agreement with other resonant structures such as ring resonators or grating couplers. The Bragg guided optofluidic sensor proposed in Chapter 7, Section 7.4 provides a high sensitivity of

3000 nm RIU^{-1} which is comparable with grating coupled SPR sensors and LPFGs. The long period grating shown in Chapter 7, Section 7.3 is with a sensitivity of 6000 nm RIU^{-1} within the range of highly sensitive SPR sensors.

SPR sensors are the most widely employed optical biosensor since its first description in 1983 [271]. Most of the commercially available at present use surface plasmon polaritons (SPPs) [260] and an outstanding ability to analyze biological interactions has been demonstrated. The exceptionally high number of publications in plasmonic biosensors is a proof of the profound impact of SPRs, with many and diverse configurations in applications that range from biotechnology, chemistry to environmental monitoring and food industries [267].

However, SPR sensor still suffers from an intrinsic limited sensitivity which is not enough for relevant clinical and environmental applications [217]. New concepts, for example, SPPs based on metamaterial of porous nanorod layers can potentially achieve extreme sensitivities of 30000 nm RIU^{-1} for detection and studies of binding events of analytes and receptors [260].

Even though the presented long period grating sensor in Chapter 7, Section 7.3 is highly sensitive to changes in the refractive index of a liquid and has a sensitivity comparable to SPR-based sensors, more investigations in working principles and technological approaches have to be carried out in order to realize relevant clinical and environmental applications in the future.

In summary, this work has proposed a new polymer lamination method that enables efficient light coupling into air-suspended polymer waveguides by optical grating couplers which then can be exploited for research towards a large range of applications in the field of microfluidics, optics and optofluidics, especially towards highly sensitive integrated optofluidic sensors as it has been demonstrated in this work.

8.2 Outlook

The methods and scientific insight presented in this thesis offer several opportunities for future research projects.

The insights gained in Chapter 3 enable bonding of unstructured and structured films of the epoxy-based, negative photoresist SU-8 down to a thickness of 0.5 μm onto microchannels fabricated in the epoxy-based negative photoresist KMPR us-

ing a flexible PDMS carrier stamp. Future work on the proposed bonding method could gather new insights, especially for microfluidics, when other material combinations would be employed. Other epoxy-based photoresists might be interesting for applications with certain surface property requirements on the microchannels. However, bonding of structured polymer photonic films onto silicon or glass would enable more complex optofluidic structures and applications including the advantages that both materials offer, such as high chemical resistance, solvent compatibility, mechanical strength, surface and temperature stability, high aspect ratio or high accuracy on large footprints.

Since air-suspended polymer photonic structures such as surface grating couplers have been demonstrated as a proof-of concept for infrared light in Chapter 5, future work could aim to transfer the gained knowledge to visible wavelengths as this range is widely used in biomedical and chemical analysis. However, this would require even thinner laminated layers due to the shorter wavelengths. New insights could be gathered by investigating the limits in thickness of such thin films. Another approach to achieve such thin films could be to underexpose the SU-8 film and only cross-link the upper part of the layer. The unexposed part could then be removed using developer.

In order to improve the performance of the demonstrated air-suspended SU-8 grating couplers that have been proposed in Chapter 5, significant changes of the design could be made in the future. First, a high-quality anti-reflection layer could be coated onto the silicon substrate to suppress interferences caused by the air-cavity. One possible method to improve the coupling efficiency is to reduce the grating coupler width to minimize the mode mismatch of the diffracted field of the output grating coupler and the spot size of the output single-mode optical fibre. Tapering the waveguide down to single-mode conditions in the horizontal dimension would enhance this behaviour as well. Another significant improvement towards higher coupling efficiencies would be to employ curved grating couplers to focus the light towards the output fibre. Furthermore, since the waveguide between the two grating couplers can act as a multi-mode interferometer, after a certain distance, all of the modes will accumulate multiples of 2 π phase shift and will form an image of the input fibre spot. This would be the optimal situation for minimal coupling loss in the system and should be studied in the future.

The obvious next research goal will be continuing the work on the proposed highly sensitive refractive index sensors of Chapter 7. Regarding the sensor based on long-period gratings, 3D simulations would be required to obtain the width of the structures. Alternatively, different waveguide and grating widths could directly be fabricated and tested with testing solutions with different refractive indices. When the waveguide dimensions have to be within the single-mode range, the width is limited to several hundreds of nanometres. For the fabrication the proposed SU-8 bonding method described in Chapter 3 could be employed, combined with the air-suspended grating couplers shown in Chapter 5.

The second highly sensitive refractive index sensor described in Section 7.4, which employs a reverse symmetry waveguide to confine guided light horizontally and a Bragg grating to confine the light vertically in an analyte, needs further simulations to enable the fabrication and hence the experimental realization in the future. Currently, Prof. Majid Ebnali-Heidari, a specialist in the simulation of optical structures from Shahrekord University in Iran, is performing simulations in order to provide parameters for the fabrication. Once the simulations are finished, a master can be designed and fabricated. With the insights achieved in this thesis, the fabrication and characterisation of the sensors should be more or less straightforward.

A more technological progress could be made by semi-automating the SU-8 bonding procedure using the EVG 620 mask aligner. Currently, only a software restriction prohibits the lamination of SU-8 layers as the PDMS carrier stamp with the applied uncross-linked SU-8 layer is always getting in contact with the KMPR microchannel by using the EVG 620 mask aligner. First, the process of the machine requires a wedge compensation of the employed tooling. The wedge compensation could be avoided in a second step by using a dummy substrate; however, the alignment distance of the machine is always acquired by touching the substrate, followed by moving the tooling in the separation distance set in the software. This procedure would destroy the uncross-linked SU-8 layer during the alignment procedure of the machine. However, re-writing the software seems to be straightforward as well as the design of new tooling such as holders, heating elements and precise pressure transducers which would be required for a semi-automated SU-8 bonding process. Realizing such technology in a high-level mask aligner would pave the way towards a more precise and better controlled bonding process and would allow automation and mass-production of the technology and applications

presented in this work. However, in terms of mass-production it should be noted, that even though microfluidics and optofluidics offer great possibilities for research and have advantages over many technologies, no significant commercial players is exploiting it as presently such devices will not generate much profit. One aspect that might be correlated is, that in comparison to e.g. complementary metal-oxide-semiconductors (CMOS) and microelectromechanical systems (MEMS), microfluidics and optofluidics is not that easily scalable for mass-production.

References

[1] C. Monat, P. Domachuk, and B. J. Eggleton. Integrated optofluidics: A new river of light. *Nature Photonics*, 1(2):106–114, 2007. doi:10.1038/nphoton.2006.96.

[2] D. Psaltis, S. R. Quake, and C. Yang. Developing optofluidic technology through the fusion of microfluidics and optics. *Nature*, 442(7101):381–386, 2006. doi:10.1038/nature05060.

[3] A. R. Hawkins and H. Schmidt. *Handbook of optofluidics*. CRC Press, 2010. ISBN 9781138113602.

[4] R. Baets, P. Bienstman, W. Bogaerts, P. Brouckaert, J.and Debackere, P. Dumon, G. Roelkens, S. Scheerlinck, M. Smit, and D. Taillaert. Progress in high index contrast integrated optics. In *Proceedings of the European Conference on Integrated Optics (ECIO 2007)*, 2007.

[5] T. Higashihara and M. Ueda. Recent Progress in High Refractive Index Polymers. *Macromolecules*, 48(7):1915–1929, 2015. doi:10.1021/ma502569r.

[6] P. R. Villeneuve, S. H. Fan, J. D. Joannopoulos, K. Y. Lim, G. S. Petrich, L. A. Kolodziejski, and R. Reif. Air-Bridge Microcavities. *Applied Physics Letters*, 67(2):167–169, 1995. doi:10.1063/1.114655.

[7] N. Carlsson, N. Ikeda, Y. Sugimoto, K. Asakawa, T. Takemori, Y. Katayama, N. Kawai, and K. Inoue. Design, nano-fabrication and analysis of near-infrared 2D photonic crystal air-bridge structures. *Optical and Quantum Electronics*, 34(1-3):123–131, 2002. doi:10.1023/A:1013348708774.

[8] Q. F. Liu, Z. Shi, G. Y. Zhu, W. Wang, Z. H. Wang, and Y. J. Wang. Freestanding GaN grating couplers at visible wavelengths. *Journal of Optics*, 17(4):045607, 2015. doi:10.1088/2040-8978/17/4/045607.

[9] M. Loncar, T. Doll, J. Vuckovic, and A. Scherer. Design and fabrication of silicon photonic crystal optical waveguides. *Journal of Lightwave Technology*, 18(10):1402–1411, 2000. doi:10.1109/50.887192.

[10] M. O. Heuschkel, L. Guerin, B. Buisson, D. Bertrand, and P. Renaud. Buried microchannels in photopolymer for delivering of solutions to neurons in a network. *Sensors and Actuators B: Chemical*, 48(1-3):356–361, 1998. doi:10.1016/S0925-4005(98)00071-9.

[11] P. Abgrall, C. Lattes, V. Conederal, X. Dollat, S. Colin, and A. M. Gue. A novel fabrication method of flexible and monolithic 3D microfluidic structures using lamination of SU-8 films. *Journal of Micromechanics and Microengineering*, 16(1):113–121, 2006. doi:10.1088/0960-1317/16/1/016.

[12] J. Steigert, O. Brett, C. Muller, M. Strasser, N. Wangler, H. Reinecke, M. Daub, and R. Zengerle. A versatile and flexible low-temperature full-wafer bonding process of monolithic 3D microfluidic structures in SU-8. *Journal of Micromechanics and Microengineering*, 18(9):095013, 2008. doi:10.1088/0960-1317/18/9/095013.

[13] F. J. Blanco, M. Agirregabiria, J. Garcia, J. Berganzo, M. Tijero, M. T. Arroyo, J. M. Ruano, I. Aramburu, and K. Mayora. Novel three-dimensional embedded SU-8 microchannels fabricated using a low temperature full wafer adhesive bonding. *Journal of Micromechanics and Microengineering*, 14(7): 1047–1056, 2004. doi:10.1088/0960-1317/14/7/027.

[14] J. M. Ruano-López, M. Aguirregabiria, M. Tijero, M. T. Arroyo, J. Elizalde, J. Berganzo, I. Aranburu, F. J. Blanco, and K. Mayora. A new SU-8 process to integrate buried waveguides and sealed microchannels for a Lab-on-a-Chip. *Sensors and Actuators B: Chemical*, 114(1):542–551, 2006. doi:10.1016/j.snb.2005.05.011.

[15] M. Agirregabiria, F. J. Blanco, J. Berganzo, M. T. Arroyo, A. Fullaondo, K. Mayora, and J. M. Ruano-Lopez. Fabrication of SU-8 multilayer microstructures based on successive CMOS compatible adhesive bonding and releasing steps. *Lab Chip*, 5(5):545–52, 2005. doi:10.1039/b500519a.

[16] A. Ezkerra, L. J. Fernandez, K. Mayora, and J. M. Ruano-Lopez. Fabrication of SU-8 free-standing structures embedded in microchannels for microfluidic control. *Journal of Micromechanics and Microengineering*, 17(11): 2264–2271, 2007. doi:10.1088/0960-1317/17/11/013.

[17] Z. C. Peng, Z. G. Ling, M. Tondra, C. G. Liu, M. Zhang, K. Lian, J. Goettert, and J. Hormes. CMOS compatible integration of three-dimensional microfluidic systems based on low-temperature transfer of SU-8 films. *Journal of Microelectromechanical Systems*, 15(3):708–716, 2006. doi:10.1109/Jmems.2006.876793.

[18] D. Haefliger and A. Boisen. Three-dimensional microfabrication in negative resist using printed masks. *Journal of Micromechanics and Microengineering*, 16(5):951–957, 2006. doi:10.1088/0960-1317/16/5/011.

[19] C. Aracil, F. Perdigones, J. M. Moreno, and J. M. Quero. BETTS: bonding, exposing and transferring technique in SU-8 for microsystems fabrication. *Journal of Micromechanics and Microengineering*, 20(3):035008, 2010. doi:10.1088/0960-1317/20/3/035008.

[20] A. Boudrioua. *Photonic Waveguides: Theory and Applications*. ISTE Ltd and John Wiley & Sons Inc, London, 2009. ISBN 9781848210271. doi:10.1002/9780470611142.ch6.

[21] D. Taillaert, W. Bogaerts, P. Bienstman, T. F. Krauss, P. Van Daele, I. Moerman, S. Verstuyft, K. De Mesel, and R. Baets. An out-of-plane grating coupler for efficient butt-coupling between compact planar waveguides and single-mode fibers. *IEEE Journal of Quantum Electronics*, 38(7):949–955, 2002. doi:10.1109/Jqe.2002.1017613.

[22] I. M. White and X. Fan. On the performance quantification of resonant refractive index sensors. *Opt Express*, 16(2):1020–8, 2008. doi:10.1364/OE.16.001020.

[23] Bundesministerium für Bildung und Forschung. Ideen. Innovation. Wachstum. Hightech-Strategie 2020 für Deutschland. *Available at:* `http://www.bmbf.de:8001/pub/Ideen_Innovation_Wachstum.pdf`, 2010.

[24] D. Qin, Y. Xia, J. A. Rogers, R. J. Jackman, X. Zhao, and G. M. Whitesides. Microfabrication, Microstructures and Microsystems. In A. Manz and H. Becker, editors, *Microsystem Technology in Chemistry and Life Sciences*, pages 1–20. Springer, 1998. doi:10.1007/3-540-69544-3_1.

[25] W. M. Moreau. *Semiconductor lithography: principles, practices, and materials*. Springer Science & Business Media, 2012. ISBN 9781461282280.

[26] S. Thomas and W. Yang. *Advances in Polymer Processing: From Macro- To Nano-Scales*. Woodhead Publishing Online. Elsevier Science, 2009. ISBN 9781845696429.

[27] H. Becker and C. Gartner. Polymer microfabrication technologies for microfluidic systems. *Anal Bioanal Chem*, 390(1):89–111, 2008. doi:10.1007/s00216-007-1692-2.

[28] M. J. Madou. *Manufacturing techniques for microfabrication and nanotechnology*, volume 2. CRC Press, 2011. ISBN 9781420055191.

[29] D. Qin, Y. Xia, and G. M. Whitesides. Soft lithography for micro- and nanoscale patterning. *Nat Protoc*, 5(3):491–502, 2010. doi:10.1038/nprot.2009.234.

[30] Y. Shin, S. Han, J. S. Jeon, K. Yamamoto, I. K. Zervantonakis, R. Sudo, R. D. Kamm, and S. Chung. Microfluidic assay for simultaneous culture of multiple cell types on surfaces or within hydrogels. *Nat Protoc*, 7(7):1247–59, 2012. doi:10.1038/nprot.2012.051.

[31] L. J. Guo. Nanoimprint lithography: Methods and material requirements. *Advanced Materials*, 19(4):495–513, 2007. doi:10.1002/adma.200600882.

[32] H. Schift. Nanoimprint lithography: An old story in modern times? A review. *Journal of Vacuum Science & Technology B: Microelectronics and Nanometer Structures*, 26(2):458, 2008. doi:10.1116/1.2890972.

[33] S. Y. Chou. Sub-10 nm imprint lithography and applications. *Journal of Vacuum Science & Technology B: Microelectronics and Nanometer Structures*, 15(6):2897, 1997. doi:10.1116/1.589752.

[34] S. Zankovych, T. Hoffmann, J. Seekamp, J. U. Bruch, and C. M. S. Torres. Nanoimprint lithography: challenges and prospects. *Nanotechnology*, 12(2): 91–95, 2001. doi:10.1088/0957-4484/12/2/303.

[35] S. Y. Chou, P. R. Krauss, and P. J. Renstrom. Imprint lithography with 25-nanometer resolution. *Science*, 272(5258):85–87, 1996. doi:10.1126/science.272.5258.85.

[36] H. Schift and A. Kristensen. Nanoimprint Lithography - Patterning of Resists Using Molding. In *Handbook of Nanotechnology*, pages 271–312. Springer, 2010. doi:10.1007/978-3-642-02525-9_9.

[37] Y. Xia and G. M. Whitesides. Soft lithography. *Annual Review of Materials Science*, 28(1):153–184, 1998. doi:10.1146/annurev.matsci.28.1.153.

[38] S. J Clarson and J A. Semlyen. *Siloxane polymers*. Prentice Hall, 1993. ISBN 9780138163150.

[39] D. B. Weibel, W. R. Diluzio, and G. M. Whitesides. Microfabrication meets microbiology. *Nat Rev Microbiol*, 5(3):209–18, 2007. doi:10.1038/nrmicro1616.

[40] R. Luttge. *Nano- and Microfabrication for Industrial and Biomedical Applications*. William Andrew, 2016. ISBN 9780323378284.

[41] G. Voskerician, M. S. Shive, R. S. Shawgo, H. von Recum, J. M. Anderson, M. J. Cima, and R. Langer. Biocompatibility and biofouling of MEMS drug delivery devices. *Biomaterials*, 24(11):1959–67, 2003. doi:10.1016/s0142-9612(02)00565-3.

[42] M. C. Belanger and Y. Marois. Hemocompatibility, biocompatibility, inflammatory and in vivo studies of primary reference materials low-density polyethylene and polydimethylsiloxane: a review. *J Biomed Mater Res*, 58 (5):467–77, 2001. doi:10.1002/jbm.1043.

[43] C. Prokop, S. Schoenhardt, T. Mahmud, A. Mitchell, and C. Karnutsch. Bonding of SU-8 films onto KMPR structures for microfluidic, air-suspended photonic and optofluidic applications. *Journal of Micromechanics and Microengineering*, 26(5):055001, 2016. doi:10.1088/0960-1317/26/5/055001.

[44] C. T. Ko and K. N. Chen. Wafer-level bonding/stacking technology for 3D integration. *Microelectronics Reliability*, 50(4):481–488, 2010. doi:10.1016/j.microrel.2009.09.015.

[45] C. Tsao and D. L. DeVoe. Bonding of thermoplastic polymer microfluidics. *Microfluidics and Nanofluidics*, 6(1):1–16, 2008. doi:10.1007/s10404-008-0361-x.

[46] H. Shadpour, M. L. Hupert, D. Patterson, C. Liu, M. Galloway, W. Stryjewski, J. Goettert, and S. A. Soper. Multichannel microchip electrophoresis device fabricated in polycarbonate with an integrated contact conductivity sensor array. *Anal Chem*, 79(3):870–8, 2007. doi:10.1021/ac0612168.

[47] J. Li, D. Chen, and G. Chen. Low-Temperature Thermal Bonding of PMMA Microfluidic Chips. *Analytical Letters*, 38(7):1127–1136, 2005. doi:10.1081/al-200057209.

[48] X. Zhu, G. Liu, Y. Guo, and Y. Tian. Study of PMMA thermal bonding. *Microsystem Technologies*, 13(3-4):403–407, 2006. doi:10.1007/s00542-006-0224-x.

[49] X. Sun, B. A. Peeni, W. Yang, H. A. Becerril, and A. T. Woolley. Rapid prototyping of poly(methyl methacrylate) microfluidic systems using solvent imprinting and bonding. *J Chromatogr A*, 1162(2):162–6, 2007. doi:10.1016/j.chroma.2007.04.002.

[50] J. Steigert, S. Haeberle, T. Brenner, C. Mueller, C. P. Steinert, P. Koltay, N. Gottschlich, H. Reinecke, J. Rühe, R. Zengerle, and J. Ducrée. Rapid prototyping of microfluidic chips in COC. *Journal of Micromechanics and Microengineering*, 17(2):333–341, 2007. doi:10.1088/0960-1317/17/2/020.

[51] A. Bhattacharyya and C. M. Klapperich. Thermoplastic microfluidic device for on-chip purification of nucleic acids for disposable diagnostics. *Anal Chem*, 78(3):788–92, 2006. doi:10.1021/ac051449j.

[52] H. Shadpour, H. Musyimi, J. Chen, and S. A. Soper. Physiochemical properties of various polymer substrates and their effects on microchip electrophoresis performance. *J Chromatogr A*, 1111(2):238–51, 2006. doi:10.1016/j.chroma.2005.08.083.

[53] K. B. Mogensen, J. El-Ali, A. Wolff, and J. P. Kutter. Integration of polymer waveguides for optical detection in microfabricated chemical analysis systems. *Appl Opt*, 42(19):4072–9, 2003. doi:10.1364/Ao.42.004072.

[54] L. Gutierrez-Rivera, J. Martinez-Quijada, R. Johnstone, D. Elliott, C. Backhouse, and D. Sameoto. Multilayer bonding using a conformal adsorbate film (CAF) for the fabrication of 3D monolithic microfluidic devices in photopolymer. *Journal of Micromechanics and Microengineering*, 22(8):085018, 2012. doi:10.1088/0960-1317/22/8/085018.

[55] E. Zeller, F. H. Bennet, D. N. Neshev, and A. Mitchell. Laminated Air Structured and Fluid Infiltrated Polymer Waveguides. *IEEE Photonics Technology Letters*, 23(21):1564–1566, 2011. doi:10.1109/Lpt.2011.2164396.

[56] D. C. Duffy, J. C. McDonald, O. J. Schueller, and G. M. Whitesides. Rapid Prototyping of Microfluidic Systems in Poly(dimethylsiloxane). *Anal Chem*, 70(23):4974–84, 1998. doi:10.1021/ac980656z.

[57] R. J. Jackman, T. M. Floyd, R. Ghodssi, M. A. Schmidt, and K. F. Jensen. Microfluidic systems with on-line UV detection fabricated in photodefinable epoxy. *Journal of Micromechanics and Microengineering*, 11(3):263–269, 2001. doi:10.1088/0960-1317/11/3/316.

[58] H. Lorenz, M. Despont, N. Fahrni, N. LaBianca, P. Renaud, and P. Vettiger. SU-8: a low-cost negative resist for MEMS. *Journal of Micromechanics and Microengineering*, 7(3):121–124, 1997. doi:10.1088/0960-1317/7/3/010.

[59] J.D. Gelorme, R.J. Cox, and S.A.R. Gutierrez. Photoresist composition and printed circuit boards and packages made therewith, 1989. US Patent US4882245 A.

[60] H. Lorenz, M. Despont, N. Fahrni, J. Brugger, P. Vettiger, and P. Renaud. High-aspect-ratio, ultrathick, negative-tone near-UV photoresist and its applications for MEMS. *Sensors and Actuators A: Physical*, 64(1):33–39, 1998. doi:10.1016/S0924-4247(98)80055-1.

[61] H. Lorenz, M. Despont, P. Vettiger, and P. Renaud. Fabrication of photoplastic high-aspect ratio microparts and micromolds using SU-8 UV resist. *Microsystem Technologies*, 4(3):143–146, 1998. doi:10.1007/s005420050118.

[62] E. H. Conradie and D. F. Moore. SU-8 thick photoresist processing as a functional material for MEMS applications. *Journal of Micromechanics and Microengineering*, 12(4):368–374, 2002. doi:10.1088/0960-1317/12/4/303.

[63] A. L. Bogdanov and S. S. Peredkov. Use of SU-8 photoresist-for very high aspect ratio x-ray lithography. *Microelectronic Engineering*, 53(1-4):493–496, 2000. doi:10.1016/S0167-9317(00)00363-4.

[64] B. Bilenberg, S. Jacobsen, M. S. Schmidt, L. H. D. Skjolding, P. Shi, P. Bøggild, J. O. Tegenfeldt, and A. Kristensen. High resolution 100kV electron beam lithography in SU-8. *Microelectronic Engineering*, 83(4-9):1609–1612, 2006. doi:10.1016/j.mee.2006.01.142.

[65] J. M. Shaw, J. D. Gelorme, N. C. LaBianca, W. E. Conley, and S. J. Holmes. Negative photoresists for optical lithography. *IBM Journal of Research and Development*, 41(1-2):81–94, 1997. doi:10.1147/rd.411.0081.

[66] MicroChem Corp. SU-8 2000 Permanent Epoxy Negative Photoresist datasheeet, version SU-82000DataSheet2025thru2075Ver4. *Available at:* `http://http://www.microchem.com/pdf/SU-82000DataSheet2025thru2075Ver4.pdf`. Viewed 20 Nov. 2016.

[67] H. H. Gatzen, V. Saile, and J. Leuthold. *Micro and Nano Fabrication: Tools and Processes*, volume 1. Springer-Verlag Berlin Heidelberg, 2015. ISBN 9783662443958. doi:10.1007/978-3-662-44395-8.

[68] S. Arscott. SU-8 as a material for lab-on-a-chip-based mass spectrometry. *Lab Chip*, 14(19):3668–89, 2014. doi:10.1039/c4lc00617h.

[69] C. J. Robin, A. Vishnoi, and K. N. Jonnalagadda. Mechanical Behavior and Anisotropy of Spin-Coated SU-8 Thin Films for MEMS. *Journal of Microelectromechanical Systems*, 23(1):168–180, 2014. doi:10.1109/Jmems.2013.2264341.

[70] G. Kotzar, M. Freas, P. Abel, A. Fleischman, S. Roy, C. Zorman, J. M. Moran, and J. Melzak. Evaluation of MEMS materials of construction for implantable medical devices. *Biomaterials*, 23(13):2737–50, 2002. doi:10.1016/s0142-9612(02)00007-8.

[71] K. V. Nemani, K. L. Moodie, J. B. Brennick, A. Su, and B. Gimi. In vitro and in vivo evaluation of SU-8 biocompatibility. *Mater Sci Eng C Mater Biol Appl*, 33(7):4453–9, 2013. doi:10.1016/j.msec.2013.07.001.

[72] L. Wang, Z. Z. Wu, B. Q. Xu, Y. P. Zhao, and W. S. Kisaalita. SU-8 microstructure for quasi-three-dimensional cell-based biosensing. *Sensors and Actuators B: Chemical*, 140(2):349–355, 2009. doi:10.1016/j.snb.2009.05.009.

[73] R. Marie, S. Schmid, A. Johansson, L. Ejsing, M. Nordstrom, D. Hafliger, C. B. Christensen, A. Boisen, and M. Dufva. Immobilisation of DNA to polymerised SU-8 photoresist. *Biosens Bioelectron*, 21(7):1327–32, 2006. doi:10.1016/j.bios.2005.03.004.

[74] J. C. Ribeiro, G. Minas, P. Turmezei, R. F. Wolffenbuttel, and J. H. Correia. A SU-8 fluidic microsystem for biological fluids analysis. *Sensors and Actuators A: Physical*, 123-24:77–81, 2005. doi:10.1016/j.sna.2005.03.032.

[75] V. N. Vernekar, D. K. Cullen, N. Fogleman, Y. Choi, A. J. Garcia, M. G. Allen, G. J. Brewer, and M. C. LaPlaca. SU-8 2000 rendered cytocompatible for neuronal bioMEMS applications. *J Biomed Mater Res A*, 89(1):138–51, 2009. doi:10.1002/jbm.a.31839.

[76] Y. J. Chuang, F. G. Tseng, J. H. Cheng, and W. K. Lin. A novel fabrication method of embedded micro-channels by using SU-8 thick-film photoresists. *Sensors and Actuators A: Physical*, 103(1-2):64–69, 2003. doi:10.1016/S0924-4247(02)00325-4.

[77] S. Arscott, S. L. Gac, C. Druon, P. Tabourier, and C. Rolando. A planar on-chip micro-nib interface for NanoESI-MS microfluidic applications. *Journal of Micromechanics and Microengineering*, 14(2):310–316, 2004. doi:10.1088/0960-1317/14/2/021.

[78] S. Arscott, F. Garet, P. Mounaix, L. Duvillaret, J. L. Coutaz, and D. Lippens. Terahertz time-domain spectroscopy of films fabricated from SU-8. *Electronics Letters*, 35(3):243, 1999. doi:10.1049/el:19990146.

[79] J. Carlier, S. Arscott, V. Thomy, J. C. Fourrier, F. Caron, J. C. Camart, C. Druon, and P. Tabourier. Integrated microfluidics based on multi-layered SU-8 for mass spectrometry analysis. *Journal of Micromechanics and Microengineering*, 14(4):619–624, 2004. doi:10.1088/0960-1317/14/4/024.

[80] A. Mata, A. J. Fleischman, and S. Roy. Fabrication of multi-layer SU-8

microstructures. *Journal of Micromechanics and Microengineering*, 16(2): 276–284, 2006. doi:10.1088/0960-1317/16/2/012.

[81] F. D. Mbairi and H. Hesselbom. High frequency design and characterization of SU-8 based conductor backed coplanar waveguide transmission lines. *International Symposium on Advanced Packaging Materials: Processes, Properties and Interfaces*, pages 243–248, 2005. doi:10.1109/isapm.2005.1432083.

[82] B. Bêche, N. Pelletier, E. Gaviot, and J. Zyss. Single-mode TE_{00}-TM_{00} optical waveguides on SU-8 polymer. *Optics Communications*, 230(1-3): 91–94, 2004. doi:10.1016/j.optcom.2003.11.016.

[83] S. Lee, C. Chen, V. V. Deshpande, G. Lee, I. Lee, M. Lekas, A. Gondarenko, Y. Yu, K. Shepard, P. Kim, and J. Hone. Electrically integrated SU-8 clamped graphene drum resonators for strain engineering. *Applied Physics Letters*, 102(15):153101, 2013. doi:10.1063/1.4793302.

[84] C. Lin, G. Lee, B. Chang, and G. Chang. A new fabrication process for ultra-thick microfluidic microstructures utilizing SU-8 photoresist. *Journal of Micromechanics and Microengineering*, 12(5):590–597, 2002. doi:10.1088/0960-1317/12/5/312.

[85] J. Zhang, K. L. Tan, G. D. Hong, L. J. Yang, and H. Q. Gong. Polymerization optimization of SU-8 photoresist and its applications in microfluidic systems and MEMS. *Journal of Micromechanics and Microengineering*, 11 (1):20–26, 2001. doi:10.1088/0960-1317/11/1/304.

[86] M. Calleja, M. Nordstrom, M. Alvarez, J. Tamayo, L. M. Lechuga, and A. Boisen. Highly sensitive polymer-based cantilever-sensors for DNA detection. *Ultramicroscopy*, 105(1-4):215–22, 2005. doi:10.1016/j.ultramic.2005.06.039.

[87] Thaysen, J. and Yalcinkaya, A. D. and Vestergaard, R. K. and Jensen, S. and Mortensen, M. W. and Vettiger, P. and Menon, A. SU-8 based piezoresistive mechanical sensor. *The Fifteenth IEEE International Conference on Micro Electro Mechanical Systems*, pages 320–323, 2002. doi:10.1109/memsys.2002.984267.

[88] P. Abgrall, V. Conedera, H. Camon, A. M. Gue, and N. T. Nguyen. SU-8 as a structural material for labs-on-chips and microelectromechanical systems. *Electrophoresis*, 28(24):4539–51, 2007. doi:10.1002/elps.200700333.

[89] B. Bilenberg, T. Nielsen, B. Clausen, and A. Kristensen. PMMA to SU-8 bonding for polymer based lab-on-a-chip systems with integrated optics. *Journal of Micromechanics and Microengineering*, 14(6):814–818, 2004. doi:10.1088/0960-1317/14/6/008.

[90] H. R. Miller, D. W. Johnson, and S. Mori. KMPR Photoresist Process Optimization Using Factorial Experimental Design. *Journal of Photopolymer Science and Technology*, 17(5):677–684, 2004. doi:10.2494/photopolymer.17.677.

[91] C. Lee and K. Jiang. KMPR photoresist for fabrication of thick microstructures. In *Proceedings of the Third International Conference on Multi-Material Micro Manufacture*, pages 207–210, 2007. ISBN 9781420070040.

[92] C. Salm, V. M. Blanco Carballo, J. Melai, and J. Schmitz. Reliability aspects of a radiation detector fabricated by post-processing a standard CMOS chip. *Microelectronics Reliability*, 48(8-9):1139–1143, 2008. doi:10.1016/j.microrel.2008.06.038.

[93] J. Park, J. Fattaccioli, H. Fujita, and B. Kim. Fabrication of aluminum/alumina patterns using localized anodization of aluminum. *International Journal of Precision Engineering and Manufacturing*, 13(5):765–770, 2012. doi:10.1007/s12541-012-0100-9.

[94] V. M. Blanco Carballo, J. Melai, C. Salm, and J. Schmitz. Moisture resistance of SU-8 and KMPR as structural material. *Microelectronic Engineering*, 86(4-6):765–768, 2009. doi:10.1016/j.mee.2008.12.076.

[95] K. S. Ou, H. Y. Yan, and K. S. Chen. Mechanical Characterization of KMPR by Nano-Indentation for MEMS Applications. *Strain*, 44(3):267–271, 2008. doi:10.1111/j.1475-1305.2007.00367.x.

[96] X. Wei, C. H. Lee, Z. Jiang, and K. Jiang. Thick photoresists for electroforming metallic microcomponents. *Proceedings of the Institution of Mechanical*

Engineers Part C-Journal of Mechanical Engineering Science, 222(1):37–42, 2008. doi:10.1243/09544062JMES786.

[97] T. Ray, H. Zhu, I. S. Elango, and D. R. Meldrum. Characterization of KMPR 1025 as a masking layer for deep reactive ion etching of fused silica. *Proceedings of the IEEE International Conference on Micro Electro Mechanical Systems (MEMS)*, pages 213–216, 2011. doi:10.1109/memsys.2011.5734399.

[98] L. Convert, V. Aimez, P. Charette, and R. Lecomte. Rapid prototyping of integrated microfluidic devices for combined radiation detection and plasma separation. *MNRC 2008: Proc. IEEE 1st Conf. Microsystems and Nanoelectronics Research*, pages 105–108, 2008. doi:10.1109/mnrc.2008.4683389.

[99] T. Ray, H. Zhu, and D. R. Meldrum. Deep reactive ion etching of fused silica using a single-coated soft mask layer for bio-analytical applications. *Journal of Micromechanics and Microengineering*, 20(9):097002, 2010. doi:10.1088/0960-1317/20/9/097002.

[100] S. Young-Min, D. Gamzina, L. R. Barnett, F. Yaghmaie, A. Baig, and N. C. Luhmann. UV Lithography and Molding Fabrication of Ultrathick Micrometallic Structures Using a KMPR Photoresist. *Journal of Microelectromechanical Systems*, 19(3):683–689, 2010. doi:10.1109/jmems.2010.2045880.

[101] C. H. Lee and K. Jiang. Fabrication of thick electroforming micro mould using a KMPR negative tone photoresist. *Journal of Micromechanics and Microengineering*, 18(5):055032, 2008. doi:10.1088/0960-1317/18/5/055032.

[102] M. D. Ynsa, P. Shao, S. R. Kulkarni, N. N. Liu, and J. A. van Kan. Exposure parameters in proton beam writing for KMPR and EPO Core negative tone photoresists. *Nuclear Instruments and Methods in Physics Research Section B: Beam Interactions with Materials and Atoms*, 269(20):2409–2412, 2011. doi:10.1016/j.nimb.2011.02.027.

[103] C. Richard, A. Renaudin, V. Aimez, and P. G. Charette. An integrated hybrid interference and absorption filter for fluorescence detection in lab-on-a-chip devices. *Lab Chip*, 9(10):1371–6, 2009. doi:10.1039/b819080a.

[104] W. Noll. Zur Chemie und Technologie der Silicone. *Angewandte Chemie*, 66 (2):41–55, 1954. doi:10.1002/ange.19540660202.

[105] J. C. McDonald, D. C. Duffy, J. R. Anderson, D. T. Chiu, H. Wu, O. J. Schueller, and G. M. Whitesides. Fabrication of microfluidic systems in poly(dimethylsiloxane). *Electrophoresis*, 21 (1):27–40, 2000. doi:10.1002/(SICI)1522-2683(20000101)21:1<27::AID-ELPS27>3.0.CO;2-C.

[106] J. C. McDonald and G. M. Whitesides. Poly(dimethylsiloxane) as a material for fabricating microfluidic devices. *Accounts of Chemical Research*, 35(7): 491–499, 2002. doi:10.1021/ar010110q.

[107] G. M. Whitesides, E. Ostuni, S. Takayama, X. Jiang, and D. E. Ingber. Soft lithography in biology and biochemistry. *Annu Rev Biomed Eng*, 3:335–73, 2001. doi:10.1146/annurev.bioeng.3.1.335.

[108] H. Hillborg, J. F. Ankner, U. W. Gedde, G. D. Smith, H. K. Yasuda, and K. Wikstrom. Crosslinked polydimethylsiloxane exposed to oxygen plasma studied by neutron reflectometry and other surface specific techniques. *Polymer*, 41(18):6851–6863, 2000. doi:10.1016/S0032-3861(00)00039-2.

[109] S. H. Tan, N. T. Nguyen, Y. C. Chua, and T. G. Kang. Oxygen plasma treatment for reducing hydrophobicity of a sealed polydimethylsiloxane microchannel. *Biomicrofluidics*, 4(3):32204, 2010. doi:10.1063/1.3466882.

[110] S. Bhattacharya, A. Datta, J. M. Berg, and S. Gangopadhyay. Studies on surface wettability of poly(dimethyl) siloxane (PDMS) and glass under oxygen-plasma treatment and correlation with bond strength. *Journal of Microelectromechanical Systems*, 14(3):590–597, 2005. doi:10.1109/jmems.2005.844746.

[111] J. M. Ng, I. Gitlin, A. D. Stroock, and G. M. Whitesides. Components for integrated poly(dimethylsiloxane) microfluidic systems. *Electrophoresis*, 23(20):3461–73, 2002. doi:10.1002/1522-2683(200210)23:20<3461::AID-ELPS3461>3.0.CO;2-8.

[112] S. L. Peterson, A. McDonald, P. L. Gourley, and D. Y. Sasaki. Poly(dimethylsiloxane) thin films as biocompatible coatings for microflu-

idic devices: cell culture and flow studies with glial cells. *J Biomed Mater Res A*, 72(1):10–8, 2005. doi:10.1002/jbm.a.30166.

[113] M. Kakuta, F. G. Bessoth, and A. Manz. Microfabricated devices for fluid mixing and their application for chemical synthesis. *Chem Rec*, 1(5):395–405, 2001. doi:10.1002/tcr.1023.

[114] R. Mukhopadhyay. When PDMS isn't the best. *Analytical Chemistry*, 79 (9):3248–3253, 2007. doi:10.1021/ac071903e.

[115] J. Friend and L. Yeo. Fabrication of microfluidic devices using polydimethylsiloxane. *Biomicrofluidics*, 4(2), 2010. doi:10.1063/1.3259624.

[116] F. Schneider, T. Fellner, J. Wilde, and U. Wallrabe. Mechanical properties of silicones for MEMS. *Journal of Micromechanics and Microengineering*, 18(6), 2008. doi:10.1088/0960-1317/18/6/065008.

[117] F. Schneider, J. Draheirn, R. Kamberger, and U. Wallrabe. Process and material properties of polydimethylsiloxane (PDMS) for Optical MEMS. *Sensors and Actuators A: Physical*, 151(2):95–99, 2009. doi:10.1016/j.sna.2009.01.026.

[118] A. Mata, A. J. Fleischman, and S. Roy. Characterization of polydimethylsiloxane (PDMS) properties for biomedical micro/nanosystems. *Biomed Microdevices*, 7(4):281–93, 2005. doi:10.1007/s10544-005-6070-2.

[119] J. M. Spotts. Fabrication of PDMS Microfluidic Devices. *Institute for Systems Biology*, 2008.

[120] Z. Zhang, P. Zhao, G. Xiao, B. R. Watts, and C. Xu. Sealing SU-8 microfluidic channels using PDMS. *Biomicrofluidics*, 5(4):46503–465038, 2011. doi:10.1063/1.3659016.

[121] F. Schneider, J. Draheim, R. Kamberger, and U. Wallrabe. Process and material properties of polydimethylsiloxane (PDMS) for Optical MEMS. *Sensors and Actuators A: Physical*, 151(2):95–99, 2009. doi:10.1016/j.sna.2009.01.026.

[122] T. C. Sum, A. A. Bettiol, J. A. van Kan, F. Watt, E. Y. B. Pun, and K. K. Tung. Proton beam writing of low-loss polymer optical waveguides. *Applied Physics Letters*, 83(9):1707–1709, 2003. doi:10.1063/1.1606502.

[123] N. T. Nguyen and Z. Wu. Micromixers - a review. *Journal of Micromechanics and Microengineering*, 15(2):R1–R16, 2005. doi:10.1088/0960-1317/15/2/r01.

[124] Y. K. Suh and S. Kang. A Review on Mixing in Microfluidics. *Micromachines*, 1(3):82–111, 2010. doi:10.3390/mi1030082.

[125] I. Glasgow and N. Aubry. Enhancement of microfluidic mixing using time pulsing. *Lab Chip*, 3(2):114–20, 2003. doi:10.1039/b302569a.

[126] V. Hessel, H. Löwe, and F. Schönfeld. Micromixers - a review on passive and active mixing principles. *Chemical Engineering Science*, 60(8-9):2479–2501, 2005. doi:10.1016/j.ces.2004.11.033.

[127] M. A. Eddings, M. A. Johnson, and B. K. Gale. Determining the optimal PDMS-PDMS bonding technique for microfluidic devices. *Journal of Micromechanics and Microengineering*, 18(6):067001, 2008. doi:10.1088/0960-1317/18/6/067001.

[128] P. Abgrall, S. Charlot, R. Fulcrand, L. Paul, A. Boukabache, and A. M. Gue. Low-stress fabrication of 3D polymer free standing structures using lamination of photosensitive films. *Microsystem Technologies-Micro-and Nanosystems-Information Storage and Processing Systems*, 14(8):1205–1214, 2008. doi:10.1007/s00542-008-0625-0.

[129] C. Prokop, P. Kleeßen, N. Irmler, A. Mitchell, and C. Karnutsch. Air-suspended polymer rib waveguides. In *SPIE OPTO. International Society for Optics and Photonics, San Francisco, United States of America*, volume 9365. Proc. SPIE 9365, Integrated Optics: Devices, Materials, and Technologies XIX, 2015. doi:10.1117/12.2079207.

[130] V. R. Almeida, C. A. Barrios, R. R. Panepucci, and M. Lipson. All-optical control of light on a silicon chip. *Nature*, 431(7012):1081–4, 2004. doi:10.1038/nature02921.

[131] S. McNab, N. Moll, and Y. Vlasov. Ultra-low loss photonic integrated circuit with membrane-type photonic crystal waveguides. *Opt Express*, 11(22):2927–39, 2003. doi:10.1364/OE.11.002927.

[132] G. Y. Si, E. J. Teo, A. A. Bettiol, J. H. Teng, and A. J. Danner. Suspended slab and photonic crystal waveguides in lithium niobate. *Journal of Vacuum Science & Technology B*, 28(2):316–320, 2010. doi:10.1116/1.3327925.

[133] M. Schmidt, G. Boettger, M. Eich, W. Morgenroth, U. Huebner, R. Boucher, H. G. Meyer, D. Konjhodzic, H. Bretinger, and F. Marlow. Ultralow refractive index substrates-a base for photonic crystal slab waveguides. *Applied Physics Letters*, 85(1):16–18, 2004. doi:10.1063/1.1767962.

[134] Q. Fang, T. Y. Liow, J. F. Song, C. W. Tan, M. B. Yu, G. Q. Lo, and D. L. Kwong. Suspended optical fiber-to-waveguide mode size converter for silicon photonics. *Opt Express*, 18(8):7763–9, 2010. doi:10.1364/OE.18.007763.

[135] J. Brandrup, E. H. Immergut, E. A. Gruike, A. Abe, and D. R. Bloch. *Polymer Handbook*. ISTE Ltd and John Wiley & Sons Inc, New York, 4th edition, 2005. ISBN 9780471479369.

[136] R. Bruck and R. Hainberger. Efficient coupling of narrow beams into polyimide waveguides by means of grating couplers with high-index coating. *Appl Opt*, 49(10):1972–8, 2010. doi:10.1364/AO.49.001972.

[137] L. H. Wang, Y. L. Li, M. G. Porcel, D. Vermeulen, X. Y. Han, J. Y. Wang, X. G. Jian, R. Baets, M. S. Zhao, and G. Morthier. A polymer-based surface grating coupler with an embedded Si_3N_4 layer. *Journal of Applied Physics*, 111(11):114507, 2012. doi:10.1063/1.4724335.

[138] X. Wei, C. Kang, M. Liscidini, G. Rong, S. T. Retterer, M. Patrini, J. E. Sipe, and S. M. Weiss. Grating couplers on porous silicon planar waveguides for sensing applications. *Journal of Applied Physics*, 104(12):123113, 2008. doi:10.1063/1.3043579.

[139] P. Yang, G. Wirnsberger, H. C. Huang, S. R. Cordero, M. D. McGehee, B. Scott, T. Deng, G. M. Whitesides, B. F. Chmelka, S. K. Buratto, and G. D. Stucky. Mirrorless lasing from mesostructured wave-

guides patterned by soft lithography. *Science*, 287(5452):465–467, 2000. doi:10.1126/science.287.5452.465.

[140] W. P. Risk, H-C. Kim, R. D. Miller, H. Temkin, and S. Gangopadhyay. Optical waveguides with an aqueous core and a low-index nanoporous cladding. *Optics express*, 12(26):6446–6455, 2004. doi:10.1364/OPEX.12.006446.

[141] E. V. Astrova and V. A. Tolmachev. Effective refractive index and composition of oxidized porous silicon films. *Materials Science and Engineering: B*, 69:142–148, 2000. doi:10.1016/S0921-5107(99)00236-6.

[142] T. Fukazawa, T. Hirano, F. Ohno, and T. Baba. Low loss intersection of Si photonic wire waveguides. *Japanese Journal of Applied Physics Part 1-Regular Papers Short Notes & Review Papers*, 43(2):646–647, 2004. doi:10.1143/Jjap.43.646.

[143] C. G. Choi, Y. T. Han, J. T. Kim, and H. Schift. Air-suspended two-dimensional polymer photonic crystal slab waveguides fabricated by nanoimprint lithography. *Applied Physics Letters*, 90(22):221109, 2007. doi:10.1063/1.2744482.

[144] X. Tao, C. Ruisheng, M. Bachman, and L. Guann-Pyng. Optical polymer waveguide based cantilevers for chemical and biological sensors. In *Sensors, 2005 IEEE*, pages 963–966, 2005. doi:10.1109/ICSENS.2005.1597861.

[145] L. J. Guerin, M. Bossel, M. Demierre, S. Calmes, and P. Renaud. Simple and low cost fabrication of embedded micro-channels by using a new thick-film photoplastic. *Transducers '97, lnternational Conference on Solid-State Sensors and Actuators (Chicago)*, 2:1419–1422, 1997. doi:10.1109/sensor.1997.635730.

[146] B. E. J. Alderman, C. M. Mann, D. P. Steenson, and J. M. Chamberlain. Microfabrication of channels using an embedded mask in negative resist. *Journal of Micromechanics and Microengineering*, 11(6):703–705, 2001. doi:10.1088/0960-1317/11/6/312.

[147] F. E. H. Tay, J. A. van Kan, F. Watt, and W. O. Choong. A novel micromachining method for the fabrication of thick-film SU-8 embedded micro-

channels. *Journal of Micromechanics and Microengineering*, 11(1):27–32, 2001. doi:10.1088/0960-1317/11/1/305.

[148] Y. J. Chuang, F. G. Tseng, J. H. Cheng, and W. K. Lin. A novel fabrication method of embedded micro-channels by using SU-8 thick-film photoresists. *Sensors and Actuators A: Physical*, 103(1-2):64–69, 2003. doi:10.1016/S0924-4247(02)00325-4.

[149] S. Metz, S. Jiguet, A. Bertsch, and P. Renaud. Polyimide and SU-8 microfluidic devices manufactured by heat-depolymerizable sacrificial material technique. *Lab Chip*, 4(2):114–20, 2004. doi:10.1039/b310866j.

[150] C. Fu, C. Hung, and H. Huang. A novel and simple fabrication method of embedded SU-8 micro channels by direct UV lithography. *Journal of Physics: Conference Series*, 34:330–335, 2006. doi:10.1088/1742-6596/34/1/054.

[151] B. E. A. Saleh and M. C. Teich. *Fundamentals of Photonics*, volume 2. Wiley & Sons Ltd, 2007. ISBN 9780471358329.

[152] R. B. Thompson. *Fluorescence Sensors and Biosensors*. CRC Press, 2005. ISBN 9780824727376.

[153] Daniel Colladon. On the reflections of a ray of light inside a parabolic liquid stream. *Comptes Rendus*, 15:800, 1842.

[154] R. G. Hunsperger. *Integrated optics: theory and technology*, volume 2. Springer, 1984. ISBN 9780387897752.

[155] M. Zourob, S. Elwary, and A. P. F. Turner. *Principles of Bacterial Detection: Biosensors, Recognition Receptors and Microsystems: Biosensors, Recognition Receptors, and Microsystems*. Springer Science & Business Media, 2008. ISBN 9780387751122.

[156] A. W. Snyder and J. Love. *Optical waveguide theory*. Springer Science & Business Media, 1983. ISBN 9780412242502.

[157] J. D. Joannopoulos, S.G. Johnson, J.N. Winn, and R.D. Meade. *Photonic crystals: molding the flow of light*. Princeton university press, 2008. ISBN 9780691124568.

[158] S. P. Pogossian, L. Vescan, and A. Vonsovici. The single-mode condition for semiconductor rib waveguides with large cross section. *Journal of Lightwave Technology*, 16(10):1851–1853, 1998. doi:10.1109/50.721072.

[159] R. A. Soref, J. Schmidtchen, and K. Petermann. Large Single-Mode Rib Waveguides in GeSi-Si and Si-on-SO2. *IEEE Journal of Quantum Electronics*, 27(8):1971–1974, 1991. doi:10.1109/3.83406.

[160] K. Petermann. Properties of Optical Rib-Guides with Large Cross-Section. *AEU-International Journal of Electronics and Communications*, 30(3):139–140, 1976.

[161] K. S. Chiang. Analysis of optical fibers by the effective-index method. *Applied Optics*, 25(3):348, 1986. doi:10.1364/ao.25.000348.

[162] K. S. Chiang. Effective-index method for the analysis of optical waveguide couplers and arrays: an asymptotic theory. *Journal of Lightwave Technology*, 9(1):62–72, 1991. doi:10.1109/50.64924.

[163] T. K. Lim and H. Melchior. Effective index method for generalised waveguide dispersion characteristics analysis of optical channel waveguides. *Electronics Letters*, 27(11):917–918, 1991. doi:10.1049/el:19910574.

[164] Q. Wang, G. Farrell, and T. Freir. Effective index method for planar lightwave circuits containing directional couplers. *Optics Communications*, 259 (1):133–136, 2006. doi:10.1016/j.optcom.2005.08.054.

[165] G. B. Hocker and W. K. Burns. Mode dispersion in diffused channel waveguides by the effective index method. *Appl Opt*, 16(1):113–8, 1977. doi:10.1364/AO.16.000113.

[166] CAMFR. (CAvity Modelling FRamework). *Available at:* `http://camfr.sourceforge.net/`. Viewed 20 Nov. 2016.

[167] C. L. Xu and W. P. Huang. Finite-difference beam propagation method for guide-wave optics. *Progress In Electromagnetics Research*, 11:1–49, 1995.

[168] C. Prokop, S. Schoenhardt, B. Laegel, S. Wolff, A. Mitchell, and C. Karnutsch. Air-suspended polymer waveguide grating couplers

of SU-8. *Journal of Lightwave Technology*, 34(17):3966–3971, 2016. doi:10.1109/JLT.2016.2593025.

[169] L. Eldada and L. W. Shacklette. Advances in polymer integrated optics. *IEEE Journal of Selected Topics in Quantum Electronics*, 6(1):54–68, 2000. doi:10.1109/2944.826873.

[170] M. Heckele, W. Bacher, and K. D. Muller. Hot embossing - The molding technique for plastic microstructures. *Microsystem Technologies*, 4(3):122–124, 1998. doi:10.1007/s005420050112.

[171] C. M. S. Torres, S. Zankovych, J. Seekamp, A. P. Kam, C. C. Cedeno, T. Hoffmann, J. Ahopelto, F. Reuther, K. Pfeiffer, G. Bleidiessel, G. Gruetzner, M. V. Maximov, and B. Heidari. Nanoimprint lithography: an alternative nanofabrication approach. *Materials Science & Engineering C-Biomimetic and Supramolecular Systems*, 23(1-2):23–31, 2003. doi:10.1016/S0928-4931(02)00221-7.

[172] P. Kozma, F. Kehl, E. Ehrentreich-Forster, C. Stamm, and F. F. Bier. Integrated planar optical waveguide interferometer biosensors: a comparative review. *Biosens Bioelectron*, 58:287–307, 2014. doi:10.1016/j.bios.2014.02.049.

[173] S. Somekh, E. Garmire, A. Yariv, H. L. Garvin, and R. G. Hunsperger. Channel optical waveguide directional couplers. *Applied Physics Letters*, 22 (1):46, 1973. doi:10.1063/1.1654468.

[174] L. Vivien, D. Pascal, S. Lardenois, D. Marris-Morini, E. Cassan, F. Grillot, S. Laval, J. M. Fedeli, and M. Loubna El. Light injection in SOI microwaveguides using high-efficiency grating couplers. *Journal of Lightwave Technology*, 24(10):3810–3815, 2006. doi:10.1109/jlt.2006.878060.

[175] Taillaert. D. Grating coupler as Interface between optical fibres and nanophotonic waveguides. *Ghent University, Department of Information Technology (INTEC)*, 2004. Ph.D. thesis.

[176] D. Taillaert, P. Bienstman, and R. Baets. Compact efficient broadband grating coupler for silicon-on-insulator waveguides. *Opt Lett*, 29(23):2749–51, 2004. doi:10.1364/OL.29.002749.

[177] F. Van Laere, G. Roelkens, M. Ayre, J. Schrauwen, D. Taillaert, D. Van Thourhout, T. F. Krauss, and R. Baets. Compact and Highly Efficient Grating Couplers Between Optical Fiber and Nanophotonic Waveguides. *Journal of Lightwave Technology*, 25(1):151–156, 2007. doi:10.1109/jlt.2006.888164.

[178] D. Taillaert, F. Van Laere, M. Ayre, W. Bogaerts, D. Van Thourhout, P. Bienstman, and R. Baets. Grating couplers for coupling between optical fibers and nanophotonic waveguides. *Japanese Journal of Applied Physics Part 1-Regular Papers Brief Communications & Review Papers*, 45(8A):6071–6077, 2006. doi:10.1143/Jjap.45.6071.

[179] F. Golek, P. Mazur, Z. Ryszka, and S. Zuber. AFM image artifacts. *Applied Surface Science*, 304:11–19, 2014. doi:10.1016/j.apsusc.2014.01.149.

[180] D. J. Keller and F. S. Franke. Envelope reconstruction of probe microscope images. *Surface Science*, 294(3):409–419, 1993. doi:10.1016/0039-6028(93)90126-5.

[181] U. D. Schwarz, H. Haefke, P. Reimann, and H. J. Güntherodt. Tip artefacts in scanning force microscopy. *Journal of Microscopy*, 173(3):183–197, 1994. doi:10.1111/j.1365-2818.1994.tb03441.x.

[182] Python. *Available at:* `https://www.python.org/`. Viewed 20 Nov. 2016.

[183] IPKISS. *Available at:* `http://www.ipkiss.org/`. Viewed 20 Nov. 2016.

[184] A. Borreman, S. Musa, A. Kok, M. Diemeer, and A. Driessen. Fabrication of Polymeric Multimode Waveguides and Devices in SU-8 Photoresist Using Selective Polymerization. In *Proceedings of the Symposium on IEEE/LEOS Benelux Chapter, Amsterdam*, pages P83–P86, 2002. ISBN 908075191X.

[185] D. Yin, H. Schmidt, J. Barber, and A. Hawkins. Integrated ARROW waveguides with hollow cores. *Opt Express*, 12(12):2710–5, 2004. doi:10.1364/OPEX.12.002710.

[186] F. Van Laere, T. Claes, J. Schrauwen, S. Scheerlinck, W. Bogaerts, D. Taillaert, L. O'Faolain, D. Van Thourhout, and R. Baets. Compact focusing grating couplers for silicon-on-insulator integrated cir-

cuits. *IEEE Photonics Technology Letters*, 19(21-24):1919–1921, 2007. doi:10.1109/Lpt.2007.908762.

[187] C. Prokop, T. Schmalz, P. Kleeßen, Laegel. B., S. Wolff, A. Mitchell, and C. Karnutsch. Tunable air-suspended polymer grating couplers. *Optical Engineering*, 56(6):067112–4, 2017. doi:10.1117/1.OE.56.6.067112.

[188] Z. Zhang, G. Genrich, N. Keil, and N. Grote. Widely tunable grating-assisted heterogeneous silicon nitride/polymer waveguide coupler. *Opt Lett*, 39(1): 162–5, 2014. doi:10.1364/OL.39.000162.

[189] J. Komma, C. Schwarz, G. Hofmann, D. Heinert, and R. Nawrodt. Thermo-optic coefficient of silicon at 1550 nm and cryogenic temperatures. *Applied Physics Letters*, 101(4):041905, 2012. doi:10.1063/1.4738989.

[190] Z. Xiao, F. Luan, T. Y. Liow, J. Zhang, and P. Shum. Design for broadband high-efficiency grating couplers. *Opt Lett*, 37(4):530–2, 2012. doi:10.1364/OL.37.000530.

[191] A. Othonos. Fiber Bragg gratings. *Review of Scientific Instruments*, 68(12): 4309–4341, 1997. doi:10.1063/1.1148392.

[192] H. Lorenz, M. Laudon, and P. Renaud. Mechanical characterization of a new high-aspect-ratio near UV-photoresist. *Microelectronic Engineering*, 41-42: 371–374, 1998. doi:10.1016/s0167-9317(98)00086-0.

[193] K. K. Tung, W. H. Wong, and E. Y. B. Pun. Polymeric optical waveguides using direct ultraviolet photolithography process. *Applied Physics a-Materials Science & Processing*, 80(3):621–626, 2005. doi:10.1007/s00339-003-2248-8.

[194] H. Y. Liu, G. D. Peng, and P. L. Chu. Thermal tuning of polymer optical fiber Bragg gratings. *IEEE Photonics Technology Letters*, 13(8):824–826, 2001. doi:10.1109/68.935816.

[195] H. Zou, K. W. Beeson, and P. M. Ferm. Polymer Bragg gratings for telecom applications. *Proc. SPIE*, 4805:68–78, 2002. doi:10.1117/12.450895.

[196] C. Prokop, I. Irmler, B. Laegel, S. Wolff, A. Mitchell, and C. Karnutsch. Optofluidic refractive index sensor based on air-suspended SU-8

grating couplers. *Sensors and Actuators A: Physical*, 263:439–444, 2017. doi:10.1016/j.sna.2017.07.014.

[197] D. Psaltis, S. R. Quake, and C. Yang. Developing optofluidic technology through the fusion of microfluidics and optics. *Nature*, 442(7101):381–6, 2006. doi:10.1038/nature05060.

[198] G. Testa, G. Persichetti, and R. Bernini. Optofluidic approaches for enhanced microsensor performances. *Sensors (Basel)*, 15(1):465–84, 2015. doi:10.3390/s150100465.

[199] P. Abgrall and A. M. Gue. Lab-on-chip technologies: making a microfluidic network and coupling it into a complete microsystem - a review. *Journal of Micromechanics and Microengineering*, 17(5):R15–R49, 2007. doi:10.1088/0960-1317/17/5/R01.

[200] S. J. Lee and S. Y. Lee. Micro total analysis system (micro-TAS) in biotechnology. *Appl Microbiol Biotechnol*, 64(3):289–99, 2004. doi:10.1007/s00253-003-1515-0.

[201] J. Homola, S. S. Yee, and G. Gauglitz. Surface plasmon resonance sensors: review. *Sensors and Actuators B: Chemical*, 54(1-2):3–15, 1999. doi:10.1016/s0925-4005(98)00321-9.

[202] E. Chow, A. Grot, L. W. Mirkarimi, M. Sigalas, and G. Girolami. Ultracompact biochemical sensor built with two-dimensional photonic crystal microcavity. *Opt Lett*, 29(10):1093–5, 2004. doi:10.1364/OL.29.001093.

[203] M. R. Lee and P. M. Fauchet. Two-dimensional silicon photonic crystal based biosensing platform for protein detection. *Opt Express*, 15(8):4530–5, 2007. doi:10.1364/OE.15.004530.

[204] L. Rindorf, J. B. Jensen, M. Dufva, L. H. Pedersen, P. E. Hoiby, and O. Bang. Photonic crystal fiber long-period gratings for biochemical sensing. *Opt Express*, 14(18):8224–31, 2006. doi:10.1364/OE.14.008224.

[205] S. Arnold, M. Khoshsima, I. Teraoka, S. Holler, and F. Vollmer. Shift of whispering-gallery modes in microspheres by protein adsorption. *Optics Letters*, 28(4):272, 2003. doi:10.1364/ol.28.000272.

[206] N. M. Hanumegowda, C. J. Stica, B. C. Patel, I. White, and X. D. Fan. Refractometric sensors based on microsphere resonators. *Applied Physics Letters*, 87(20), 2005. doi:10.1063/1.2132076.

[207] A. Ksendzov and Y. Lin. Integrated optics ring-resonator sensors for protein detection. *Opt Lett*, 30(24):3344–6, 2005. doi:10.1364/OL.30.003344.

[208] C. Y. Chao, W. Fung, and L. J. Guo. Polymer microring resonators for biochemical sensing applications. *IEEE Journal of Selected Topics in Quantum Electronics*, 12(1):134–142, 2006. doi:10.1109/Jstqe.2005.862945.

[209] A. Yalcin, K. C. Popat, J. C. Aldridge, T. A. Desai, J. Hryniewicz, N. Chbouki, B. E. Little, King Oliver, V. Van, Chu Sai, D. Gill, M. Anthes-Washburn, M. S. Unlu, and B. B. Goldberg. Optical sensing of biomolecules using microring resonators. *IEEE Journal of Selected Topics in Quantum Electronics*, 12(1):148–155, 2006. doi:10.1109/jstqe.2005.863003.

[210] H. Zhu, I. M. White, J. D. Suter, P. S. Dale, and X. Fan. Analysis of biomolecule detection with optofluidic ring resonator sensors. *Optics Express*, 15(15):9139, 2007. doi:10.1364/oe.15.009139.

[211] S. Song, H. Xu, and C. Fan. Potential diagnostic applications of biosensors: current and future directions. *International Journal of Nanomedicine*, 1(4): 433–440, 2006. doi:10.2147/nano.2006.1.4.433.

[212] X. Fan, I. M. White, S. I. Shopova, H. Zhu, J. D. Suter, and Y. Sun. Sensitive optical biosensors for unlabeled targets: A review. *Anal Chim Acta*, 620(1): 8–26, 2008. doi:10.1016/j.aca.2008.05.022.

[213] B. Hooda and V. Rastogi. Low cost highly sensitive miniaturized refractive index sensor based on planar waveguide. *Optik-International Journal for Light and Electron Optics*, 143:158–166, 2017. doi:10.1016/j.ijleo.2017.06.050.

[214] E. Mauriz, A. Calle, J. J. Manclus, A. Montoya, A. Hildebrandt, D. Barcelo, and L. M. Lechuga. Optical immunosensor for fast and sensitive detection of DDT and related compounds in river water samples. *Biosens Bioelectron*, 22(7):1410–1418, 2007. doi:10.1016/j.bios.2006.06.016.

[215] J. Trevino, A. Calle, J. M. Rodriguez-Frade, M. Mellado, and L. M. Lechuga. Surface plasmon resonance immunoassay analysis of pituitary hormones in urine and serum samples. *Clin Chim Acta*, 403(1):56–62, 2009. doi:10.1016/j.cca.2009.01.015.

[216] L. G. Carrascosa, A. Calle, and L. M. Lechuga. Label-free detection of DNA mutations by SPR: application to the early detection of inherited breast cancer. *Anal Bioanal Chem*, 393(4):1173, 2009. doi:10.1007/s00216-008-2555-1.

[217] M. C. Estevez, M. Alvarez, and L. M. Lechuga. Integrated optical devices for lab-on-a-chip biosensing applications. *Laser & Photonics Reviews*, 6(4): 463–487, 2012. doi:10.1002/lpor.201100025.

[218] X. Fan and I. M. White. Optofluidic Microsystems for Chemical and Biological Analysis. *Nat Photonics*, 5(10):591–597, 2011. doi:10.1038/nphoton.2011.206.

[219] P. M. Nellen, K. Tiefenthaler, and W. Lukosz. Integrated Optical Input Grating Couplers as Biochemical Sensors. *Sensors and Actuators*, 15(3): 285–295, 1988. doi:10.1016/0250-6874(88)87017-3.

[220] P. V. Lambeck. Integrated optical sensors for the chemical domain. *Measurement Science and Technology*, 17(8):R93–R116, 2006. doi:10.1088/0957-0233/17/8/R01.

[221] M. C. Estevez, M. Alvarez, and L. M. Lechuga. Integrated optical devices for lab-on-a-chip biosensing applications. *Laser & Photonics Reviews*, 6(4): 463–487, 2012. doi:10.1002/lpor.201100025.

[222] L. Eldada and L. W. Shacklette. Advances in polymer integrated optics. *IEEE Journal of Selected Topics in Quantum Electronics*, 6(1):54–68, 2000. doi:10.1109/2944.826873.

[223] H. Ma, A. K. Y. Jen, and L. R. Dalton. Polymer-based optical waveguides: Materials, processing, and devices. *Advanced Materials*, 14 (19):1339–1365, 2002. doi:10.1002/1521-4095(20021002)14:19<1339::Aid-Adma1339>3.0.Co;2-O.

[224] D. Irimia. *Capillary Force Valves*, pages 192–196. Springer, 2008. ISBN 0387324682.

[225] C. A. Barrios, K. B. Gylfason, B. Sanchez, A. Griol, H. Sohlstrom, M. Holgado, and R. Casquel. Slot-waveguide biochemical sensor. *Optics letters*, 32 (21):3080–3082, 2007. doi:10.1364/OL.32.003080.

[226] S. Grego, K. H. Gilchrist, J. B. Carlson, and B. R. Stoner. A compact and multichannel optical biosensor based on a wavelength interrogated input grating coupler. *Sensors and Actuators B: Chemical*, 161(1):721–727, 2012. doi:10.1016/j.snb.2011.11.020.

[227] T. Allsop, R. Neal, S. Rehman, D. J. Webb, D. Mapps, and I. Bennion. Generation of infrared surface plasmon resonances with high refractive index sensitivity utilizing tilted fiber Bragg gratings. *Appl Opt*, 46(22):5456–60, 2007. doi:10.1364/AO.46.005456.

[228] P. Pfeifer, U. Aldinger, G. Schwotzer, S. Diekmann, and P. Steinrucke. Real time sensing of specific molecular binding using surface plasmon resonance spectroscopy. *Sensors and Actuators B: Chemical*, 54(1-2):166–175, 1999. doi:10.1016/S0925-4005(98)00334-7.

[229] S. Blair and Y. Chen. Resonant-enhanced evanescent-wave fluorescence biosensing with cylindrical optical cavities. *Appl Opt*, 40(4):570–82, 2001. doi:10.1364/Ao.40.000570.

[230] A. Leung, P. M. Shankar, and R. Mutharasan. A review of fiber-optic biosensors. *Sensors and Actuators B: Chemical*, 125(2):688–703, 2007. doi:10.1016/j.snb.2007.03.010.

[231] M. Liscidini and J. E. Sipe. Enhancement of diffraction for biosensing applications via Bloch surface waves. *Applied Physics Letters*, 91(25), 2007. doi:10.1063/1.2826545.

[232] T. F. Krauss. Why do we need slow light? *Nature Photonics*, 2(8):448–450, 2008. doi:10.1038/nphoton.2008.139.

[233] D. Yin, D. W. Deamer, H. Schmidt, J. P. Barber, and A. R. Hawkins. Integrated optical waveguides with liquid cores. *Applied Physics Letters*, 85 (16):3477–3479, 2004. doi:10.1063/1.1807966.

[234] V. Bhatia, D. Campbell, R. O. Claus, and A. M. Vengsarkar. Simultaneous strain and temperature measurement with long-period gratings. *Optics Letters*, 22(9):648, 1997. doi:10.1364/ol.22.000648.

[235] M. N. Ng, Z. Chen, and K. S. Chiang. Temperature compensation of long-period fiber grating for refractive-index sensing with bending effect. *IEEE Photonics Technology Letters*, 14(3):361–362, 2002. doi:10.1109/68.986813.

[236] C. Guan, X. Tian, S. W. Li, X. L. Zhong, J. Shi, and L. Yuan. Long period fiber grating and high sensitivity refractive index sensor based on hollow eccentric optical fiber. *Sensors and Actuators B: Chemical*, 188:768–771, 2013. doi:10.1016/j.snb.2013.07.086.

[237] P. F. Wysocki, J. B. Judkins, R. P. Espindola, M. Andrejco, and A. M. Vengsarkar. Broad-band erbium-doped fiber amplifier flattened beyond 40 nm using long-period grating filter. *IEEE Photonics Technology Letters*, 9 (10):1343–1345, 1997. doi:10.1109/68.623257.

[238] A. M. Vengsarkar, P. J. Lemaire, J. B. Judkins, V. Bhatia, T. Erdogan, and J. E. Sipe. Long-period fiber gratings as band-rejection filters. *Journal of Lightwave Technology*, 14(1):58–65, 1996. doi:10.1109/50.476137.

[239] D. B. Stegall and T. Erdogan. Dispersion control with use of long-period fiber gratings. *Journal of the Optical Society of America A*, 17(2):304, 2000. doi:10.1364/josaa.17.000304.

[240] K. S. Chiang, Y. Liu, M. N. Ng, and S. Li. Coupling between two parallel long-period fibre gratings. *Electronics Letters*, 36(16):1408, 2000. doi:10.1049/el:20001014.

[241] Q. Liu, K. S. Chiang, and V. Rastogi. Analysis of corrugated long-period gratings in slab waveguides and their polarization dependence. *Journal of Lightwave Technology*, 21(12):3399–3405, 2003. doi:10.1109/jlt.2003.821749.

[242] K. S. Chiang, K. P. Lor, C. K. Chow, H. P. Chan, V. Rastogi, and Y. M. Chu. Widely tunable long-period gratings fabricated in polymer-clad ion-exchanged glass waveguides. *IEEE Photonics Technology Letters*, 15(8): 1094–1096, 2003. doi:10.1109/lpt.2003.815331.

[243] Q. Liu, K. Chiang, and K. Lor. Long-period gratings in polymer ridge waveguides. *Opt Express*, 13(4):1150–60, 2005. doi:10.1364/opex.13.001150.

[244] V. Rastogi and K. Seng Chiang. Long-period gratings in planar optical waveguides. *Applied Optics*, 41(30):6351, 2002. doi:10.1364/ao.41.006351.

[245] K. S. Chiang, K. P. Lor, Q. Liu, C. K. Chow, Y. M. Chu, and H. P. Chan. Long-Period Waveguide Gratings. *Japanese Journal of Applied Physics*, 43 (8B):5690–5696, 2004. doi:10.1143/jjap.43.5690.

[246] K. P. Lor, Q. Liu, and K. S. Chiang. UV-written long-period gratings on polymer waveguides. *IEEE Photonics Technology Letters*, 17(3):594–596, 2005. doi:10.1109/lpt.2004.840918.

[247] S. Pal and B. R. Singh. Analysis and Design of Corrugated Long-Period Gratings in Silica-on-Silicon Planar Waveguides. *Journal of Lightwave Technology*, 25(8):2260–2267, 2007. doi:10.1109/jlt.2007.901335.

[248] A. Yariv. *Optical Electronics in Modern Communications*. Number Bd. 1 in Oxford series in electrical and computer engineering. Oxford University Press, 1997. ISBN 9780195106268.

[249] T. W. MacDougall, S. Pilevar, C. W. Haggans, and M. A. Jackson. Generalized expression for the growth of long period gratings. *IEEE Photonics Technology Letters*, 10(10):1449–1451, 1998. doi:10.1109/68.720290.

[250] S. Xuewen, Z. Lin, and I. Bennion. Sensitivity characteristics of long-period fiber gratings. *Journal of Lightwave Technology*, 20(2):255–266, 2002. doi:10.1109/50.983240.

[251] R. Bernini, S. Campopiano, L. Zeni, and P. M. Sarro. ARROW optical waveguides based sensors. *Sensors and Actuators B: Chemical*, 100(1-2): 143–146, 2004. doi:10.1016/j.snb.2003.12.035.

[252] R. F. Cregan, B. J. Mangan, J. C. Knight, T. A. Birks, P. S. Russell, P. J. Roberts, and D. C. Allan. Single-Mode Photonic Band Gap Guidance of Light in Air. *Science*, 285(5433):1537–1539, 1999. doi:10.1126/science.285.5433.1537.

[253] Y. Fink, D. J. Ripin, S. H. Fan, C. P. Chen, J. D. Joannopoulos, and E. L. Thomas. Guiding optical light in air using an all-dielectric structure. *Journal of Lightwave Technology*, 17(11):2039–2041, 1999. doi:10.1109/50.802992.

[254] Y. Yi, S. Akiyama, P. Bermel, X. Duan, and L. Kimerling. On-chip Si-based Bragg cladding waveguide with high index contrast bilayers. *Opt Express*, 12(20):4775–80, 2004. doi:10.1364/Opex.12.004775.

[255] J. Sun and C. C. Chan. Photonic bandgap fiber for refractive index measurement. *Sensors and Actuators B: Chemical*, 128(1):46–50, 2007. doi:10.1016/j.snb.2007.05.037.

[256] H. Qu and M. Skorobogatiy. Liquid-core low-refractive-index-contrast Bragg fiber sensor. *Applied Physics Letters*, 98(20), 2011. doi:10.1063/1.3592758.

[257] K. J. Rowland, V. Shahraam Afshar, A. Stolyarov, Y. Fink, and T. M. Monro. Bragg waveguides with low-index liquid cores. *Opt Express*, 20(1): 48–62, 2012. doi:10.1364/OE.20.000048.

[258] E. Zeller. *Planar fluid-tunable waveguide arrays*. Ph.D. Thesis, RMIT University, 2014.

[259] R. Horvath, L. R. Lindvold, and N. B. Larsen. Reverse-symmetry waveguides: theory and fabrication. *Applied Physics B-Lasers and Optics*, 74 (4-5):383–393, 2002. doi:10.1007/s003400200823.

[260] A. V. Kabashin, P. Evans, S. Pastkovsky, W. Hendren, G. A. Wurtz, R. Atkinson, R. Pollard, V. A. Podolskiy, and A. V. Zayats. Plasmonic nanorod metamaterials for biosensing. *Nat Mater*, 8(11):867–871, 2009. doi:10.1038/nmat2546.

[261] G. G. Nenninger, M. Piliarik, and J. Homola. Data analysis for optical sensors based on spectroscopy of surface plasmons. *Measurement Science and Technology*, 13(12):2038, 2002. doi:10.1088/0957-0233/13/12/332.

[262] T. Allsop, R. Neal, S. Rehman, D. J. Webb, D. Mapps, and I. Bennion. Generation of infrared surface plasmon resonances with high refractive index sensitivity utilizing tilted fiber Bragg gratings. *Applied optics*, 46(22):5456–5460, 2007. doi:10.1364/AO.46.005456.

[263] A. Hassani, B. Gauvreau, M. F. Fehri, A. Kabashin, and M. Skorobogatiy. Photonic crystal fiber and waveguide-based surface plasmon resonance sensors for application in the visible and near-IR. *Electromagnetics*, 28(3): 198–213, 2008. doi:10.1080/02726340801921627.

[264] R. Garg, S. M. Tripathi, K. Thyagarajan, and W. J. Bock. Long period fiber grating based temperature-compensated high performance sensor for bio-chemical sensing applications. *Sensors and Actuators B: Chemical*, 176: 1121–1127, 2013. doi:10.1016/j.snb.2012.08.059.

[265] M. Sumetsky, R. S. Windeler, Y. Dulashko, and X. Fan. Optical liquid ring resonator sensor. *Optics Express*, 15(22):14376–14381, 2007. doi:10.1364/OE.15.014376.

[266] A. E. Cetin and H. Altug. Fano resonant ring/disk plasmonic nanocavities on conducting substrates for advanced biosensing. *ACS nano*, 6(11):9989–9995, 2012. doi:10.1021/nn303643w.

[267] G. K. Joshi, P. J. McClory, S. Dolai, and R. Sardar. Improved localized surface plasmon resonance biosensing sensitivity based on chemically-synthesized gold nanoprisms as plasmonic transducers. *J. Mater. Chem.*, 22 (3):923–931, 2012. doi:10.1039/C1JM14391C.

[268] M. M. Miller and A. A. Lazarides. Sensitivity of metal nanoparticle surface plasmon resonance to the dielectric environment. *J Phys Chem B*, 109(46): 21556–21565, 2005. doi:10.1021/jp054227y.

[269] N. M. Hanumegowda, C. J. Stica, B. C. Patel, I. White, and X. Fan. Refractometric sensors based on microsphere resonators. *Applied Physics Letters*, 87(20):201107, 2005. doi:10.1063/1.2132076.

[270] J. L. Arlett, E. B. Myers, and M. L. Roukes. Comparative advantages of mechanical biosensors. *Nat Nanotechnol*, 6(4):203–215, 2011. doi:10.1038/nnano.2011.44.

[271] B. Liedberg, C. Nylander, and I. Lunstrom. Surface plasmon resonance for gas detection and biosensing. *Sensors and Actuators*, 4:299–304, 1983. doi:10.1016/0250-6874(83)85036-7.

Appendix A

Supporting simulations of air-suspended SU-8 grating couplers

In order to better understand the sensitivity of the air-suspended SU-8 grating couplers to variations in the grating parameters, additional simulations to the simulations demonstrated in Section 5.3 have been carried out. Errors on the waveguide thickness, filling factor, groove depth, grating period and coupling angle have been introduced to the grating structure. For the following simulations, all parameters were kept constant while the investigated parameter (see insets in the figures) was varied.

Fig. 8.1 shows the result, when the waveguide thickness t is varied within the single-mode condition. With increasing waveguide thickness, the effective index changes and thus the phase matching condition which can result in a shift of the spectral response towards longer wavelengths while the coupling loss stays constant. The resonant wavelength shift is approximately 7 pm per nm change in thickness of the waveguide.

Fig. 8.2 shows the result, when the filling factor is varied. Variations of the optimum ratio of 0.5 cause a shift of the spectral response towards shorter wavelengths for values lower than 0.5, while higher values result in a shift towards longer wavelengths. The coupling loss increases the higher the difference to the ideal value between 0.4 and 0.5 gets.

Fig. 8.3 shows the result, when the groove depth e is varied. Variations cause a shift of the grating coupler spectrum and a change in the coupling loss. The shallower a grating is the weaker it is in terms of coupled light efficiency. Deeper gratings result in a shift towards shorter wavelengths.

Fig. 8.4 shows the result, when the grating period Λ is varied. With increasing period, the spectral response of the grating coupler shifts towards longer wavelengths while the coupling loss stays almost constant at around 5 dB.

Fig. 8.5 shows the result, when the coupling angle θ is varied. Adjusting the angle of the incident light over a range of about 4° to 18°, can cause a shift in the resonant wavelength towards shorter wavelengths of about 15 nm/°.

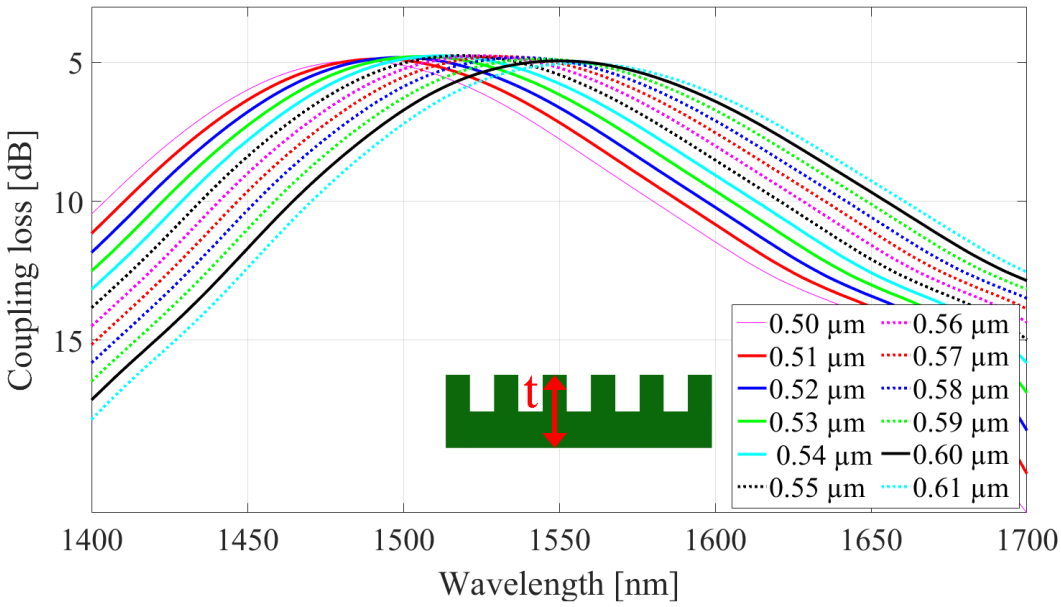

Figure 8.1: Variation of the waveguide thickness. All other simulation parameters were kept constant. With increasing waveguide thickness, the effective index changes and thus the phase matching condition resulting in a shift of the spectral response towards longer wavelengths.

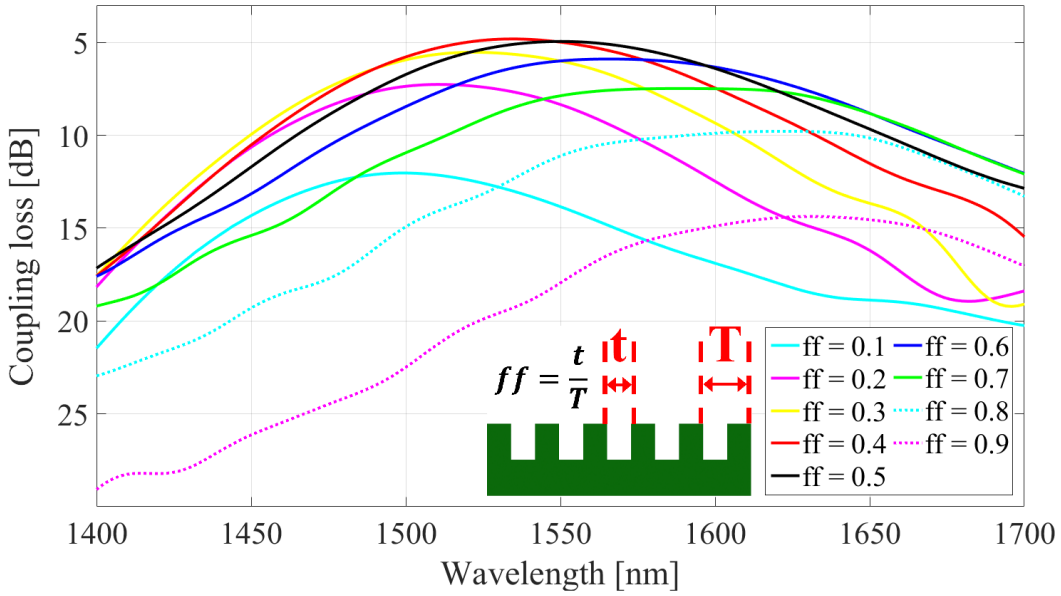

Figure 8.2: Variation of the filling factor. All other simulation parameters were kept constant. Variations of the optimum ratio of 0.5 cause a shift of the spectral response towards shorter wavelengths for values lower than 0.5, while higher values result in a shift towards longer wavelengths.

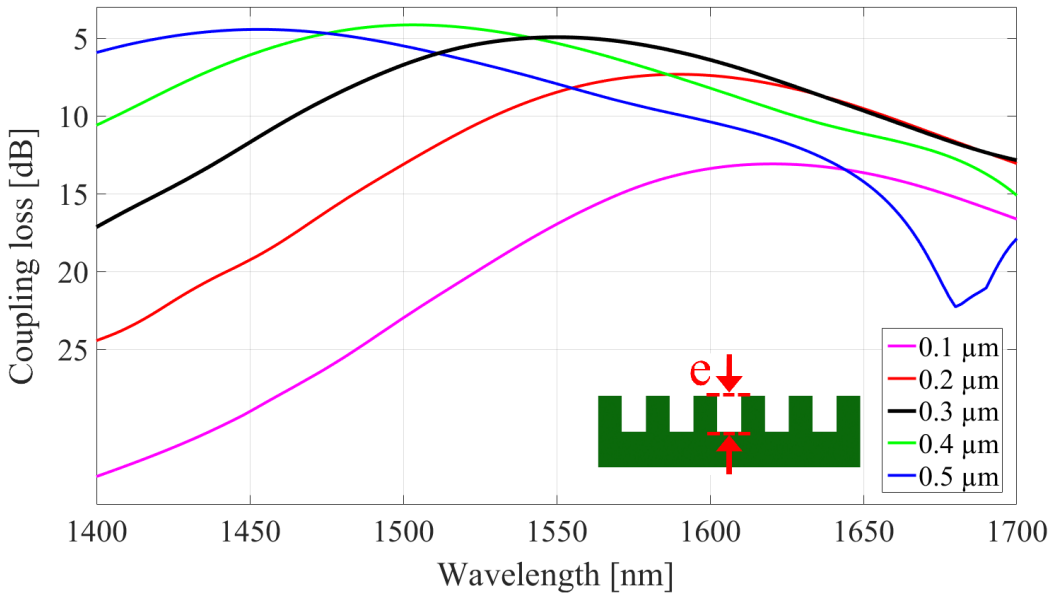

Figure 8.3: Variation of the groove depth. All other simulation parameters were constant. Variations cause a shift of the grating coupler spectrum and coupling loss difference. The shallower a grating is the weaker it is in terms of coupled light efficiency. Deeper gratings result in a shift towards shorter wavelengths.

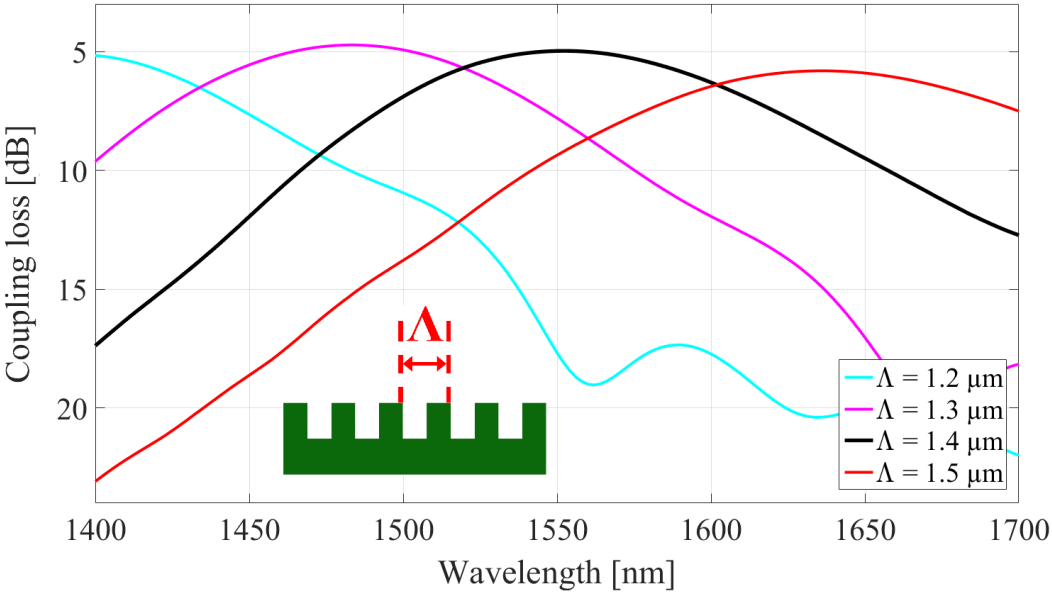

Figure 8.4: Variation of the grating period. All other simulation parameters were constant. With increasing period, the spectral response of the grating coupler shifts towards longer wavelengths while the coupling loss stays almost constant at around 5 dB.

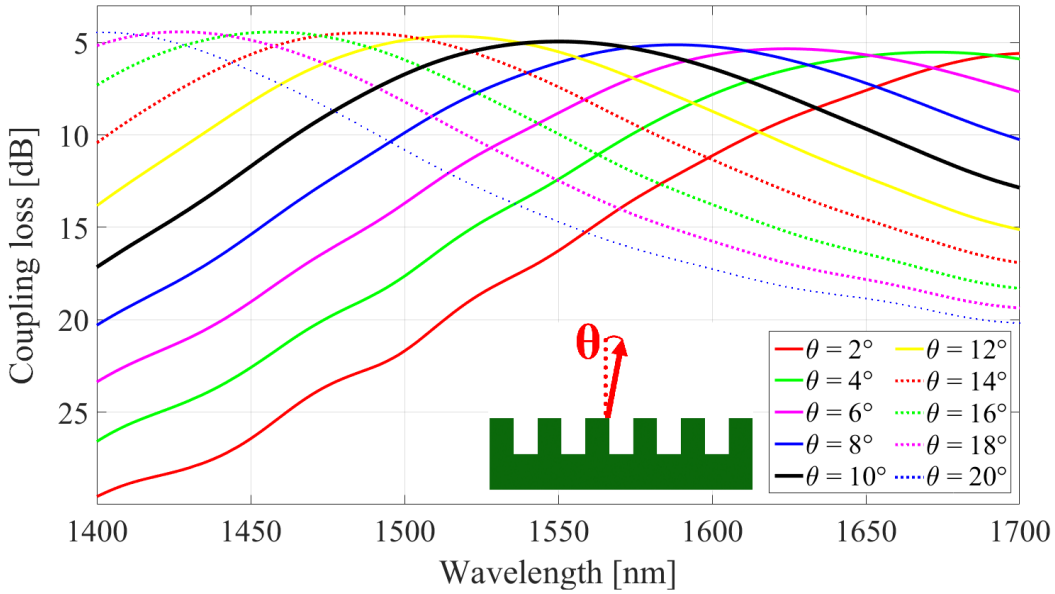

Figure 8.5: Variation of the coupling angle. All other simulation parameters were constant. Adjusting the angle of the incident light over a range of about 4° to 18°, can cause a shift in the resonant wavelength towards shorter wavelengths of about 15 nm/° towards shorter wavelengths.